

Understanding solid-state batteries

The route to stability

Schwietert, T.K.

DOI

[10.4233/uuid:4bb38399-9267-428f-b10a-80b86e101f23](https://doi.org/10.4233/uuid:4bb38399-9267-428f-b10a-80b86e101f23)

Publication date

2022

Document Version

Final published version

Citation (APA)

Schwietert, T. K. (2022). *Understanding solid-state batteries: The route to stability*.
<https://doi.org/10.4233/uuid:4bb38399-9267-428f-b10a-80b86e101f23>

Important note

To cite this publication, please use the final published version (if applicable).
Please check the document version above.

Copyright

Other than for strictly personal use, it is not permitted to download, forward or distribute the text or part of it, without the consent of the author(s) and/or copyright holder(s), unless the work is under an open content license such as Creative Commons.

Takedown policy

Please contact us and provide details if you believe this document breaches copyrights.
We will remove access to the work immediately and investigate your claim.

UNDERSTANDING SOLID-STATE BATTERIES

THE ROUTE TO STABILITY

Proefschrift

ter verkrijging van de graad van doctor
aan de Technische Universiteit Delft,
op gezag van de Rector Magnificus prof. dr. ir. T.H.J.J. Van der Hagen,
voorzitter van het College voor Promoties,
in het openbaar te verdedigen op maandag 10 oktober 2022 om 15:00 uur

door

Tammo Klaas SCHWIETERT

Master of Science in Applied Physics,
Technische Universiteit Delft, Delft, Nederland,
geboren te Amsterdam.

Dit proefschrift is goedgekeurd door de promotoren.

Samenstelling promotiecommissie:

Rector Magnificus,	Voorzitter
Prof. dr. ir. M. Wagemaker,	Technische Universiteit Delft, promotor
Dr. E.M. Kelder,	Technische Universiteit Delft, promotor

Onafhankelijke leden:

Prof. dr. M.Z. Bazant	Massachusetts Institute of Technology, VS
Prof. dr. J. Janek,	Justus Liebig University Giessen, Duitsland
Prof. dr. ir. F.M. Mulder,	Technische Universiteit Delft
Dr. J.A. Dawson,	Newcastle University, Verenigd Koninkrijk
Prof. dr. E.H. Brück,	Technische Universiteit Delft, reservelid

Overig lid:

Dr. ir. A. Vasileiadis,	Technische Universiteit Delft
-------------------------	-------------------------------



Keywords: Solid-state batteries, Solid electrolytes, Electrochemical stability, Solid electrolyte redox, Decomposition window, Intrinsic window

Cover design: Hugo Romer & Tammo Schwieter

Printed by: ProefschriftMaken

Copyright © 2022 by T.K. Schwieter

ISBN 978-94-6423-992-8

An electronic version of this dissertation is available at
<http://repository.tudelft.nl/>.

To Harry Schwietert

CONTENTS

1	Introduction	1
1.1	The relevance of batteries in our future society	2
1.2	Li-ion batteries towards solid-state batteries	2
1.3	Challenges in solid-state batteries	4
1.4	Modeling of solid-state batteries	5
1.5	The electrochemical Stability window.	6
1.6	The ionic conductivity	7
1.7	Microscopic model for solid-state batteries	8
1.8	Thesis Outline	9
	References	11
2	Clarifying the relationship between redox activity and electrochemical stability in solid electrolytes	13
2.1	Abstract	14
2.2	Introduction	14
2.3	Results	15
2.4	Conclusion	27
2.5	Materials and Methods	27
	References	30
3	First-principles prediction of the electrochemical stability and reaction mechanisms of solid-state electrolytes	35
3.1	Abstract	36
3.2	Introduction	36
3.3	Methods	38
3.4	Results	38
3.5	Discussion	45
3.6	Conclusion	47
	References	49
4	The effect of aliovalent cation substitution on the Li-ion diffusion mechanism in Li-argyrodites.	53
4.1	Abstract	54
4.2	Introduction	54
4.3	Method	55
4.4	Results	56
4.5	Conclusion	62
	References	63

5	An advanced model for solid-state batteries and its main challenges	67
5.1	Abstract	68
5.2	Introduction	68
5.3	Methods	70
5.4	Results	75
5.5	Conclusion	82
5.6	Parameters	84
	References	85
A	Appendix	91
A.1	Appendix Chapter 2	91
A.2	Appendix Chapter 3	96
A.3	Appendix Chapter 4	103
	References	105
	Summary	107
	Samenvatting	109
	Acknowledgements	111
	Conferences	113
	List of Publications	115
	Curriculum Vitae	117

1

INTRODUCTION

1.1. THE RELEVANCE OF BATTERIES IN OUR FUTURE SOCIETY

WE are all aware of the importance of batteries in our daily lives. Our laptops, mobile phones, headphones and practically every other portable electronic device is battery powered as they make devices wireless and therefore much more convenient to use. However, maybe not everybody is aware that batteries also play a crucial role against climate change in the future energy systems of our society.

The importance of energy storage in electrical grids originates from the intermittent energy output of renewable energy sources such as wind and solar. When the wind is not blowing or there is limited sunlight, we need to use energy that is stored in times of excess energy generation and use it in times of shortage. At this moment, hydroelectricity is globally the most installed storage mechanism, however, batteries are growing fast as a storage technology, and are expected to be in equal use as hydro-storage around 2030.¹ This increase in battery storage systems is caused by the growing demand and wider deployment of battery applications, which lowered the price of batteries dramatically over the last decade.² Also recent developments in battery technologies such as flow batteries and high-temperature sodium sulfur gain increasing interest for stationary storage applications as they are generally easier to scale compared to Li-ion batteries.

In the transport sector, a sharp increase in the sales of battery-driven vehicles occurred in the past decade, from a global market share of 0.07 % in 2011 to 8.57 % in 2021³, this growth is expected to continue in the coming years. The ambition of the Dutch government is to sell only zero-emission cars from 2030.⁴ One of the main benefits of battery powered vehicles is that they can store energy from renewable sources relatively efficiently. In an extensive part of the world, electric cars already emit less greenhouse gasses compared to fossil fuel cars, which will improve even further with more renewable energy in the energy mix.⁵ While the purchase price of electric cars is still relatively high, in the current decade the difference in purchase price between a new electric car and a petrol car is expected to disappear and the driving range is expected to be comparable.

1.2. LI-ION BATTERIES TOWARDS SOLID-STATE BATTERIES

The ability of Li-ion batteries to reversibly store large amounts of energy has made them the major driver of innovation in portable electronics and battery electric vehicles. The importance of Li-ion batteries is highlighted by the Nobel prize of 2019 by John Goodenough, Stanley Whittingham and Akira Yoshino for their crucial roles in the discovery of the Li-ion battery.⁶ Li-ion batteries particularly consist of three main parts, the negative electrode, positive electrode (here referred to as anode and cathode as usually done in the battery literature) and electrolyte, a schematic figure of a Li-ion battery with solid electrolyte, and Li-metal anode is shown in Figure 1.1. In a Li-ion battery, Li-ion ions are exchanged between the anode and cathode. The driving force of this reaction is the chemical potential difference between the anode and cathode. The chemical potential is the energy that is gained or released if the particle number of a given species changes in a material. In case Li resides in the anode it has a relatively high chemical potential, which is related to high potential energy. If the Li atom resides in the cathode it has a lower chemical potential and thus lower potential energy. The difference between the

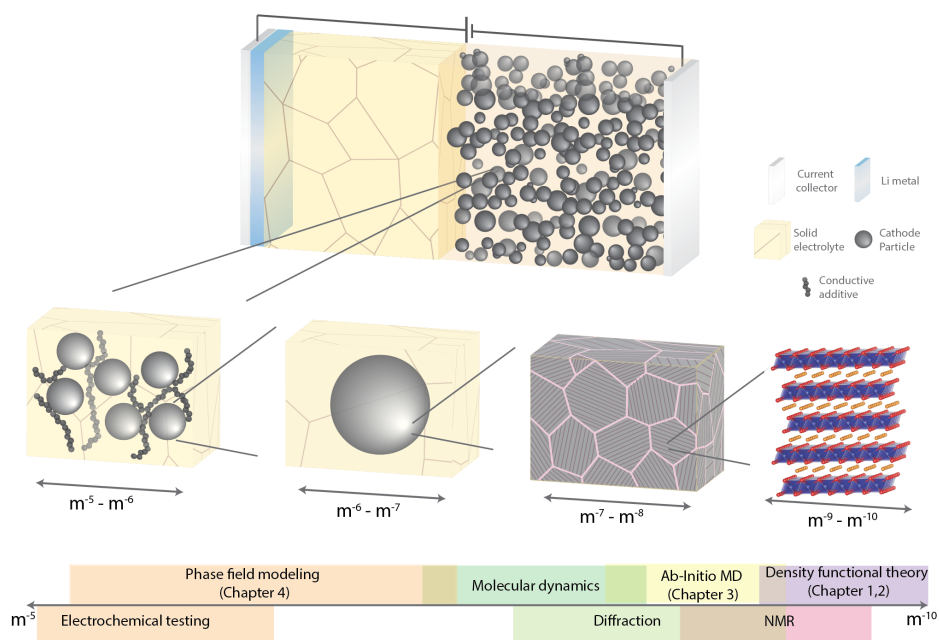


Figure 1.1: Schematic representation of a solid-state battery with relevant length scales.

chemical potentials gives rise to the voltage, which is correlated to the gain in energy if Li moves from the anode to the cathode. As nature tends to move to the lowest energy configuration, a Li atom in the anode has the tendency to move to the cathode. By placing an electrolyte between the electrodes that blocks electrons and passes Li-ions, the Li atom is separated in a Li-ion (Li^+) and an electron (e^-). During a discharge, the electron moves from the anode through the current collector and a wire to the cathode, the Li-ion moves through the electrolyte to the cathode, where the Li-ion and electron are reunited again. This is a spontaneous process as energy is gained. In the opposite process energy is required to force the Li atom back to the anode, which is the charging process.

Most electrolytes in commercial Li-ion batteries consist of an organic liquid with Li salt dissolved. These liquid electrolytes have as main advantage that they conduct lithium ions relatively fast ($\sim 10^{-2}$ S/cm) and have a relatively good electrochemical stability (1-4.2 V)⁷. However, liquid electrolytes have the disadvantage of being flammable, which can result in fire accidents.⁸ Furthermore, there is always the desire of improving the performance of the batteries regarding cycle life, energy density, power density, stability and operating conditions.⁸ These features are all related to the specific battery chemistry and can be improved by investigating new electrolyte materials, as well as cathode and anode materials.

Solid-state batteries, using a solid electrolyte, have great advantages over conventional liquid electrolyte batteries. One of the main advantages is safety, unlike liquid electrolyte batteries inorganic all-solid-state batteries are non-flammable reducing most of the safety issues. In addition, less packaging materials are required and different elec-

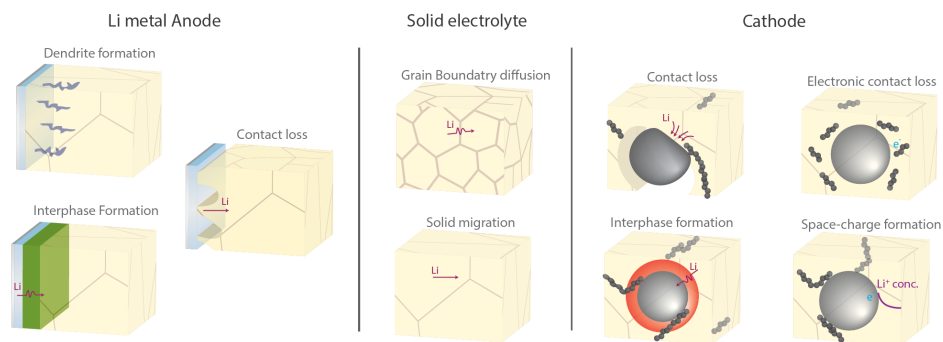


Figure 1.2: Main challenges in solid-state batteries.

trode/electrolyte combinations are possible which could potentially increase the gravimetric and volumetric energy density.⁷ In Figure 1.1 a schematic representation of a solid-state battery is shown. The battery consists of a metallic anode, a solid electrolyte and a porous cathode. The cathode itself is composed of the solid electrolyte, conductive additive and cathode particles, where the solid electrolyte and conductive additive are generally added to provide additional electronic and ionic conduction. On the far left and right current collectors accept and donate electrons from and to the external circuit.

Various types of solid electrolytes are studied in literature ranging from oxides, sulfides, hydrides, halides and polymer electrolytes. The different groups of materials have different properties in terms of ionic conductivity, electrochemical stability and mechanical properties.⁹ For example, oxides are generally relatively stable over a wide voltage range however are difficult to integrate in batteries because of high grain boundary resistance. Whereas, sulfides are generally ductile and have low grain boundary resistance but have a smaller stability window. A single solid electrolyte that possesses all relevant properties has not yet been presented but smart solutions such as multi-layer solid electrolytes, specialized coatings or adding small amounts of liquids can be used to reach high performances in (hybrid) solid-state batteries.¹⁰

One of the most pursued battery configurations in (solid-state) batteries is a Li-metal anode in combination with a high voltage metal oxide cathode, see Figure 1.1. Li-metal is considered as the 'holy grail' in batteries as it has the lowest reduction potential (0 V vs. Li/Li⁺) and high volumetric and gravimetric specific capacities (2046 mAh/cm³ and 3862 mAh/g respectively). To reach high voltages, a metal oxide cathode is placed at the cathode side, similar to used in state-of-the-art Li-ion batteries, where materials such as LiNi_{0.8}Mn_{0.1}Co_{0.1}O₂ (NMC811) are good candidates to reach high energy density solid-state batteries.

1.3. CHALLENGES IN SOLID-STATE BATTERIES

Solid-state batteries still have challenges to overcome,^{8,10} the main challenges of a Li-metal / high voltage cathode, solid-state battery are shown in Figure 1.2.

The main challenge of using Li-metal anodes is to overcome dendrite formation.¹⁰

These tree-like structures grow on the Li-metal anode, promote degradation and ultimately grow to the opposite electrode resulting in a short circuit. The better structural integrity of solid electrolytes compared to liquid electrolytes has been expected to suppress or even prevent dendrite formation, however, recent studies showed that dendrites still grow in the grains of solid-state batteries.¹¹

Another major challenge in solid-state batteries is contact loss, solids have a definite shape and when voids are present in the structure, the solid can not flow into the void as easily as liquids, which results in contact loss. Additionally, during battery operation electrode particles expand or shrink during cycling and can lose contact with the electrolyte. Here it is important to realize that only a subnanometer gap can be sufficient to completely lose contact. This has a major influence on the effective reactive area of a particle and thus on the overpotential. Besides contact loss with the electrolyte, electronic contact loss is also essential for battery operation, as for the redox reaction to take place both Li-ions and electrons are necessary.

Besides contact loss, interphase formation is one of the main challenges. Interphases are formed at the active material / electrolyte interface, which, in battery literature is often referred to as the solid electrolyte interphase or SEI. In this interphase layer Li-ion diffusion is often sluggish which limits the performance of the battery. However, when the SEI is well designed it can also be beneficial for the battery performance and serve as a protective layer between the electrolyte and electrode.

When two materials with different chemical potentials come together and do not decompose, a space-charge layer forms. The electrochemical potential equilibrates and charges will accumulate or deplete at the electrode - electrolyte interface. These space-charge layers can hinder or enhance the transport properties near interfaces. However, in most cases the effect of space-charge formation on the solid-state battery performance is predicted to be limited.¹²

1.4. MODELING OF SOLID-STATE BATTERIES

The field of modeling is expanding extremely fast because of the rapid increase in computational power that is available. With this increase larger and more detailed models can be simulated closer matching the real world. There are multiple reasons why modeling is so effective in research. The first one is control, In a computer model it is possible to change only one or a few parameters in a controlled environment, which, in an experiment is sometimes even impossible, this makes it easier to understand the underlying physical mechanisms of the problem. A second reason is that computer models consume less resources and time, computer models can often run faster than experiments without the need for expensive resources. Furthermore, models can be predictive, if a model has proven to work well for a certain problem, it can be used to predict outcomes if different variables are used. It is important to realize that computer models and experiments work hand in hand as computer models are often used to guide and understand experiments and experiments in turn are needed to validate the models.

In battery research computational modeling is widely applied.¹³ As shown in Figure 1.1, different modeling techniques are used at different length scales. At the atomic scale Density Functional Theory (DFT) is widely used. DFT is a modeling method that uses theories based on quantum mechanics to approximate the ground-state electron

density of a many-body system by approximating the Schrödinger equation. From the electron density the total energy of the system is calculated obtaining the lowest energy configuration of the system. Relevant properties for Li-ion batteries can be calculated using DFT, for example, electronic band structures, chemical potentials, formation energies and structural parameters such as atomic positions, lattice parameters and site occupancy's.

As DFT calculates a static ground state of the system, the kinetics of the system are not captured. To model the kinetics of a many-body system at the atomic scale, ab-initio molecular dynamics (MD) simulations are performed. The starting point of an MD simulation is often the lowest energy structure calculated by DFT. By applying the Born-Oppenheimer equation, and fixating the atomic nuclei, a time-independent DFT calculation can be performed to calculate the electron density, this calculated electron density provides the spatial dependent energy of the system. From the gradient of this energy map, a force field is calculated that can be applied to the atomic nuclei, where the nuclei are displaced according to the classical equation of motion. By taking the displacement of the nuclei as the starting point, a new static DFT calculation calculating the electron density can be performed. By iterating this process the displacement of atoms can be monitored and kinetic properties (e.g. ionic conductivity) of the system can be predicted.

At the microscale, DFT based approaches are computational too expensive because of the large number of atoms to be simulated. A widely used theory to simulate battery behavior at this length scale is Porous Electrode Theory (PET) developed by John Newman and coworkers.¹⁴ With PET Li-ion batteries can be modeled using the microscopical physical properties of materials, electrodes are described as particles that act as a volumetric source or sink terms residing in an electrolyte bath. In the model the specific geometry and particle size distributions of a cell can be implemented and properties such as the overpotential, electrolyte concentration and the number of active particles in the electrode can be calculated. As PET is developed to be a volume averaging approach it generally does not have accurate descriptions of phase boundaries inside the volumes of active particles. To capture these phase boundaries a more detailed thermodynamic description is developed by the group of Martin Z. Bazant and is based on modeling the free energy functional of multiphase materials, this approach is called 'multiphase porous electrode theory' (MPET)^{15,16}. This accurate description of phase boundaries is especially important for phase separating materials as LiFePO_4 , graphite and $\text{Li}_4\text{Ti}_5\text{O}_{12}$.

1.5. THE ELECTROCHEMICAL STABILITY WINDOW

THE ORIGIN OF REDOX POTENTIALS IN SOLID ELECTROLYTES

As explained in Section 1.2 interphase formation is one of the main issues in solid-state batteries. Interphase formation occurs when batteries are cycled outside the electrochemical window of the electrolyte defined by the oxidation and reduction potential of the material. In literature, the electrochemical stability is often probed by Cyclic Voltammetry (CV), where wide electrochemical windows are reported for most solid-state electrolytes (> 0-5 V)^{17,18}. This is significantly wider than the stability windows of liquid electrolytes (1-4 V)⁷. In practice however, the stability window of solid electrolytes appears

to be much more narrow and electrolyte decomposition is shown at lower voltages.¹⁹

HOW TO EXPERIMENTALLY DETERMINE THE INTRINSIC ELECTROCHEMICAL STABILITY?

The origin of this discrepancy lies in the limited contact area that is used in the CV experiments. More interfacial contact area between the current collector and the solid electrolyte pallet creates more reactive area such that the overpotential is reduced.²⁰ To increase this effective contact area between the current collector and solid electrolyte an electronic conductive additive is mixed in the solid electrolyte. By slow galvanostatic cycling of the electrolyte mixed with conductive additive the intrinsic electrochemical stability of the solid electrolyte is obtained.

WHAT ARE THE DIFFERENT DECOMPOSITION REACTION MECHANISMS IN SOLID ELECTROLYTES?

Solid electrolytes have different mechanisms to decompose: the solid electrolyte can directly decompose into decomposition products, or form an intermediate (de)lithiated phase. In this thesis it is proposed that solid electrolytes often react via this intermediate (de)lithiated phase, which can be (partly) stable, but in most cases phase separates into the decomposition products. From the evaluation of the different reaction routes for several solid electrolytes it appears that the (de)lithiated intermediate phase in most cases determines the reaction route, hence the electrochemical stability window.

HOW TO ACCURATELY PREDICT THE PRACTICAL ELECTROCHEMICAL STABILITY WINDOW?

Evaluation of the electrochemical stability by modeling also shows inconsistencies with experiments. These models are generally based on the formation energy towards the most favorable decomposition products and predict a much more limited electrochemical window (i.e. argyrodite 1.7-2 V)^{21,22} as compared to experiments (argyrodite 1.1-2.3 V). In the evaluations via the most favorable decomposition products no kinetic barriers are assumed. An evaluation of the electrochemical window via the (meta)stable (de)lithiated phases predicts, in most cases, more accurately the practical electrochemical window. In these reactions atoms do not have to diffuse far to rearrange into the favorable decomposition products, and as Li moves fast through solid electrolytes the kinetic barrier towards these (de)lithiated phases is expected to be low and therefore predicts a more realistic electrochemical stability window.

1.6. THE IONIC CONDUCTIVITY

THE ORIGIN OF IONIC CONDUCTIVITY.

Ionic conduction is enabled by the movement of cations and/or anions in a given material. It is a multi-scale process, where different length scales play important roles (Figure 1.1). At the nano-scale, three requirements enable ionic conduction: 1) Free sites are available in the crystal that charge carriers can occupy, 2) the migration energy barrier is low enough for the charge carrier to hop to the free sites and 3) the diffusion pathway should be continuous.¹⁰ The free sites are vacant positions in the crystal structure originating from defects, partial occupancies or metastable interstitials. The migration of ions can be described by three main mechanisms: a vacancy mechanism, where the ion hops through the material between vacant sites, an interstitial mechanism, where the ion hops between partial occupied sites, or a correlated mechanism, in which an ion

on a metastable position pushes an atom from an occupied site to another interstitial site. On the micro-scale, the intrinsic bulk ionic conductivity of the atomic scale is affected by factors as grain boundary resistance, porosity and contact of surfaces. Grain boundaries generally hinder the ionic migration as Li cannot move easily through the lattice mismatch. However, there are also theories that grain boundaries can enhance the conductivity, where for example along the grains local disorder or space-charge layers improve the conductivity along the boundary.²³ At the macro-scale, the combination of all effects from every length scale determines the performance of the full cell.

THE EFFECT OF DOPING ON THE IONIC CONDUCTIVITY

In literature doping is often proposed as an effective method to change relevant solid-electrolyte properties such as the electrochemical stability, air stability, elasticity, hardness, and fracture toughness^{24,25}. Doping can also affect the ionic conductivity, Kraft et al. demonstrated that aliovalent Ge doping in argyrodite $\text{Li}_6\text{PS}_5\text{I}$ enables the highest conductivity in argyrodites so far (18.4 mS/cm).²⁶ The increase in ionic conductivity by doping is often related to a flattening in the energy landscape, however a comprehensive description of the origin of this flattening is still missing.

THE ORIGIN OF IONIC CONDUCTIVITY CHANGE BY ALIOVALENT DOPING

Silicon doping in the argyrodite $\text{Li}_6\text{PS}_5\text{Br}$ structure also shows significant improvements in the ionic conductivity.²⁷ The conductivity increase in the Si-doped material is larger than only predicted by the higher Li concentration due to charge balance, hence, a more sophisticated effect should determine the increased conductivity. It is found that the excess Li in the structure resides on a previously vacant site that improves the diffusion by changing the local Li occupancy on the site by coulombic interaction effectively lowering the energy barrier for jumps through this site.

1.7. MICROSCOPIC MODEL FOR SOLID-STATE BATTERIES

A LI-ION TRANSPORT MODEL FOR SOLID ELECTROLYTES

As discussed above, Li-ion transport in solid electrolytes proceeds differently than Li transport in liquid electrolytes. In solid electrolytes for example, the anionic framework is fixed, Li hops between fixed sites and the Li concentration is generally orders of magnitude higher than in liquid electrolytes. A model based on non-equilibrium thermodynamics that captures solid-state Li-transport is essential to model these kind of systems. A modified model based on the well known regular solution model can capture solid transport where experimental or ab-initio calculated thermodynamic parameters can be implemented. The different diffusion properties of solid-state compared to diffusion in the liquid state leads to a different lithiation profile in the electrodes. Especially the lack of concentration gradients in solids changes the lithiation profile, which could enable thicker porous electrodes in solid-state batteries as compared to liquid electrolytes.

A MODEL FOR CONTACT LOSS AND SOLID ELECTROLYTE INTERPHASES IN SOLID-STATE BATTERIES

A model capturing contact loss is important to evaluate its limitations on the solid-state battery performance. Contact loss can be modeled by implementing an effective reactive

area for electrode particles. By applying a contact loss distribution to the particles in the electrode, we find that especially particles with limited contact determine the capacity retention because of the high reaction barriers for these particles to be lithiated.

As discussed in Section 1.5, interphase layers can be formed in solid-state batteries, also coatings and hybrid interlayers can be artificially applied. To evaluate the effect of an extra diffusion barrier on the battery performance additional volumes are implemented between the electrolyte and active particles, where specific physics can be modeled. As the diffusion in these interphase layers is often sluggish the effect of the conductivity on the overpotential can be evaluated. Additionally, because of the modularity of the modeling framework, different transport equations can be implemented and combinations of solid and liquid electrolytes and interphases can be simulated.

1.8. THESIS OUTLINE

The main focus of this thesis is to find the origin of the most relevant challenges of solid-state electrolytes in solid-state batteries and to capture the underlying physics of these challenges in computational models that can be generally applied.

Chapter 2 focuses on the origin of the electrochemical stability window of solid electrolytes, where especially argyrodite $\text{Li}_6\text{PS}_5\text{Cl}$, garnet $\text{Li}_7\text{La}_3\text{Zr}_2\text{O}_{12}$ and NASICON $\text{Li}_{1.5}\text{Al}_{0.5}\text{Ge}_{1.5}(\text{PO}_4)_3$ are investigated. The research suggests that the investigated solid electrolytes favor a decomposition route via (de)lithiated phases of the solid electrolyte rather than direct decomposition towards the decomposition products. First, a method to accurately measure the intrinsic electrochemical window of solid electrolytes is described. Secondly, it is shown that modeling of the electrochemical window via the (de)lithiated phases of the electrolyte accurately predicts the experimentally found stability window. Finally, the proposed mechanism is analysed by XRD and solid-state NMR.

In **Chapter 3** the practical electrochemical window and the decomposition reaction pathway is predicted for the most commonly studied solid electrolytes of different groups of solid electrolytes. Where the DFT based methodology calculating the electrochemical stability window via the (de)lithiated solid electrolyte phases as described in the previous chapter is applied. The research shows that the electrochemical stability window calculated by the (de)lithiated phases accurately predicts the redox potentials of solid electrolytes in many cases. Additionally, it is shown that solid electrolytes have specific reaction mechanisms for decomposition, these different reaction mechanisms for solid electrolytes are further investigated.

Chapter 4 investigates the origin of the ionic conductivity increase in Si-doped $\text{Li}_6\text{PS}_5\text{Br}$ argyrodite. The research suggests that the excess Li in the structure, originating from the lower valence of Si compared to P, resides on a previously unoccupied site (16e) in the $F43m$ space-group. Due to this occupation, Li atoms redistribute more homogeneously around the 16e site and neighboring (48h T5) site, effectively lowering the energy barrier to jump through this diffusion path. Because this specific jump path is the bottleneck for macroscopic diffusion the total conductivity increases with higher doping concentrations.

In **Chapter 5** a mesoscopic solid-state battery model is presented based on multi-phase porous electrode theory. A transport model for solid-state electrolytes based on

1

non-equilibrium thermodynamics is described and the differences between solid and liquid electrolyte models are investigated. Additionally, models for the main challenges of solid-state batteries are implemented in the computational framework and its effect on the battery performance is studied.

REFERENCES

- [1] International Renewable Energy Agency. IRENA, *Electricity storage and renewables: Costs and markets to 2030*, **1**.
- [2] International Energy Agency (IEA), *Evolution of Li-ion battery price, 1995-2019*, (accessed on 09-02-2022).
- [3] International Energy Agency (IEA), *Electric cars fend off supply challenges to more than double global sales*, (accessed on 09-02-2022).
- [4] Voortgangsoverleg Klimaatakkoord, *Klimaatakkoord*, (accessed on 09-02-2022).
- [5] F. Knobloch, S. V. Hanssen, A. Lam, H. Pollitt, P. Salas, U. Chewprecha, M. A. Huijbregts, and J.-F. Mercure, *Net emission reductions from electric cars and heat pumps in 59 world regions over time*, *Nature sustainability* **3**, 437 (2020).
- [6] Nobel Prize Committee, *The nobel prize in chemistry 2019*, (accessed on 09-02-2022).
- [7] J. B. Goodenough and Y. Kim, *Challenges for rechargeable li batteries*, *Chemistry of materials* **22**, 587 (2010).
- [8] J. Janek and W. G. Zeier, *A solid future for battery development*, *Nature Energy* **1**, 1 4 (2016).
- [9] A. Manthiram, X. Yu, and S. Wang, *Lithium battery chemistries enabled by solid-state electrolytes*, *Nature Reviews Materials* **2** (2017).
- [10] T. Famprikis, P. Canepa, J. A. Dawson, M. S. Islam, and C. Masquelier, *Fundamentals of inorganic solid-state electrolytes for batteries*, *Nature Materials* **18**, 1278 1291 (2019).
- [11] J. Kasemchainan, S. Zekoll, D. Spencer Jolly, Z. Ning, G. O. Hartley, J. Marrow, and P. G. Bruce, *Critical stripping current leads to dendrite formation on plating in lithium anode solid electrolyte cells*, *Nature Materials* **18**, 1105 (2019).
- [12] N. J. J. de Klerk and M. Wagemaker, *Space-charge layers in all-solid-state batteries; important or negligible?* *ACS Applied Energy Materials*, acsaem.8b01141 (2018).
- [13] A. Urban, D.-H. Seo, and G. Ceder, *Computational understanding of Li-ion batteries*, *npj Computational Materials* **2** (2016).
- [14] J. Newman and N. P. Balsara, *Electrochemical systems*, **4**, 611 (2021).
- [15] R. B. Smith and M. Z. Bazant, *Multiphase porous electrode theory*, *Journal of The Electrochemical Society* **164**, E3291 (2017).
- [16] T. R. Ferguson and M. Z. Bazant, *Nonequilibrium thermodynamics of porous electrodes*, *Journal of The Electrochemical Society* **159**, A1967 A1985 (2012).

- [17] N. Kamaya, K. Homma, Y. Yamakawa, M. Hirayama, R. Kanno, M. Yonemura, T. Kamiyama, Y. Kato, S. Hama, K. Kawamoto, and A. Mitsui, *A lithium superionic conductor*, *Nature Materials* **10**, 682 (2011).
- [18] S. Boulineau, M. Courty, J.-M. Tarascon, and V. Viallet, *Mechanochemical synthesis of Li-argyrodite $\text{Li}_6\text{PS}_5\text{X}$ ($\text{X} = \text{Cl}, \text{Br}, \text{I}$) as sulfur-based solid electrolytes for all solid state batteries application*, *Solid State Ionics* **221**, 1 (2012).
- [19] J. Auvergniot, A. Cassel, J.-B. Ledeuil, V. Viallet, V. Seznec, and R. Dedryvère, *Interface stability of argyrodite $\text{Li}_6\text{PS}_5\text{Cl}$ toward LiCoO_2 , $\text{LiNi}_{1/3}\text{Co}_{1/3}\text{Mn}_{1/3}\text{O}_2$, and LiMn_2O_4 in bulk all-solid-state batteries*, *Chemistry of Materials* **29**, 3883 (2017).
- [20] F. Han, Y. Zhu, X. He, Y. Mo, and C. Wang, *Electrochemical stability of $\text{Li}_{10}\text{GeP}_2\text{S}_{12}$ and $\text{Li}_7\text{La}_3\text{Zr}_2\text{O}_{12}$ solid electrolytes*, *Advanced Energy Materials* **6**, 1501590 (2016).
- [21] Y. Zhu, X. He, and Y. Mo, *Origin of outstanding stability in the lithium solid electrolyte materials: Insights from thermodynamic analyses based on first-principles calculations*, *ACS Applied Materials & Interfaces* **7**, 23685 (2015).
- [22] W. D. Richards, L. J. Miara, Y. Wang, J. C. Kim, and G. Ceder, *Interface stability in solid-state batteries*, *Chemistry of Materials* **28**, 266 (2016).
- [23] J. A. Dawson, P. Canepa, T. Famprikis, C. Masquelier, and M. S. Islam, *Atomic-scale influence of grain boundaries on li-ion conduction in solid electrolytes for all-solid-state batteries*, *Journal of the American Chemical Society* **140**, 362 (2018).
- [24] Z. Sun, Y. Lai, N. Lv, Y. Hu, B. Li, L. Jiang, J. Wang, S. Yin, K. Li, and F. Liu, *Insights on the properties of the O-doped argyrodite sulfide solid electrolytes ($\text{Li}_6\text{PS}_{5-x}\text{ClO}_x$, ($x = 0-1$))*, *ACS Applied Materials & Interfaces* **13**, 54924 54935 (2021).
- [25] Z. Fu, L. Zhang, J. E. Gritton, G. Godbey, T. Hamann, Y. Gong, D. McOwen, and E. Wachsman, *Probing the mechanical properties of a doped $\text{Li}_7\text{La}_3\text{Zr}_2\text{O}_{12}$ garnet thin electrolyte for solid-state batteries*, *ACS Applied Materials & Interfaces* **12**, 24693 (2020).
- [26] M. A. Kraft, S. Ohno, T. Zinkevich, R. Koerver, S. P. Culver, T. Fuchs, A. Senyshyn, S. Indris, B. J. Morgan, and W. G. Zeier, *Inducing high ionic conductivity in the lithium superionic argyrodites $\text{Li}_{6+x}\text{P}_{1-x}\text{Ge}_x\text{S}_5\text{I}$ for all-solid-state batteries*, *Journal of the American Chemical Society* **140**, 16330 (2018).
- [27] N. Minafra, S. P. Culver, T. Krauskopf, A. Senyshyn, and W. G. Zeier, *Effect of Si substitution on the structural and transport properties of superionic Li-argyrodites*, *Journal of Materials Chemistry A* **6**, 645 651 (2018).

2

CLARIFYING THE RELATIONSHIP BETWEEN REDOX ACTIVITY AND ELECTROCHEMICAL STABILITY IN SOLID ELECTROLYTES

This chapter has been published as: **Schwiertert, T. K.**[†], Arszelewska[†], V.A., Wang, C., Yu, C., Vasileiadis, A., de Klerk, N.J., Hageman, J., Hupfer, T., Kerkamm, I., Xu, Y. and van der Maas, E., Kelder, E.M., Ganapathy, S., Wage-maker, M., *Clarifying the relationship between redox activity and electrochemical stability in solid electrolytes*, [Nature Materials](#) **19**, 4 (2020). († Co first author)

2.1. ABSTRACT

ALL-SOLID-STATE Li-ion batteries promise safer electrochemical energy storage with larger volumetric and gravimetric energy densities. A major concern is the limited electrochemical stability of solid electrolytes and related detrimental electrochemical reactions, especially because of our restricted understanding. Here we demonstrate for the argyrodite, garnet and NASICON type solid electrolytes, that the favourable decomposition pathway is indirect rather than direct, via (de)lithiated states of the solid electrolyte, into the thermodynamically stable decomposition products. The consequence is that the electrochemical stability window of the solid electrolyte is significantly larger than predicted for direct decomposition, rationalizing the observed stability window. The observed argyrodite metastable (de)lithiated solid electrolyte phases contribute to the (ir)reversible cycling capacity of all-solid-state batteries, in addition to the contribution of the decomposition products, comprehensively explaining solid electrolyte redox activity. The fundamental nature of the proposed mechanism suggests this is a key aspect for solid electrolytes in general, guiding interface and material design for all-solid-state batteries.

2.2. INTRODUCTION

All-solid-state batteries (ASSBs) are attracting ever increasing attention due to their high intrinsic safety, achieved by replacing the flammable and reactive liquid electrolyte by a solid electrolyte.¹ In addition, a higher energy density in ASSBs may be achieved through; (a) bipolar stacking of the electrodes, which reduces the weight of the non-active battery parts and (b) by potentially enabling the use of a Li-metal anode, which possesses the maximum theoretical Li capacity and lowest electrochemical potential (3860 mAhg⁻¹ and -3.04 V vs. SHE). First of all, the success of ASSBs relies on solid electrolytes with a high Li-ion conductivity.²⁻⁴ A second prerequisite, is the electrochemical stability at the interfaces of the solid electrolyte with the electrode materials in the range of their working potentials. Any electrochemical decomposition of the solid electrolyte may lead to decomposition products with poor ionic conductivity that increase the internal battery resistance²⁻⁵. Third, ASSBs require mechanical stability as the changes in volume of the electrode materials upon (de)lithiation, as well as decomposition reactions at the electrode-electrolyte interface may lead to contact loss, also increasing the internal resistance and lowering the capacity.²⁻⁴

Initially, for many solid electrolytes wide electrochemical stability windows were reported^{4,6-9}, which appeared in practice to be much more limited^{4,10,11}. Evaluation of the electrochemical stability, based on differences in formation energies, indeed led to much narrower stability windows^{12,13}, however, practical stability windows typically appear larger^{4,10,11}. As a thermodynamic evaluation cannot predict kinetic barriers for decomposition reactions, the mechanisms of solid electrolyte decomposition are poorly understood, presenting one of the major challenges for ASSBs^{4,10,11}. Another important aspect, directly related to this, is the potentially significant contribution of the typically Li-rich solid electrolytes through (de)lithiation reactions, either directly or indirectly¹⁴. In general, redox activity can be expected near the interface between the solid electrolyte and the electronically conductive components of the electrode (electrode active mate-

rial and carbon additives¹⁵), but may also extend deep into the solid electrolyte through short range electron conductivity of the electrolyte itself¹⁶. Understanding the redox activity of solid electrolytes, and its correlation with the electrochemical stability window is of fundamental importance for the development of stable solid-solid interfaces in ASSBs.

Here, we demonstrate that the electrochemical stability window of the argyrodite $\text{Li}_6\text{PS}_5\text{Cl}$ solid electrolyte is determined by the solid electrolyte redox activity, that is, lithiation upon reduction of phosphorus and delithiation upon oxidation of sulfur, before decomposing into more stable products. As demonstrated by DFT simulations, this kinetically favourable indirect decomposition pathway effectively widens the electrochemical stability window, compared to direct decomposition into stable products, in excellent agreement with accurate electrochemical measurements. The (de)lithiated argyrodite phases are directly observed with XRD and solid state NMR, providing direct evidence of this indirect decomposition mechanism. As solid electrolytes are designed to provide fast ionic conduction, the indirect decomposition through (de)lithiation is proposed to be relevant for solid electrolytes in general, determining the practical electrochemical stability window. This is further validated by the agreement between the measured and the predicted indirect decomposition mechanism for $\text{Li}_7\text{La}_3\text{Zr}_2\text{O}_{12}$ (LLZO) garnet type and $\text{Li}_{1.5}\text{Al}_{0.5}\text{Ge}_{1.5}(\text{PO}_4)_3$ (LAGP) NASICON type solid electrolytes. This mechanism establishes that not only the decomposition products, but also the solid electrolyte structure itself contribute to the reversible capacity in ASSBs, making the present findings highly relevant for the working and development of ASSBs.

2.3. RESULTS

The electrochemical stability, especially for thiophosphate solid electrolytes, was shown to be significantly lower than initially expected^{8,15,17–20}, where the consequential decomposition reactions have had a large impact on the ASSB performance^{9,19–22}. To investigate the electrochemical stability and the role of electrochemical reactions in solid electrolytes, the argyrodite $\text{Li}_6\text{PS}_5\text{Cl}$ (LPSC), introduced by Deiseroth et al.²³, is employed both as active material and solid electrolyte in ASSBs. To induce oxidation and reduction reactions of the solid electrolyte, carbon black and carbon nano-fibres are mixed in with the LPSC. The mixture is referred to as the LPSC-C electrode (for details see the methods section 2.5). To study the oxidation and reduction independently, while at the same time preventing the redox activity of the decomposition products from interfering with the decomposition itself, individual cells are prepared for the first oxidation and for the first reduction respectively. An $\text{In}|\text{LPSC}|\text{LPSC-C}$ battery is cycled galvanostatically starting with oxidation, and a $\text{Li-In}|\text{LPSC}|\text{LPSC-C}$ battery starting with reduction, the resulting voltage curves of which are shown in Figure 2.1a,b. Unless otherwise specified, all voltages are expressed vs. Li/Li^+ . On galvanostatic oxidation, the LPSC-C electrode shows a voltage plateau at 2.5 V (Figure 2.1a), reaching a total charge capacity of 264 $\text{mAh g}_{\text{LPSC}}^{-1}$ when charged to 3.63 V. On galvanostatic reduction, the LPSC-C electrode shows a voltage plateau at around 1.2 V (Figure 2.1b), with a discharge capacity of 405 $\text{mAh g}_{\text{LPSC}}^{-1}$ when discharged to 0.63 V. The large partially reversible specific capacities demonstrate that LPSC can undergo severe oxidation and reduction reactions, and the low columbic efficiencies of 70 and 40% upon first oxidation and reduction, respectively,

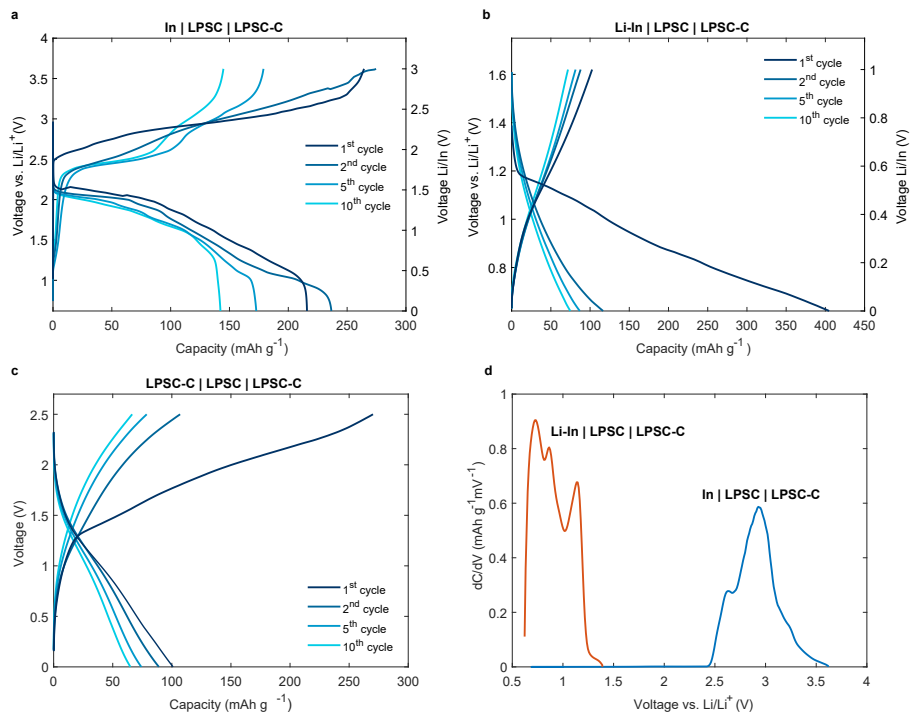


Figure 2.1: Voltage profiles and differential capacity curve of the $\text{Li}_6\text{PS}_5\text{Cl-C}$ electrode. a-c, Voltage profile of the 1st, 2nd, 5th and 10th cycle of a **a** In|LPSC|LPSC-C ASSB starting from charge, **b** Li-In|LPSC|LPSC-C ASSB starting from discharge and **c** LPSC-C|LPSC|LPSC-C, a one material (LPSC) ASSB. **d**, The differential capacity $\frac{dC}{dV}$ curve of the In|LPSC|LPSC-C (blue) and a Li-In|LPSC|LPSC-C battery (orange) showing the first oxidation and first reduction of LPSC. Electrochemical activity is observed below 1.25 V and above 2.50 V vs. Li/Li^+ , indicating an electrochemical stability window of 1.25 V.

suggest the formation of a significant amount of decomposition products. The decreasing capacity of the initial cycles (Appendix A.1) indicates that these decomposition reactions increase the impedance. However, upon extended cycling, the reversible capacity remains relatively constant, which could indicate that the decomposition products are able to deliver reversible electrochemical activity, as already suggested for LPSC by Auvergnot et al.²⁴, and worked out in detail by Tan et al.²⁵ Since LPSC can undergo both oxidation and reduction reactions, it can be used to assemble a one-material-battery, similar to what was reported for the $\text{Li}_{10}\text{GeP}_2\text{S}_{12}$ solid electrolyte, for which the combination of decomposition products at the cathode and anode provided the reversible redox¹⁴. The assembled LPSC-C|LPSC|LPSC-C symmetric one-material-battery shows an initial charge capacity of 270 $\text{mAh g}_{\text{LPSC}}^{-1}$ shown in Figure 2.1c, which drops to 107 $\text{mAh g}_{\text{LPSC}}^{-1}$ in the second cycle. During the first charge the activity appears to set in at around 1.25 V, a direct indication of the practical electrochemical stability window. To evaluate the practical electrochemical stability window more accurately, the differential

capacity is determined from the 1st charge of the In|LPSC|LPSC-C battery and from the 1st discharge of the Li-In|LPSC|LPSC battery, shown in Figure 2.1d. Indeed, a practical stability window of 1.25 V is obtained, much larger than that theoretically predicted (0.3 V)^{12,13}, and much smaller than initially reported (7 V)⁸. Additionally, the presence of more than one peak, both on reduction and oxidation, indicates subsequent redox activity. This raises the question; what reactions take place and how do these determine the observed electrochemical stability window?

Aiming for better understanding and prediction of practical electrochemical stability windows, and correlation with solid electrolyte redox activity, we evaluate the formation energies of all possible Li-vacancy configurations at different compositions of argyrodite $\text{Li}_x\text{PS}_5\text{Cl}$, within a (charge neutral) single unit cell, similar to how the energetics of electrode materials are evaluated²⁶. This appears to be a realistic approach considering that the solid electrolyte is in contact with the conductive additives in a cathodic mixture, and therefore the solid electrolyte can function as an electrode material being oxidized and reduced. Argyrodite $\text{Li}_x\text{PS}_5\text{Cl}$ crystallizes in the $F43m$ space group and at $x = 6$ has 50 % of the 48h crystallographic Li positions occupied.⁵ By calculating the energies of the symmetrically non-equivalent Li configurations, the most stable $\text{Li}_x\text{PS}_5\text{Cl}$ configurations are obtained, from which the voltage at which these phases are formed can be determined (see computational details in the methods section 2.5). Argyrodite starting structure was obtained from literature where a thorough investigation of the most stable configuration is performed²⁷.

The resulting formation energies of the argyrodite $\text{Li}_x\text{PS}_5\text{Cl}$ as a function of Li-composition are shown in Figure 2.2a, where the convex hull connects the most stable configurations. Upon oxidation and reduction of $\text{Li}_6\text{PS}_5\text{Cl}$ the most stable compositions are $\text{Li}_4\text{PS}_5\text{Cl}$ and $\text{Li}_{11}\text{PS}_5\text{Cl}$, respectively. Upon oxidation of argyrodite, sulfur is redox active ($\text{S}^{2-} \rightarrow 2\text{S}^0 + 2e^-$) whereas upon reduction, phosphorous is redox active ($\text{P}^{5+} \rightarrow \text{P}^0 - 5e^-$). Also indicated in Figure 2.2a are the energies of the thermodynamically more stable combinations of Li_3PS_4 , Li_2S and LiCl species, and the most stable decomposition products of the oxidized and reduced argyrodite. Clearly, a delithiated (oxidized) argyrodite ($\text{Li}_4\text{PS}_5\text{Cl}$) is much less stable than the combination of Li_3PS_4 , S and LiCl , as previously predicted^{12,13}, which are therefore the expected decomposition products on oxidation^{12,13}. Similarly, lithiated (reduced) argyrodite ($\text{Li}_{11}\text{PS}_5\text{Cl}$) is much less stable than the combination of P, Li_2S and LiCl ^{12,13}, which are therefore the expected decomposition products on reduction^{12,13}.

The average voltages, calculated from the convex hull, as a function of Li composition x in $\text{Li}_x\text{PS}_5\text{Cl}$ are shown in Figure 2.2b. From the theoretical voltage curve it is expected that the argyrodite LPSC delithiates (oxidizes) at 2.24 V and lithiates (reduces) at 1.08 V. This indicates that, if the decomposition reactions for oxidation and reduction are determined by the stability of the $\text{Li}_4\text{PS}_5\text{Cl}$ and $\text{Li}_{11}\text{PS}_5\text{Cl}$ species respectively, an electrochemical stability window of 1.16 V is expected. Also indicated is the much narrower electrochemical stability window, approximately 0.3 V wide, based on direct decomposition into Li_3PS_4 , S and LiCl (oxidation) and into Li_3PS_4 , Li_2S and LiCl (reduction), in line with previous DFT calculations^{12,13}. Which stability window applies, depends on the activation barriers to these decomposition routes. Based on the high Li-ion conductivity of the argyrodite, indicating low kinetic barriers for changes in the Li-composition, we pro-

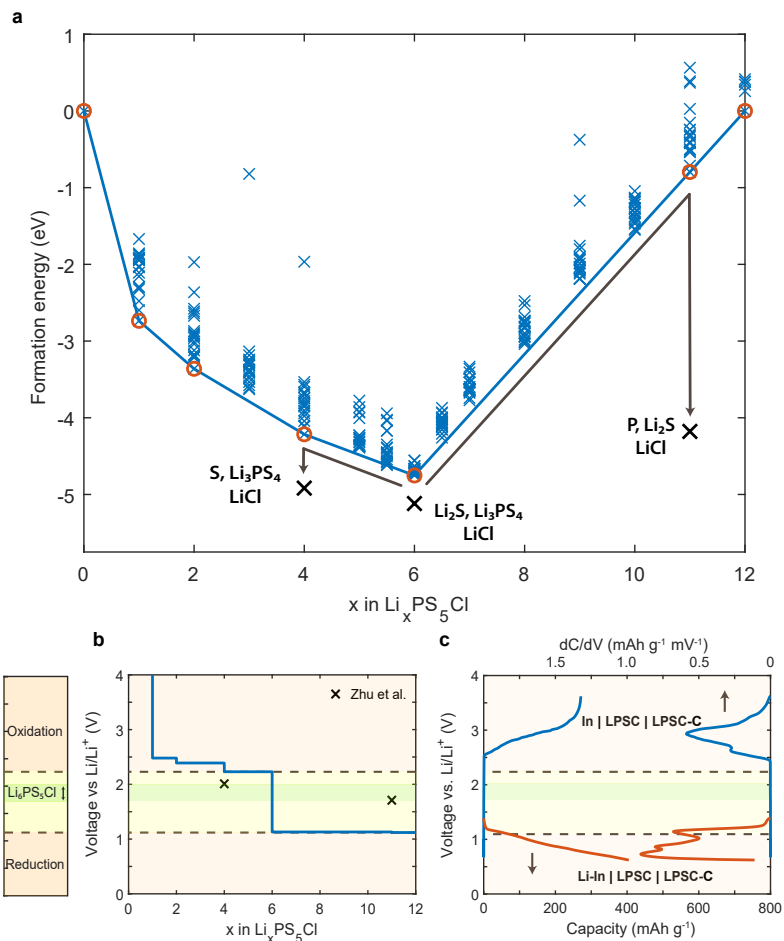


Figure 2.2: Formation energies of Li-vacancy configurations of $\text{Li}_x\text{PS}_5\text{Cl}$ and comparison of experimental and calculated voltage profiles. **a**, Formation energies per formula unit for all symmetrically non-equivalent Li configurations within one unit cell, versus the composition x in $\text{Li}_x\text{PS}_5\text{Cl}$. The formation energy of the combination of Li_3PS_4 , Li_2S and LiCl is shown below the convex hull at $x = 6$. At $x = 4$ and $x = 11$ the formation energies of the decomposition products upon oxidation (S , Li_3PS_4 , LiCl) and upon reduction (P , Li_2S and LiCl) respectively, are shown, in line with the decomposition products previously reported¹². **b**, Calculated theoretical voltage profile, vs. Li/Li^+ , of $\text{Li}_x\text{PS}_5\text{Cl}$ in the compositional range of $0 < x < 12$. Reduction and oxidation are expected to occur at 1.08 V and 2.24 V vs. Li/Li^+ , respectively. The crosses indicate the voltages at which the argyrodite is expected to decompose, upon oxidation to S , Li_3PS_4 , LiCl , and upon reduction to P , Li_2S and LiCl , previously reported¹². **c**, First charge of the In|LPSC|LPSC-C (blue) and first discharge of the Li-In|LPSC|LPSC-C battery (orange) including the differential capacity from Figure 2.1d. Above 2.50 V vs. Li/Li^+ LPSC is oxidized, and below 1.25 V vs. Li/Li^+ LPSC is reduced. The legend compares the stability windows. Yellow: Present stability window of LPSC based on the oxidation and reduction potentials of $\text{Li}_4\text{PS}_5\text{Cl}$ and $\text{Li}_{11}\text{PS}_5\text{Cl}$, respectively. Green: Predicted window (thermodynamic equilibrium towards decomposition products), based on the stability of the decomposition products upon oxidation (S , Li_3PS_4 , LiCl) and reduction (P , Li_2S and LiCl)^{12,13}.

pose that the decomposition occurs indirectly, via the lithiated and delithiated compositions of argyrodite ($\text{Li}_4\text{PS}_5\text{Cl}$ and $\text{Li}_{11}\text{PS}_5\text{Cl}$), rather than directly into the decomposition products. Upon argyrodite oxidation and reduction, first $\text{Li}_4\text{PS}_5\text{Cl}$ and $\text{Li}_{11}\text{PS}_5\text{Cl}$ would form, which are most likely unstable as evaluated below, providing a facile reaction pathway towards the formation of the more stable decomposition products as indicated by the solid black arrows in Figure 2.2a.

The experimental voltage curves obtained on oxidation and reduction of the argyrodite, including their differential capacity, are shown for comparison in Figure 2.2c. Remarkable agreement is found between the predicted electrochemical stability window of 1.16 V (Figure 2.2b) and the experimentally observed window (Figure 2.2c), supporting the present hypothesis that the argyrodite stability is determined by its redox activity upon (de)lithiation. The offset between the measured and predicted stability window is most likely a result of the lower voltages predicted by DFT calculations²⁸. Based on this, we propose that the first oxidation peak in the differential capacity, shown in Figure 2.1d and Figure 2.2c, is associated with the decomposition of LPSC at around 2.24 V via $\text{Li}_4\text{PS}_5\text{Cl}$ into Li_3PS_4 , S and LiCl, and the first reduction peak in the differential capacity with the decomposition of LPSC at around 1.08 V via $\text{Li}_{11}\text{PS}_5\text{Cl}$ into P, Li_2S and LiCl.

On further oxidation, after the formation of Li_3PS_4 via $\text{Li}_4\text{PS}_5\text{Cl}$, thermodynamic evaluation predicts the formation of P_2S_5 at 2.3 V.¹² Further reduction, after formation of P via $\text{Li}_{11}\text{PS}_5\text{Cl}$, thermodynamic evaluations predicts the formation of Li_3P , resulting in several voltage plateau's starting from 1.3 V down to approximately 0.87 V. The latter represents 67% of the reduction capacity (LiP to Li_3P) (see Appendix Table A.1, consistent with previous DFT predictions²⁹). This provides a complete prediction of the oxidation and reduction potential pathway, via the solid electrolyte to the redox activity of the decomposition products as illustrated by Appendix Figure A.2. For reduction this is consistent with the observed reduction activity measured at around 0.8 V in Figure 2.2c, and with the known reduction potentials associated with the lithiation of phosphorus³⁰. However, upon oxidation of the expected Li_3PS_4 decomposition product, a peak in the differential capacity is observed around 2.9 V, which is not in agreement with the predicted P_2S_5 formation at 2.3 V. As discussed below, formation of $\text{P}_2\text{S}_7^{4-}$ is observed, consistent with the P-S-P bridging polyhedral suggested by XPS²⁴. Moreover, Li_3PS_4 has been observed to oxidize at 2.9 V towards of $\text{P}_2\text{S}_7^{4-}$ ³¹ consistent with the observed oxidation activity shown in Figure 2.1d and 2.2b. We anticipate that to predict the oxidation of Li_3PS_4 to $\text{P}_2\text{S}_7^{4-}$ at 2.9 V requires a comprehensive DFT redox activity analysis as done here for LSPC.

To evaluate the kinetic stability of the delithiated ($\text{Li}_4\text{PS}_5\text{Cl}$) and lithiated ($\text{Li}_{11}\text{PS}_5\text{Cl}$) phases, DFT based molecular dynamics (MD) simulations are performed. It is important to realize that the timescale at which these structural transformations can be evaluated is limited, up to 100 picoseconds at present, and therefore sluggish transformations fall outside the scope of this evaluation. The radial distribution functions and corresponding (de)lithiated structures of $\text{Li}_x\text{PS}_5\text{Cl}$ with $x = 4, 6,$ and 11 after the MD simulations are shown in Figure 2.3. In the delithiated phase, $\text{Li}_4\text{PS}_5\text{Cl}$, the S atoms at the 4a and 4c positions bond to the PS_4 groups, demonstrated by a decrease in the intensity at $r = 4.1 \text{ \AA}$ and an increase of intensity at $r = 2.1 \text{ \AA}$ (Figure 2.3a), consistent with experimental observation where S bonds PS_4 groups^{18,19}. Because the PS_x units move relative to each other

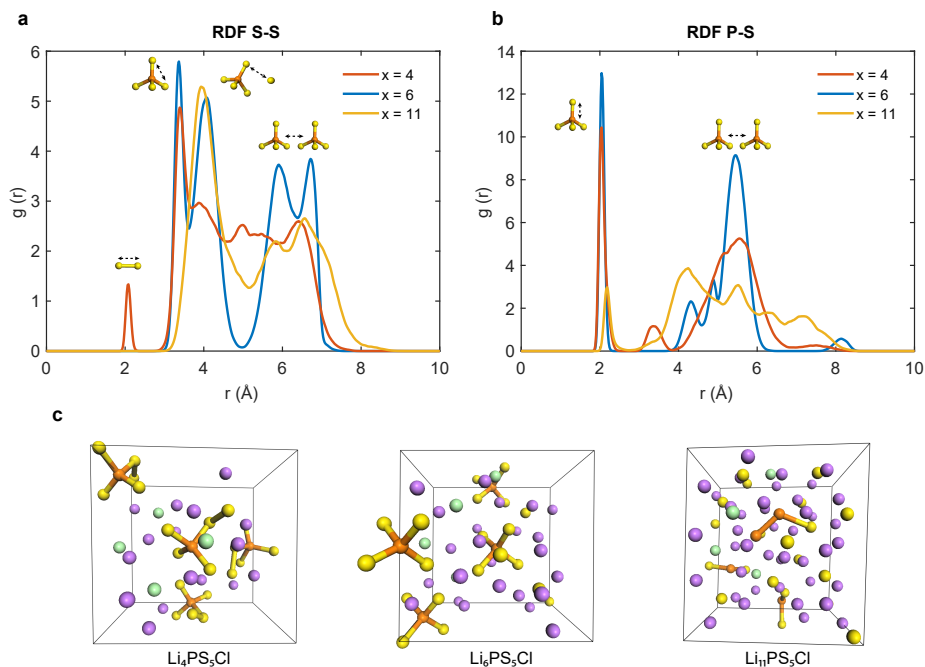


Figure 2.3: Molecular dynamics simulations of $\text{Li}_4\text{PS}_5\text{Cl}$, $\text{Li}_6\text{PS}_5\text{Cl}$ and $\text{Li}_{11}\text{PS}_5\text{Cl}$ **a**, Radial distribution function (RDF) of the S-S bonds in (de)lithiated $\text{Li}_x\text{PS}_5\text{Cl}$ for $x = 4, 6,$ and 11 during a 400 K DFT-MD simulation. During delithiation an increase in S-S bonds is seen around 2.1 \AA , indicating that the formation of S-S bonds originates from the oxidation of S in the argyrodite. On top of the peaks, bonds at corresponding radii are displayed. **b**, Radial distribution function (RDF) of the P-S bonds of (de)lithiated $\text{Li}_x\text{PS}_5\text{Cl}$ for $x = 4, 6$ and 11 during a 400 K DFT-MD simulation, showing a decrease of P-S bonds in PS_4 units, indicating the reduction of P occurs in the argyrodite. **c**, Relaxed structures of $\text{Li}_x\text{PS}_5\text{Cl}$ for $x = 4, 6$ and 11 after a 400 K DFT-MD simulation. The pink, orange, yellow and green spheres indicate lithium, phosphorous, sulfur, and chlorine respectively. In the $\text{Li}_4\text{PS}_5\text{Cl}$ structure it is seen that the S atoms at the 2a and 2c positions make S-S bonds with PS_4 groups, while in the $\text{Li}_{11}\text{PS}_5\text{Cl}$ structure it is seen that the P-S bonds break upon reduction of P.

in $\text{Li}_4\text{PS}_5\text{Cl}$, there is a peak broadening for $r > 5 \text{ \AA}$. For the lithiated phase, $\text{Li}_{11}\text{PS}_5\text{Cl}$, a drop in intensity is observed at $r = 2.1 \text{ \AA}$ (Figure 2.3b), consistent with breaking P-S bonds in the PS_4 groups. This is expected because the P atoms can compensate for the change in valence as a consequence of the lithiation. The peak broadening of the lithiated structures indicates disorder in the S positions, resulting in a less defined structure in the simulated cell. In contrast, but as expected, no structural changes are observed for LPSC, reflecting its metastability versus Li_3PS_4 , Li_2S and LiCl (see also Figure 2.2a). The MD simulations indicate that the $\text{Li}_4\text{PS}_5\text{Cl}$ and $\text{Li}_{11}\text{PS}_5\text{Cl}$ compositions are extremely unstable, having very low activation barriers towards decomposition. This supports the presently proposed indirect decomposition reaction, via the facile oxidation and reduction of the argyrodite towards the $\text{Li}_4\text{PS}_5\text{Cl}$ and $\text{Li}_{11}\text{PS}_5\text{Cl}$ phases, respectively, further decomposing into the oxidative (Li_3PS_4 , S and LiCl) and reductive (P, Li_2S and LiCl) decomposition products. In true equilibrium the convex hull predicts that $\text{Li}_x\text{PS}_5\text{Cl}$ ($4 < x$

< 6 and $6 < x < 11$) phases will separate to $\text{Li}_4\text{PS}_5\text{Cl}$, $\text{Li}_6\text{PS}_5\text{Cl}$ and $\text{Li}_{11}\text{PS}_5\text{Cl}$. At a very local scale, the $\text{Li}_4\text{PS}_5\text{Cl}$ and $\text{Li}_{11}\text{PS}_5\text{Cl}$ phases will form upon oxidation and reduction, initiating the rapid decomposition. For example, as indicated in the MD simulations $\text{Li}_4\text{PS}_5\text{Cl}$ corresponds to the local formation of S-S bonds, and hence oxidizing S^{2-} to S^0 locally, which is the starting point for the rapid decomposition. Therefore, even though complete particles in the $\text{Li}_4\text{PS}_5\text{Cl}$ and $\text{Li}_{11}\text{PS}_5\text{Cl}$ compositions should not be expected, it is these local concentrations that will facilitate as the starting point of decomposition, defining the electrochemical stability of the solid electrolyte.

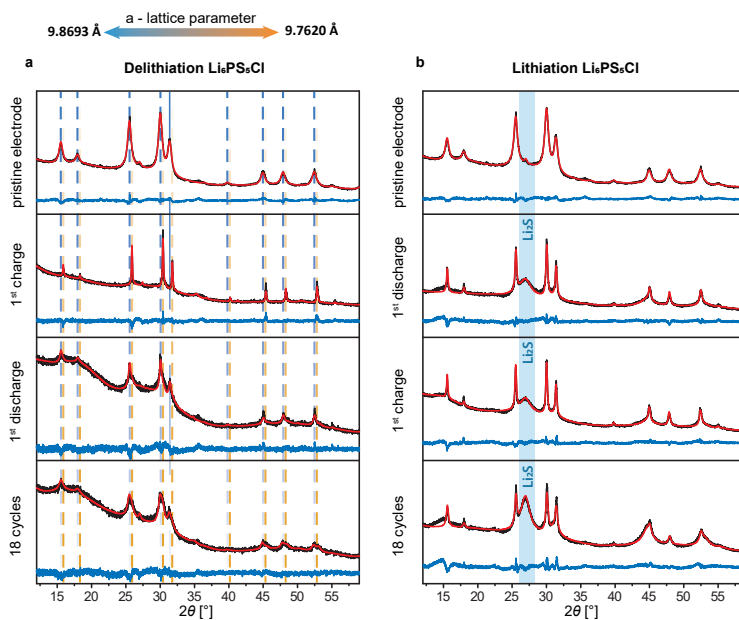


Figure 2.4: XRD patterns and fits of the LPSC-C electrodes before and after cycling. All the patterns are fit with the Rietveld method as implemented in GSAS³². **a**, XRD patterns for the In|LPSC|LPSC-C battery after 1st charge to 3.63 V vs Li/Li⁺, after subsequent discharge to 0.63 V vs Li/Li⁺ and after 18 full cycles. **b**, XRD patterns for the Li-In|LPSC|LPSC-C battery after 1st discharge to 0.63 V vs Li/Li⁺, after subsequent charge to 1.63 V vs Li/Li⁺ and after 18 full cycles.

To monitor the structural changes of LPSC-C electrodes, XRD measurements are performed at different stages during the cycling of both the In|LPSC|LPSC-C and Li-In|LPSC|LPSC-C batteries as shown in Figure 2.4, following the cycling shown in Figure 2.1a,b. After the 1st half cycle, both on oxidation and reduction, a decrease in peak width is observed, indicating an increase in average crystallite size. The average crystallite size increases from 13 nm to 80 nm on delithiation (Figure 2.4a) and to 41 nm on lithiation (Figure 2.4b) respectively. An increase in average particle size can be rationalized by the preferential decomposition of smaller particles, most likely due to their large surface areas and resulting shorter electronic pathways for oxidation and reduction. This implies that electronic transport occurs through the argyrodite solid over tens of nanometers

(the size of argyrodite particles). Upon subsequent cycling, the argyrodite XRD peaks widen, which may indicate partial decomposition of larger particles as well as a distribution of argyrodite lattice parameters as discussed below.

2

During the oxidation (delithiation) of the LPSC-C electrode to 3.63 V, the LPSC peak positions shift (Figure 2.4a), corresponding to a decrease in the average cubic lattice parameter from 9.87 Å to 9.76 Å. This can be attributed to the partial delithiation of the LPSC phase, consistent with the lattice volume changes predicted by DFT for the compositional range $4 \leq x \leq 6$ for $\text{Li}_x\text{PS}_5\text{Cl}$ (Appendix Figure A.3). Interestingly, several argyrodite compositions between $\text{Li}_4\text{PS}_5\text{Cl}$ and $\text{Li}_{11}\text{PS}_5\text{Cl}$ are located slightly above the convex hull (only 7.5 meV per atom for $\text{Li}_5\text{PS}_5\text{Cl}$) as seen in Figure 2.2a. Based on the convex hull in Figure 2.2a, these metastable phases $4 \leq x \leq 6$ should disproportionate into $\text{Li}_4\text{PS}_5\text{Cl}$ (which would decompose immediately) and LPSC. However, in reality, the system will not be in thermodynamic equilibrium as some parts of the electrodes are, or can become, more isolated through poor ionic and/or electronic contact. This makes it reasonable to suggest that parts of the electrode can be captured in $4 \leq x \leq 6$ metastable phases (which are kinetically more stable as compared to the $\text{Li}_4\text{PS}_5\text{Cl}$ and $\text{Li}_{11}\text{PS}_5\text{Cl}$ phases). Importantly, the presence of these phases in the composition range $4 \leq x \leq 6$ provides experimental support for the proposed indirect decomposition mechanism via (de)lithiation of the solid electrolyte. After subsequent reduction, hence after one complete charge–discharge cycle, two different phases of argyrodite appear to be present, indicated by the dashed lines in Figure 2.3a. The diffraction angle, 2θ , of the first phase (blue line) shifts back to the pristine argyrodite position, indicating that at least a partially reversible (de)lithiation of LPSC occurs. The second phase (orange line) remains at the position representing the delithiated argyrodite phases, the amount of which appears to grow upon cycling, indicating an increasing amount of oxidized argyrodite phases are formed upon cycling. The total amount of crystalline argyrodite decreases as indicated by the increasing background that appears over cycling, indicating the formation of amorphous sulfides and phosphorous sulfides decomposition products.

During the first reduction (lithiation) of the LPSC-C electrode to 0.63 V, the XRD patterns (Figure 2.4b) do not display an obvious peak shift. A growing peak at around 27° reflects the formation of the Li_2S phase, consistent with the predicted decomposition reaction of lithiated (reduced) argyrodite ($\text{Li}_{11}\text{PS}_5\text{Cl} \rightarrow \text{P} + 5 \text{Li}_2\text{S} + \text{LiCl}$). The amount of the Li_2S phase that is formed increases dramatically as a function of cycle number, also indicating the continued decomposition of the argyrodite for low potential cycling.

Complementary to the XRD measurements, solid-state ^6Li and ^{31}P MAS NMR measurements are performed to analyze the decomposition products formed upon cycling. For pristine argyrodite, the ^{31}P resonance at 85 ppm, shown in Figure 2.5a,d, can be assigned to the P environment in the PS_4 tetrahedral units²³. After the 1st oxidation (delithiation) to 3.63 V of the LPSC-C electrode, an additional shoulder is observed at 95 ppm (Figure 2.5b) which can be assigned to the ^{31}P environment of $\text{P}_2\text{S}_7^{4-}$ species^{33–35}. This indicates the formation of S-S bonds between PS_4 tetrahedral units (P-S-S-P), which undergoes a disproportionation reaction leading to the formation of $\text{P}_2\text{S}_7^{4-}$ and S^0 , with P-S-P bridging polyhedra¹⁸. On 1st oxidation, the ^6Li NMR spectrum (Appendix Figure A.8b) shows the formation of an additional shoulder at around -1.1 ppm consistent

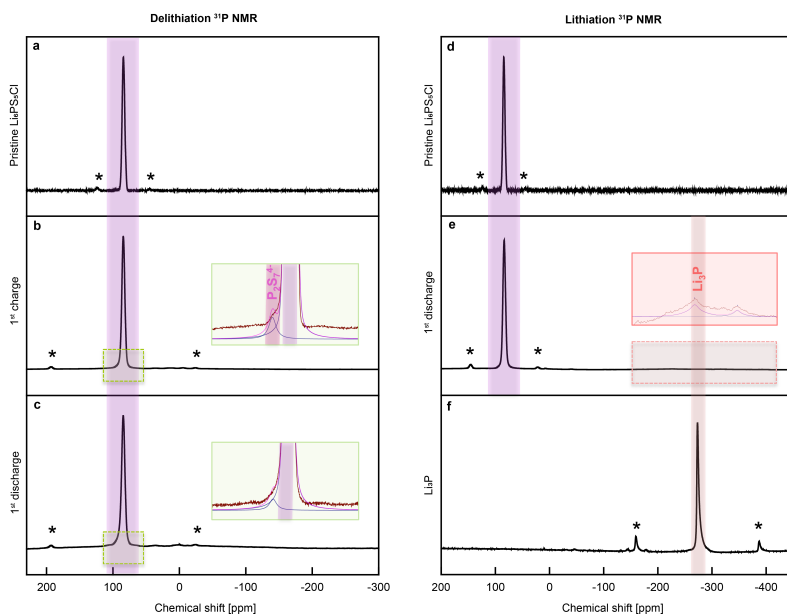


Figure 2.5: Solid-state ^{31}P NMR spectra of pristine, oxidized and reduced LPSC-C. a-f, ^{31}P MAS NMR of oxidative (a-c) and reductive (d-f) activity of LPSC in In|LPSC|LPSC-C and Li-In|LPSC|LPSC-C ASSBs respectively. After the first charge, $\text{P}_2\text{S}_7^{4-}$ is found in the cathodic mixture, and after first discharge Li_3P is present in the anodic mixture, in agreement with DFT and thermodynamic predictions. Spinning sidebands are indicated with an asterisk.

with the formation of LiCl ³⁶. This supports the decomposition products observed by XPS^{21,24}, and is also in line with the MD simulations that indicate the bonding of S to PS_4 units. Note that the oxidation to Li_3PS_4 , S and LiCl is proposed at 2.24 V, via the intermediate formation of $\text{Li}_4\text{PS}_5\text{Cl}$, whereas at around 2.9 V the oxidation towards $\text{P}_2\text{S}_7^{4-}$ and S^0 can be expected, all due to the S/S^{2-} redox, represented by the first and second oxidation peaks of the differential capacity (Figure 2.1d). The line broadening of the ^{31}P and ^6Li resonances of LPSC may originate from a distribution in bond angles and Li-deficient phases observed with XRD (Figure 2.4a). After a full cycle i.e. 1st oxidation to 3.63 V followed by reduction to 0.63 V, the intensity of the amount of $\text{P}_2\text{S}_7^{4-}$ decreases, whereas in the ^6Li NMR spectrum, a new Li-environment appears at 0.44 ppm which can be assigned to Li_3PS_4 (Appendix Figure A.8c,d). This indicates that the P-S-P bridges connecting the PS_4 units, forming upon oxidation, break upon reduction transforming them back to isolated PS_4 units, similar to what was reported for the Li_3PS_4 electrolyte^{18,19,37}.

On the 1st reduction (lithiation) to 0.63 V of the LPSC-C electrode, a new ^{31}P environment appears at -220 ppm (Figure 2.5e) which can be assigned to Li_3P (Figure 2.5f). The ^6Li NMR spectrum (Appendix Figure A.8f), shows the appearance a Li chemical environment very similar to that of Li in the argyrodite. Although the ^6Li chemical shift of this environment is close to that of Li_2PS_3 , the associated phosphorus environment at 109 ppm is not observed in Figure 2.5e. We suggest that this Li environment may repre-

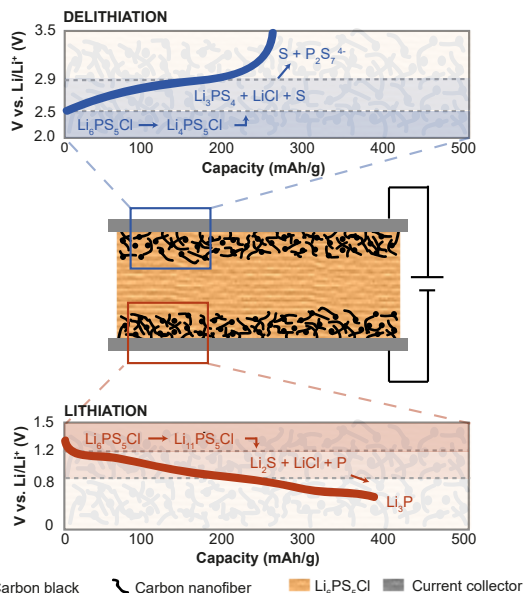


Figure 2.6: Schematic of the electrochemical activity of $\text{Li}_6\text{PS}_5\text{Cl}$ upon oxidation (delithiation) and reduction (lithiation). The electrochemical stability window is determined by the oxidation and reduction potentials of $\text{Li}_4\text{PS}_5\text{Cl}$ (effectively S/S^{2-} redox) and $\text{Li}_{11}\text{PS}_5\text{Cl}$ (effectively P/P^{5+} redox), respectively, here shown schematically, where the activation barriers to forming these compositions are expected to be very low based on the high Li-ion conductivity. These argyrodite compositions are highly unstable, having low activation barriers, resulting in rapid decomposition into the thermodynamically more stable products. The decomposition products provide reversible capacity upon ASSB cycling. Additionally, metastable oxidized and reduced argyrodite phases form i.e. $\text{Li}_{4-x}<6\text{PS}_5\text{Cl}$ and $\text{Li}_{6-x}<11\text{PS}_5\text{Cl}$ respectively, that provide additional reversible capacity upon cycling solid state batteries.

sent disordered lithiated argyrodite phases, which are suggested to form as metastable phases, occurring just above the convex hull in Figure 2.2a. Also, an additional peak appears at 2.3 ppm in the ^6Li spectrum (Appendix Figure A.8f), which can be assigned to the formation of Li_2S , consistent with the XRD pattern in Figure 2.4b. After a full cycle i.e. 1st reduction to 0.63 V followed by oxidation to 1.63 V, Li_3P disappears, indicating that in this voltage range phosphorous is redox active, reversibly transforming Li_3PS_4 to Li_3P . The observed formation of Li_3P and Li_2S in the LPSC-C electrodes reduced to 0.63 V, is consistent with XPS observations showing the formation of Li_3P , Li_2S and LiCl species, at the interface of LPSC with Li-metal²⁰. The formation of P, Li_2S and LiCl , through the decomposition of the intermediate $\text{Li}_{11}\text{PS}_5\text{Cl}$, is expected to occur at 1.08 V, and further reduction up to 0.63 V will result in the formation of Li_3P at around 0.8 V³⁰ as observed and predicted (Figure 2.2).

The proposed indirect oxidative and reductive decomposition of the argyrodite LPSC solid electrolyte, via the unstable $\text{Li}_4\text{PS}_5\text{Cl}$ (S/S^{2-} redox) at 2.24 V and $\text{Li}_{11}\text{PS}_5\text{Cl}$ (through the P/P^{5+} redox) at 1.08 V, is schematically shown in Figure 2.6. These redox potentials of the argyrodite solid electrolyte determine the practical electrochemical stability window,

as expressed by the first oxidation and reduction reactions observed in the cycling (Figure 2.1a,b), and in the differential capacity (Figure 2.1d), consistent with the predicted redox activity (Figure 2.2). These unstable argyrodite phases rapidly decompose into the expected stable Li_3PS_4 , S and LiCl species after oxidation, and P, Li_2S , and LiCl species after reduction. These decompose upon further oxidation and reduction to $\text{P}_2\text{S}_7^{4-}$ and S^0 at 2.9 V³¹ and Li_3P at 0.8 V^{12,13} respectively, as observed by XPS^{18,19} and the present XRD and NMR analysis. XRD and NMR also demonstrate the presence of metastable (de)lithiated argyrodite phases. This provides direct evidence of the proposed decomposition route, via the redox activity of the argyrodite solid electrolyte, which determines the electrochemical stability window. Both the redox activity of the solid electrolyte and of the decomposition products are responsible for the observed cycling capacity at anodic and cathodic potentials. In ASSBs this implies that both contributions of the solid electrolyte, will add to the cycling capacity based on the active electrode materials and the specified potential ranges. Moreover, the poor ionic conductivity of the decomposition products, especially S, Li_2S and LiCl, as well as the change in volume can be expected to be responsible for the large increase in interfacial resistance upon cycling^{20,38,39}.

The practical reversible and irreversible electrochemical activity, of the electrolyte in ASSBs, either originating from decomposition reactions or from the solid electrolyte itself, depends to a large extent on the electronic contact with the current collector which in turn depends on the electrode morphology. The redox activity of the solid electrolyte is expected at its contact areas with the electronically conductive cathode material and conductive carbon additive, but may also extend deep into the solid electrolyte itself, as solid electrolytes may be able to conduct electrons over small distances, as demonstrated for instance for Li_3PS_4 ¹⁶. In line with that the present detailed XRD analysis shows that decomposition reactions are not limited to the near interface area, as complete, tens of nanometer large, solid electrolyte particles decompose.

To support the general nature of the indirect decomposition mechanism, the Li insertion/extraction potentials are also determined computationally and experimentally for two different families of solid electrolytes i.e. garnet LLZO and NASICON LAGP, shown in Figure 2.7. For LLZO, the predicted and measured oxidation are both located just above 3.5 V, significantly larger than the direct decomposition at 2.91 V towards the predicted stable decomposition products Li_2O_2 , La_2O_3 and $\text{Li}_6\text{Zr}_2\text{O}_7$.¹² For LAGP, the predicted and measured oxidation occur close to 2.31 V, which is lower than direct decomposition at 2.70 V based on the stability of the predicted decomposition products Ge, GeO_2 , $\text{Li}_4\text{P}_2\text{O}_7$ and AlPO_4 .¹² These results support that the proposed indirect, kinetically favorable decomposition, via the (de)lithiation of the solid electrolyte is a general mechanism, in practice widening the solid electrolyte stability window.

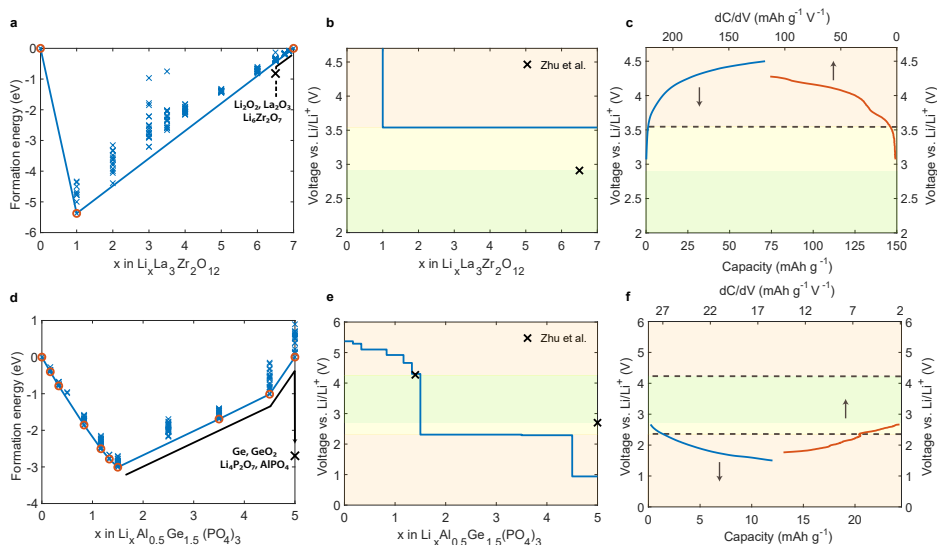


Figure 2.7: Formation energies of Li-vacancy configurations of garnet $\text{Li}_7\text{La}_3\text{Zr}_2\text{O}_{12}$ (LLZO) and NASICON $\text{Li}_{1.5}\text{Al}_{0.5}\text{Ge}_{1.5}(\text{PO}_4)_3$ (LAGP) solid electrolytes and comparison of experimental and calculated oxidation potentials a, d Formation energies per formula unit of $\text{Li}_x\text{La}_3\text{Zr}_2\text{O}_{12}$ for $0 \leq x \leq 7$ and for $\text{Li}_x\text{Al}_{0.5}\text{Ge}_{1.5}(\text{PO}_4)_3$ $0 \leq x \leq 5$. The formation energy of the decomposition products are indicated with a black cross. It is unlikely that oxidation will proceed to $\text{Li}_1\text{La}_3\text{Zr}_2\text{O}_{12}$ as suggested by the convex hull, because several compositions between $x=7$ and $x=6$ (in $\text{Li}_x\text{La}_3\text{Zr}_2\text{O}_{12}$) are located marginally above the convex hull. This suggests that in the presence of slightly higher potentials (>3.54 V), oxidation will lead to indirect decomposition via $x=6.5$, towards the predicted stable decomposition products Li_2O_2 , La_2O_3 and $\text{Li}_6\text{Zr}_2\text{O}_7$ ¹². **b, e** The calculated voltage based on the convex hull of $\text{Li}_x\text{La}_3\text{Zr}_2\text{O}_{12}$ and $\text{Li}_x\text{Al}_{0.5}\text{Ge}_{1.5}(\text{PO}_4)_3$. The blue line represents the redox potentials of the solid electrolytes, and the potentials for direct oxidation/reduction into the decomposition products are indicated with a black cross¹². The green area indicates the stability window assuming direct decomposition, defined by the black cross, and yellow the extended stability window based on the presently proposed indirect decomposition via (de)lithiation of the solid electrolyte. **c, f** Experimental voltage curve and differential capacity upon first oxidation of a Li|Liquid-Electrolyte|LLZO-C battery and first reduction of a Li|Liquid-Electrolyte|LAGP-C battery. The differential capacity shows that oxidation of LLZO occurs around 3.6 V and reduction of LAGP occurs around 2.4 V, both in good agreement with the predicted stability window based on the indirect decomposition via (de)lithiation of the solid electrolytes. The specific capacities are calculated based on the weight of LLZO and LAGP respectively. Notably, the reduction of LLZO and the oxidation of LAGP are not considered at present because both the indirect and direct reduction result in practically the same potential, making it impossible to discriminate between the two different mechanisms.

2.4. CONCLUSION

As solid electrolytes are designed for high ionic conductivity, the activation energies for oxidation and reduction reactions, associated with delithiation and lithiation respectively, can be expected to be small. The resulting metastable solid electrolyte compositions provide a kinetically facile reaction intermediate, providing an indirect pathway towards the more stable solid electrolyte decomposition products. As a consequence, the electrochemical stability window is determined by the solid electrolyte oxidation and reduction potentials (S and P redox for argyrodite and several other thiophosphate based solid electrolytes, O and Zr redox for LLZO and O and P redox for LAGP), and not by the stability of the most stable solid electrolyte decomposition products. The consequence of this indirect thermodynamic pathway, is that the electrochemical stability window is generally wider than that based on only on the stability of the decomposition products. The fundamental nature of the present decomposition mechanism, through the (de)lithiation of the solid electrolyte, suggests that it is highly relevant for solid electrolytes in general which will be further examined in Chapter 3. Based on the mechanism, the design of stable solid electrolytes and their interfaces should focus on maximizing (de)lithiation redox potentials of the solid electrolytes. The demonstrated relation between the solid electrolyte electrochemical stability window and the redox reactions of the electrolyte, are decisive for the performance of solid state batteries and provide understanding that will contribute to the design electrolyte-electrode interfaces in ASSBs.

2.5. MATERIALS AND METHODS

SYNTHESIS

Argyrodite $\text{Li}_6\text{PS}_5\text{Cl}$ (LPSC) was synthesized as described in detail elsewhere⁴⁰. Appropriate amounts of Li_2S (99.9%, Alfa Aesar), P_2S_5 (99%, Sigma-Aldrich) and LiCl (99.0%, Sigma-Aldrich) were ball-milled at 110 rpm for 2 h under argon atmosphere. The mixture was then transferred to quartz tubes and annealed at 550 °C for 15 h in order to get the pure phase of the argyrodite $\text{Li}_6\text{PS}_5\text{Cl}$ (Appendix Figure A.6).

SOLID-STATE BATTERY ASSEMBLY AND ELECTROCHEMICAL CYCLING

The electrode mixture was prepared by ball milling argyrodite with carbon (Super P, TIMCAL) and carbon nanofibres (Sigma Aldrich) in a weight ratio of 0.70 : 0.15 : 0.15 for 6 h at 450 rpm in a ZrO_2 coated stainless steel jar with 8 ZrO_2 balls. The solid electrolyte and electrodes were then cold pressed under 4 tons/cm² in a solid-state cell. In a cell, 10 mg of LPSC-C electrode was used and pressed against 180 mg of electrolyte^{40,41}. Cycling was performed in an argon filled glove box, in order to avoid reactions with oxygen and moisture. The ASSBs were cycled galvanostatically with a current density of 5.5 mA/cm² within a voltage window of 0 – 3 V vs. Li/In for In|LPSC|LPSC-C, 0 – 1 V vs. Li/In for Li-In|LPSC|LPSC-C and 0 – 2.5 V for LPSC-C|LPSC|LPSC-C respectively. To evaluate the practical electrochemical stability window more accurately, the differential capacity is determined from the 1st charge of the In|LPSC|LPSC-C battery and from the 1st discharge of the Li-In|LPSC|LPSC-C battery. Often cyclic voltammetry (CV) is used to determine the experimental stability window. However, the relatively short exposure time

to the decomposition potentials in combination with the typically sluggish decomposition reactions make it challenging to evaluate the electrochemical stability window with CV cycling. In contrast, the differential capacity, determined from the slow galvanostatic charge and discharge profiles of individual oxidation and reduction processes is effective in determining the practical electrochemical stability window, in particular when the solid electrolyte is used as an active electrode material.

To measure the oxidative and reductive stability of LLZO and LAGP an NMP (Sigma Aldrich) based electrode slurry was prepared by ball-milling active material (LLZO Ta-doped, D50 = 400 – 600 nm, Ampcera, LAGP, Ampcera), with carbon black (Super P, TIMCAL), PVDF binder (polyvinylidene fluoride, Solef PVDF, Solvay) in weight ratio 0.4 : 0.5 : 0.1 for 90 min at 250 rpm in ZrO₂ coated stainless steel jar with 8 ZrO₂ balls. A blank test was prepared using carbon black (Super P, TIMCAL) as active material and PVDF as a binder in the weight ratio 0.9 : 0.1 to result in the same carbon black loading as the LLZO and LAGP electrodes. The slurry was cast on Al foil with a thickness of 100 μm and dried at 60 °C in vacuum oven for 12h. The loading of the LLZO, LAGP and carbon electrodes was 1.6 mg/cm², 1.0 mg/cm² and 0.6 mg/cm² respectively. The coin cells were assembled in an argon filled glove box, in order to avoid reactions with oxygen and moisture (< 0.1 ppm O₂ and < 2 ppm H₂O) using both a polymer (Celgard 2250) and glass fiber (Whatman) separator and lithium metal as a counter electrode (Sigma Aldrich), which is washed with dimethyl carbonate (DMC) to remove the oxide layer and 400 μl of 1.0 M LiPF₆ in 1:1 v/v ethylene carbonate (EC) and diethyl carbonate (DEC) (<15 ppm H₂O, Sigma Aldrich) was added as an electrolyte for wetting both working and counter electrode surfaces. Galvanostatic oxidation was performed with cut-off voltage of 4.5 V (vs. Li/Li⁺) for first oxidation (LLZO-C) and 1.5 V (vs. Li/Li⁺) for first reduction (LAGP-C) with 12 hours of rest and charge/discharge current of 7.0 μA. Comparison of the galvanostatic oxidation and reduction of the LLZO-C and LAGP-C electrodes and blank electrode are provided in Appendix Figures A.4 and A.5. With the solid electrolyte – carbon mixtures, very large interface areas are achieved (for the current particle sizes » 1 m²) making the effective current densities at least 4 orders of magnitude lower than the current densities based on the electrode diameter.

X-RAY DIFFRACTION

To identify the crystalline phases of the prepared materials, powder XRD patterns were collected in the 2θ range of 10-120° using Cu KαX-rays (1.5406 Å at 45 kV and 40 mA) on an X'Pert Pro X-ray diffractometer (PANalytical). The samples were tested in an airtight sample holder, filled with argon, to prevent exposure to oxygen and moisture.

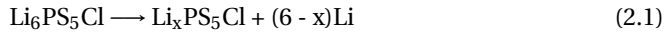
SOLID-STATE NMR

Solid-state (NMR) measurements were performed using a Bruker Ascend 500 MHz spectrometer equipped with two and three channel 4.0 mm and 3.2 mm Magnetic Angle Spinning (MAS) probes respectively. The operating frequencies for ³¹P and ⁶Li were 202.47 and 73.60 MHz respectively, and all measurements were performed within a spinning speed range of 8 to 23 kHz and π/2 pulse lengths of 4 – 5 μs were determined for ⁶Li and ³¹P. The chemical shifts of ⁶Li spectra were referenced with respect to a 0.1M LiCl solution, and ³¹P spectra with respect to an 85% H₃PO₄ solution. Based on the spin-lattice

(T_1) relaxation time, recycle delays of 5-10,000 s were utilized collecting between 128 and 11,264 scans for each sample.

COMPUTATIONAL DETAILS

To determine the energy properties of crystalline phases, Density Functional Theory (DFT) relaxations were performed with the Vienna Ab-Initio Simulation Package (VASP)⁴². The PBE exchange correlation function of Perdew et al. was implemented⁴³, and core electrons were probed with the projected-augmented wave approach (PAW)⁴⁴. A cut-off value of 280 eV and a $4 \times 4 \times 4$ k-point mesh were used. For the argyrodite, the following reaction is considered:



If $x < 6$ Li $\text{Li}_6\text{PS}_5\text{Cl}$ is oxidized, if $x > 6$ $\text{Li}_6\text{PS}_5\text{Cl}$ is reduced. Then, by calculating the energies on both sides of the reaction and taking the electrochemical potential of Li into account,

$$\bar{\mu}_{\text{Li}} = \mu_{\text{Li}} - \phi \quad (2.2)$$

with $\bar{\mu}_{\text{Li}}$ the electrochemical potential of Li, μ_{Li} the chemical potential of Li, and ϕ the electrical potential. Therefore, the average electrical potential at which oxidation/reduction takes place can be determined by:

$$\bar{\phi} = - \frac{E(\text{Li}_6\text{PS}_5\text{Cl}) - E(\text{Li}_x\text{PS}_5\text{Cl}) - (6 - x)E(\text{Li})}{6 - x} \quad (2.3)$$

where $E(\text{Li}_6\text{PS}_5\text{Cl})$ represents the composition of the most stable configurations on the convex hull. DFT-based MD simulations were performed using the same cut-off value as in DFT simulations. The ab initio MD simulations were executed in the NVT ensemble (conserving the number of atoms, volume and temperature), where the temperature scales every 1,000 time steps. The simulations use periodic boundary conditions with time steps of 2 fs, the total time of the MD simulations being 100 ps. The number of k-points was reduced from $4 \times 4 \times 4$ used in the DFT simulations to $1 \times 1 \times 1$ for the MD simulations. The lattice parameters and positions of all atoms were allowed to relax during relaxation.

The argyrodite structure was obtained from previous work.²⁷ There the Cl-S disorder over the 4a and 4c sites was investigated, and the thermodynamically most favourable configuration was obtained. Note that the Cl-S disorder was kept constant in the presented convex hull and thus the oxidation and reduction voltages were not affected. For determination of configurations as a function of the Li concentration, 10,000 structures were created by placing the appropriate number of Li ions randomly at the 48h positions. To quickly scan these for possible low-energy structures, only the electrostatic energies in these structures were calculated, using the undamped shifted force method with a cut-off radius of 15 Å (ref.⁴⁵). For the 20 lowest energy configurations of the electrostatic calculations the structure was optimized and the energy was calculated using VASP. For $\text{Li}_x\text{PS}_5\text{Cl}$, $12 \leq x \leq 15$, extra Li atoms were inserted on the 16e position, and the extended convex hull is presented in Appendix Figure A.7.

All DFT calculations were performed on charge-neutral cells, thus taking into account the true oxidation and reduction of solid electrolytes, and thus behaving similar to an electrode material. The formation energies of the thermodynamic decomposition products were taken from the Materials Project database⁴⁶. The structure of LLZO was also obtained from the Materials Project database⁴⁶. For LLZO, a $1 \times 1 \times 1$ k-point mesh was used with a cut-off value of 500 eV. The structure of LAGP was taken from the literature⁴⁷ and was relaxed using a $3 \times 3 \times 1$ k-point mesh with a cut-off value of 500 eV.

REFERENCES

- [1] J. G. Kim, B. Son, S. Mukherjee, N. Schuppert, A. Bates, O. Kwon, M. J. Choi, H. Y. Chung, and S. Park, *A review of lithium and non-lithium based solid state batteries*, *Journal of Power Sources* **282**, 299 (2015).
- [2] Z. Zhang, Y. Shao, B. Lotsch, Y.-S. Hu, H. Li, J. Janek, L. F. Nazar, C.-W. Nan, J. Maier, M. Armand, *et al.*, *New horizons for inorganic solid state ion conductors*, *Energy & Environmental Science* **11**, 1945–1976 (2018).
- [3] J. Janek and W. G. Zeier, *A solid future for battery development*, *Nature Energy* **1**, 1–4 (2016).
- [4] F. Zheng, M. Kotobuki, S. Song, M. O. Lai, and L. Lu, *Review on solid electrolytes for all-solid-state lithium-ion batteries*, *Journal of Power Sources* **389**, 198 (2018).
- [5] C. Yu, L. van Eijck, S. Ganapathy, and M. Wagemaker, *Synthesis, structure and electrochemical performance of the argyrodite $\text{Li}_6\text{PS}_5\text{Cl}$ solid electrolyte for li-ion solid state batteries*, *Electrochimica Acta* **215**, 93 (2016).
- [6] N. Kamaya, K. Homma, Y. Yamakawa, M. Hirayama, R. Kanno, M. Yonemura, T. Kamiyama, Y. Kato, S. Hama, K. Kawamoto, and A. Mitsui, *A lithium superionic conductor*, *Nature Materials* **10**, 682 (2011).
- [7] S. Ohta, T. Kobayashi, and T. Asaoka, *High lithium ionic conductivity in the garnet-type oxide $\text{Li}_{7-x}\text{La}_3(\text{Zr}_{2-x}\text{Nb}_x)\text{O}_{12}$ ($x=0-2$)*, *Journal of Power Sources* **196**, 3342 (2011).
- [8] S. Boulineau, M. Courty, J.-M. Tarascon, and V. Viallet, *Mechanochemical synthesis of Li-argyrodite $\text{Li}_6\text{PS}_5\text{X}$ ($X = \text{Cl}, \text{Br}, \text{I}$) as sulfur-based solid electrolytes for all solid state batteries application*, *Solid State Ionics* **221**, 1 (2012).
- [9] Y. Kato, S. Hori, T. Saito, K. Suzuki, M. Hirayama, A. Mitsui, M. Yonemura, H. Iba, and R. Kanno, *High-power all-solid-state batteries using sulfide superionic conductors*, *Nature Energy* **1**, 16030 (2016).
- [10] B. V. Lotsch and J. Maier, *Relevance of solid electrolytes for lithium-based batteries: A realistic view*, *Journal of Electroceramics* **38**, 128 (2017).
- [11] Y. Tian, T. Shi, W. D. Richards, J. Li, J. C. Kim, S.-H. Bo, and G. Ceder, *Compatibility issues between electrodes and electrolytes in solid-state batteries*, *Energy & Environmental Science* **10**, 1150 (2017).

- [12] Y. Zhu, X. He, and Y. Mo, *Origin of outstanding stability in the lithium solid electrolyte materials: Insights from thermodynamic analyses based on first-principles calculations*, *ACS Applied Materials & Interfaces* **7**, 23685 (2015).
- [13] W. D. Richards, L. J. Miara, Y. Wang, J. C. Kim, and G. Ceder, *Interface stability in solid-state batteries*, *Chemistry of Materials* **28**, 266 (2016).
- [14] F. Han, T. Gao, Y. Zhu, K. J. Gaskell, and C. Wang, *A battery made from a single material*, *Advanced Materials* **27**, 3473 (2015).
- [15] W. Zhang, T. Leichtweiß, S. P. Culver, R. Koerver, D. Das, D. A. Weber, W. G. Zeier, and J. Janek, *The detrimental effects of carbon additives in $\text{Li}_{10}\text{GeP}_2\text{S}_{12}$ -based solid-state batteries*, *ACS Applied Materials & Interfaces* **9**, 35888 (2017).
- [16] F. Han, A. S. Westover, J. Yue, X. Fan, F. Wang, M. Chi, D. N. Leonard, N. J. Dudney, H. Wang, and C. Wang, *High electronic conductivity as the origin of lithium dendrite formation within solid electrolytes*, *Nature Energy* **4**, 187 (2019).
- [17] F. Han, Y. Zhu, X. He, Y. Mo, and C. Wang, *Electrochemical stability of $\text{Li}_{10}\text{GeP}_2\text{S}_{12}$ and $\text{Li}_7\text{La}_3\text{Zr}_2\text{O}_{12}$ solid electrolytes*, *Advanced Energy Materials* **6**, 1501590 (2016).
- [18] R. Koerver, F. Walther, I. Ayyün, J. Sann, C. Dietrich, W. G. Zeier, and J. Janek, *Redox-active cathode interphases in solid-state batteries*, *Journal of Materials Chemistry A* **5**, 22750 (2017).
- [19] T. Hakari, M. Deguchi, K. Mitsuhara, T. Ohta, K. Saito, Y. Orikasa, Y. Uchimoto, Y. Kowada, A. Hayashi, and M. Tatsumisago, *Structural and electronic-state changes of a sulfide solid electrolyte during the Li deinsertion–insertion processes*, *Chemistry of Materials* **29**, 4768 (2017).
- [20] S. Wenzel, S. J. Sedlmaier, C. Dietrich, W. G. Zeier, and J. Janek, *Interfacial reactivity and interphase growth of argyrodite solid electrolytes at lithium metal electrodes*, *Solid State Ionics* **318**, 102 (2018).
- [21] J. Auvergniot, A. Cassel, J.-B. Ledeuil, V. Viallet, V. Seznec, and R. Dedryvère, *Interface stability of argyrodite $\text{Li}_6\text{PS}_5\text{Cl}$ toward LiCoO_2 , $\text{LiNi}_{1/3}\text{Co}_{1/3}\text{Mn}_{1/3}\text{O}_2$, and LiMn_2O_4 in bulk all-solid-state batteries*, *Chemistry of Materials* **29**, 3883 (2017).
- [22] J. Lau, R. H. DeBlock, D. M. Butts, D. S. Ashby, C. S. Choi, and B. S. Dunn, *Sulfide solid electrolytes for lithium battery applications*, *Advanced Energy Materials* **8**, 1800933.
- [23] H.-J. Deiseroth, S.-T. Kong, H. Eckert, J. Vannahme, C. Reiner, T. Zaiß, and M. Schlosser, *$\text{Li}_6\text{PS}_5\text{X}$: A class of crystalline Li-rich solids with an unusually high Li^+ mobility*, *Angewandte Chemie International Edition* **47**, 755 (2008).
- [24] J. Auvergniot, A. Cassel, D. Foix, V. Viallet, V. Seznec, and R. Dedryvère, *Redox activity of argyrodite Li_6PS_5 electrolyte in all-solid-state Li-ion battery: An XPS study*, *Solid State Ionics* **300**, 78 (2017).

- [25] D. H. S. Tan, E. A. Wu, H. Nguyen, Z. Chen, M. A. T. Marple, J.-M. Doux, X. Wang, H. Yang, A. Banerjee, and Y. S. Meng, *Elucidating reversible electrochemical redox of $\text{Li}_5\text{PS}_5\text{Cl}$ solid electrolyte*, *ACS Energy Letters* **4**, 2418 (2019).
- [26] M. Aydinol, A. Kohan, and G. Ceder, *Ab initio calculation of the intercalation voltage of lithium-transition-metal oxide electrodes for rechargeable batteries*, *Journal of Power Sources* **68**, 664 (1997).
- [27] N. J. J. de Klerk, I. Rosłoń, and M. Wagemaker, *Diffusion mechanism of Li argyrodite solid electrolytes for Li-ion batteries and prediction of optimized halogen doping: The effect of Li vacancies, halogens, and halogen disorder*, *Chemistry of Materials* **28**, 7955 (2016).
- [28] M. K. Aydinol, A. F. Kohan, G. Ceder, K. Cho, and J. Joannopoulos, *Ab initio study of lithium intercalation in metal oxides and metal dichalcogenides*, *Physical Review B* **56**, 1354 (1997).
- [29] M. Mayo, K. J. Griffith, C. J. Pickard, and A. J. Morris, *Ab initio study of phosphorus anodes for lithium- and sodium-ion batteries*, *Chemistry of Materials* **28**, 2011 (2016).
- [30] T. Ramireddy, T. Xing, M. M. Rahman, Y. Chen, Q. Dutercq, D. Gunzelmann, and A. M. Glushenkov, *Phosphorus-carbon nanocomposite anodes for lithium-ion and sodium-ion batteries*, *Journal of Materials Chemistry A* **3**, 5572 (2015).
- [31] T. Hakari, M. Nagao, A. Hayashi, and M. Tatsumisago, *All-solid-state lithium batteries with Li_3PS_4 glass as active material*, *Journal of Power Sources* **293**, 721 (2015).
- [32] A. C. Larson and R. B. V. Dreele, *General structure analysis system (GSAS)*, Los Alamos National Laboratory, Los Angeles **NM 87545**, 231.
- [33] C. Dietrich, M. Sadowski, S. Siculo, D. A. Weber, S. J. Sedlmaier, K. S. Weldert, S. Indris, K. Albe, J. Janek, and W. G. Zeier, *Local structural investigations, defect formation, and ionic conductivity of the lithium ionic conductor $\text{Li}_4\text{P}_2\text{S}_6$* , *Chemistry of Materials* **28**, 8764 (2016).
- [34] C. Dietrich, D. A. Weber, S. J. Sedlmaier, S. Indris, S. P. Culver, D. Walter, J. Janek, and W. G. Zeier, *Lithium ion conductivity in $\text{Li}_2\text{S-P}_2\text{S}_5$ glasses – building units and local structure evolution during the crystallization of superionic conductors Li_3PS_4 , $\text{Li}_7\text{P}_3\text{S}_{11}$ and $\text{Li}_4\text{P}_2\text{S}_7$* , *Journal of Materials Chemistry A* **5**, 18111 (2017).
- [35] M. Murakami, K. Shimoda, S. Shiotani, A. Mitsui, K. Ohara, Y. Onodera, H. Arai, Y. Uchimoto, and Z. Ogumi, *Dynamical origin of ionic conductivity for $\text{Li}_7\text{P}_3\text{S}_{11}$ metastable crystal as studied by $^{6/7}\text{Li}$ ^{31}P solid-state NMR*, *The Journal of Physical Chemistry C* **119**, 24248 (2015).
- [36] B. M. Meyer, N. Leifer, S. Sakamoto, S. G. Greenbaum, and C. P. Grey, *High field multinuclear NMR investigation of the SEI layer in lithium rechargeable batteries*, *Electrochemical and Solid-State Letters* **8**, A145 (2005).

- [37] H. Stöffler, T. Zinkevich, M. Yavuz, A.-L. Hansen, M. Knapp, J. Bednarčík, S. Randau, F. H. Richter, J. Janek, H. Ehrenberg, and S. Indris, *Amorphous versus crystalline Li_3PS_4 : Local structural changes during synthesis and Li ion mobility*, *The Journal of Physical Chemistry C* **123**, 10280 (2019).
- [38] C. Yu, S. Ganapathy, E. R. H. v. Eck, H. Wang, S. Basak, Z. Li, and M. Wagemaker, *Accessing the bottleneck in all-solid state batteries, lithium-ion transport over the solid-electrolyte-electrode interface*, *Nature Communications* **8** (2017).
- [39] W. Zhang, D. Schröder, T. Arlt, I. Manke, R. Koerver, R. Pinedo, D. A. Weber, J. Sann, W. G. Zeier, and J. Janek, *(Electro)chemical expansion during cycling: monitoring the pressure changes in operating solid-state lithium batteries*, *Journal of Materials Chemistry A* **5**, 9929 (2017).
- [40] C. Yu, S. Ganapathy, J. Hageman, L. van Eijck, E. R. H. van Eck, L. Zhang, T. Schwieter, S. Basak, E. M. Kelder, and M. Wagemaker, *Facile synthesis toward the optimal structure-conductivity characteristics of the argyrodite $\text{Li}_6\text{PS}_5\text{Cl}$ solid-state electrolyte*, *ACS Applied Materials & Interfaces* **10**, 33296 (2018).
- [41] C. Yu, J. Hageman, S. Ganapathy, L. van Eijck, L. Zhang, K. R. Adair, X. Sun, and M. Wagemaker, *Tailoring $\text{Li}_6\text{PS}_5\text{Br}$ ionic conductivity and understanding of its role in cathode mixtures for high performance all-solid-state Li-S batteries*, *Journal of Materials Chemistry A* **7**, 10412 (2019).
- [42] G. Kresse and J. Hafner, *Ab initio molecular dynamics for liquid metals*, *Physical Review B* **47**, 558 (1993).
- [43] J. P. Perdew, K. Burke, and Y. Wang, *Generalized gradient approximation for the exchange-correlation hole of a many-electron system*, *Physical Review B* **54**, 16533 (1996).
- [44] P. E. Blöchl, *Projector augmented-wave method*, *Physical Review B* **50**, 17953 (1994).
- [45] C. J. Fennell and J. D. Gezelter, *Is the ewald summation still necessary? Pairwise alternatives to the accepted standard for long-range electrostatics*, *The Journal of Chemical Physics* **124**, 234104 (2006).
- [46] A. Jain, S. P. Ong, G. Hautier, W. Chen, W. D. Richards, S. Dacek, S. Cholia, D. Gunter, D. Skinner, G. Ceder, and K. A. Persson, *Commentary: The materials project: A materials genome approach to accelerating materials innovation*, *APL Materials* **1**, 011002 (2013).
- [47] J. Kang, H. Chung, C. Doh, B. Kang, and B. Han, *Integrated study of first principles calculations and experimental measurements for Li-ionic conductivity in Al-doped solid-state $\text{LiGe}_2(\text{PO}_4)_3$ electrolyte*, *Journal of Power Sources* **293**, 11 (2015).

3

FIRST-PRINCIPLES PREDICTION OF THE ELECTROCHEMICAL STABILITY AND REACTION MECHANISMS OF SOLID-STATE ELECTROLYTES

This chapter has been published as: **Schwiertert, T. K.** Vasileiadis, A. and Wagemaker, M., *First-Principles Prediction of the Electrochemical Stability and Reaction Mechanisms of Solid-State Electrolytes*, [JACS Au](#) **1**, 9 (2021)

3.1. ABSTRACT

SOLID-STATE batteries have significant advantages over conventional liquid batteries, providing improved safety, design freedom, and potentially reaching higher power and energy densities. The major obstacle in the commercial realization of solid-state batteries is the high resistance at the interfaces. Essential for overcoming this bottleneck is to achieve in-depth fundamental understanding of the crucial electrochemical processes at the interface. Conventional electrochemical stability calculations for solid electrolytes, determining the formation energy towards the energetically favourable decomposition products, often underestimate the stability window because kinetics are not included. In this work, we introduce a computational scheme that takes the redox activity of the solid electrolytes into account in calculating the electrochemical stability, which in many cases appears to dictate the electrochemical stability. This methodology is applied to different chemical and structural classes of solid electrolytes, exhibiting excellent agreement with experimentally observed electrochemical stability. In contrast with current perception, the results suggest that the electrochemical stability of solid electrolytes is not always determined by the decomposition products but often originates from the intrinsic stability of the material itself. The processes occurring outside the stability window can lead towards phase separation or solid-solution depending on the reaction mechanism of the material. These newly gained insights provide better predictions of the practical voltage ranges and structural stabilities of solid electrolytes, guiding solid-state batteries toward better interfaces and material design.

3.2. INTRODUCTION

Solid-state batteries have received growing interest during the last decades due to their improved safety and potentially superior battery performance. The essential requirements for solid electrolytes are high ionic and low electronic conductivity while maintaining chemical and electrochemical stability at the anode and cathode interfaces during cycling. Several promising inorganic solid electrolytes from different material classes have been developed exhibiting high ionic conductivities. The most intensively investigated solid electrolyte structures include sulfur-based thiophosphates and thio-LISICON conductors (10^{-2} - 10^{-3} S cm⁻¹), and oxide-based solid electrolytes such as Garnets, NASICONs, Perovskite, LISICON (10^{-2} - 10^{-6} S cm⁻¹), and recently also Halides.¹⁻⁴

Besides the rapid development of solid electrolytes with high bulk Li-ion conductivities, reaching values even beyond that of liquid electrolytes, interfacial resistance between the solid electrolyte and electrode typically remains the main limiting factor in solid-state batteries.¹⁻⁵ The origin of this can include mechanical failure leading to contact loss, space-charge layers, and chemical and electrochemical instability of the solid electrolyte electrode interface.⁶ Numerous interfacial strategies have been developed to increase battery performance, but capacity retention and lower rate capability due to parasitic interface processes remain the challenge for solid-state batteries.^{3,6} These processes are complex and challenging to study experimentally, and better theoretical understanding of the electrochemical stability of solid electrolytes is a prerequisite.^{3,5,6}

More insights into the electrochemical stability window of solid electrolytes and its relationship with the decomposition mechanism have been recently obtained. For sev-

Table 3.1: Investigated solid electrolytes, including the redox element(s) on oxidation and reduction and the theoretical capacities associated with decomposition.

Material	Acronym	Redox element Oxidation	Ox. Capacity (mAh/g)	Redox element Reduction	Red. Capacity (mAh/g)
Li ₃ PS ₄	LPS	S ²⁻	96.23	P ⁵⁺	1190.78
Li ₆ PS ₅ Br	LPSB	S ²⁻ / Br ⁻	514.01	P ⁵⁺	685.35
Li ₆ PS ₅ Cl	LPSC	S ²⁻ / Cl ⁻	599.14	P ⁵⁺	798.85
Li ₁₀ GeP ₂ S ₁₂	LGPS	S ²⁻	455.20	P ⁵⁺ / Ge ⁴⁺	1081.11
LiBH ₄	LBH	B ⁵⁻	1230.55	H ⁺	4922.22
Li ₃ YBr ₆	LYB	Br ⁻	136.48	Y ³⁺	136.48
Li ₃ OCl	LOC	O ²⁻ / Cl ⁻	1112.40	-	-
Li ₂ PO ₂ N	LIPON	N ³⁻ / O ²⁻	589.95	P ⁵⁺	2359.80
Li ₇ La ₃ Zr ₂ O ₁₂	LLZO	O ²⁻	223.41	Zr ⁴⁺ / La ³⁺	255.33
Li _{0.33} La _{0.56} TiO ₃	LLTO	O ²⁻	50.27	Ti ⁴⁺ / La ³⁺	559.03
Li _{1.5} Al _{0.5} Ti _{1.5} (PO ₄) ₃	LATP	O ²⁻	105.62	P ⁵⁺ / Al ³⁺ / Ti ⁴⁺	2147.69
Li _{1.5} Al _{0.5} Ge _{1.5} (PO ₄) ₃	LAGP	O ²⁻	96.23	Ge ⁴⁺ / P ⁵⁺ / Al ³⁺	1812.34

eral solid electrolytes, it has been shown that cyclic (CV) experiments overestimate the actual electrochemical stability window^{7,8}, whereas the prediction of the thermodynamic formation energy of the decomposition products^{7,9,10} often underestimates the actual electrochemical stability window. CV experiments do not capture the electrochemical stability window accurately due to the small electrolyte-electrode contact area and the short timescale of these experiments compared to low current density solid-state battery cycling.⁸ On the other hand, the electrochemical stability window's prediction from formation energies of the decomposition products may underestimate the electrochemical stability window due to the inability of capturing the reaction mechanism and the associated reaction energy barrier towards the decomposition products, which will kinetically hinder the decomposition.

Recently, it was shown that the oxidation and reduction of several solid electrolytes, associated with delithiation and lithiation, respectively, may provide an indirect redox route, via metastable solid electrolyte composition(s), towards the most stable decomposition.⁷ In this case, the solid electrolyte acts as an active material (Li source or sink), where the associated anodic or cathodic potential determines the thermodynamic electrochemical stability window. This is only possible if the solid electrolyte is in contact with the electron-conducting network of the electrode, which can be expected to apply for the solid electrolyte material near the anode/cathode and/or near the conductive additive, where the definition of vicinity depends on the electronic conductivity of the solid electrolyte and its decomposition products, which is receiving increasing attention due to its impact on dendrite formation and decomposition.^{7,8,11,12} For the few solid electrolytes investigated, the in-this-way predicted indirect electrochemical stability window was shown to be wider than that associated with direct decomposition, matching the actual electrochemical stability window at small currents (approaching thermodynamic conditions) and supporting this indirect decomposition mechanism, which could also be qualified as kinetic stabilization.⁷

Herein, we extend and deepen this approach by predicting the electrochemical window associated with oxidation and reduction reactions (delithiation and lithiation, re-

spectively) of the most intensively studied solid electrolytes by evaluating solid electrolyte formation energies determined by density functional theory (DFT) calculations. Redox potentials for Li insertion and extraction are calculated and compared to the potentials of direct decomposition towards the most stable chemical products. The results are in good agreement with reported experimental electrochemical stability windows, predicting that the decomposition route typically proceeds via (de)lithiation of the solid electrolyte and that this indirect decomposition mechanism determines the electrochemical stability window of most solid electrolytes. In general, this results in a wider stability window than calculated based on the stability of the decomposition products, which can be rationalized by a potentially large reaction barrier for decomposition. The results are correlated to different structural responses of the solid electrolyte material to specific potentials, providing fundamental and practical insights into the structural and electrochemical stability of solid-state electrolytes.

3

3.3. METHODS

Density functional theory (DFT) using the Perdew-Burke-Ernzerhof (PBE) generalized gradient approximation (GGA) was applied to determine the lowest energy configurations of (de)lithiated materials¹³. Projected augmented wave (PAW) pseudopotentials as implemented within the Vienna Ab initio Software Package (VASP)¹⁴ are used. The k-point mesh and energy cutoff values for different materials are reported in Table A.3. All DFT calculations are performed charge neutral, taking the oxidation and reduction of the material itself as typically performed for electrode materials¹⁵.

To determine the configurations of (de)lithiated structures, the following scheme is applied. The lowest static electrostatic energy configurations are generated by minimizing the columbic interactions for Li. The above calculation is performed for 10,000 random configurations at each specific Li concentration in a material. Subsequently, for the 10 lowest energy structures, DFT relaxation is performed to obtain the final total energy and structure. To evaluate if there are energetically preferred symmetric sites for delithiation, Li concentrations at different Wyckoff positions are also evaluated. The sites where Li atoms are inserted in the materials are given in Table A.3. Structures and formation energies used as references are obtained from the Materials Project¹⁶.

3.4. RESULTS

The solid electrolytes studied are listed in Table 3.1. Sulfides generally possess a high Li conductivity and good processability but have limited electrochemical stability.³ In this study, Li_3PS_4 (LPS), thio-LISICON $\text{Li}_{10}\text{GeP}_2\text{S}_{12}$ (LGPS), argyrodites $\text{Li}_6\text{PS}_5\text{Cl}$ (LPSC), and $\text{Li}_6\text{PS}_5\text{Br}$ (LPSB) are considered. Next to sulfides, an emerging complex hydride LiBH_4 (LBH) and solid halide Li_3YBr_6 (LYB) are investigated. Halides have attained renewed interest through their combination of relatively high oxidative stability with high Li conductivity^{17,18}. In addition, solid oxide electrolytes are investigated, which are generally more electrochemically stable but have a lower ionic conductivity compared to sulfides². Specifically, anti-Perovskite Li_3OCl (LOC), Perovskite $\text{Li}_{0.33}\text{La}_{0.56}\text{TiO}_3$ (LLTO), and $\text{Li}_2\text{PO}_2\text{N}$ (LIPON) are considered.^{16,19} Finally, NASICON electrolytes, $\text{Li}_{1.5}\text{Al}_{0.5}\text{Ge}_{1.5}(\text{PO}_4)_3$ (LAGP), and $\text{Li}_{1.5}\text{Al}_{0.5}\text{Ti}_{1.5}(\text{PO}_4)_3$ (LATP) electrolytes are investigated, which have been

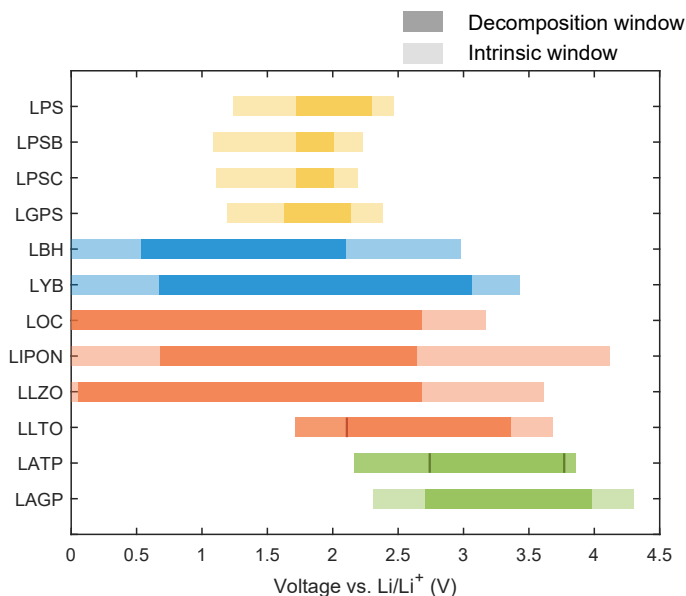


Figure 3.1: Calculated intrinsic electrochemical stability window and decomposition electrochemical stability window. For most solid electrolytes, the intrinsic oxidation and reduction voltages result in a wider stability window than the decomposition window. However, for LLTO and LATP materials, the intrinsic oxidation/reduction potential is lower/higher than the direct oxidation/reduction, indicated by the solid line.

shown to have high oxidative stability.⁹ More information about the structures used and the details of DFT relaxations are provided in the Table A.3.

In this study, two electrochemical stability windows are differentiated: (1) The electrochemical stability window, based on the stability of the decomposition products^{9,10}, referred to as the decomposition window. (2) The electrochemical stability window, based on indirect decomposition via (de)lithiation of the solid electrolyte, referred to as intrinsic window.⁹ To determine the decomposition window, the formation energy of the most favourable decomposition products at a specific potential are calculated, which are determined from the Li grand potential phase diagram.^{9,10} The decomposition potential closest to the stable solid electrolyte phase defines the reduction and oxidation redox potentials of the window. It is essential to realize that this does not consider the decomposition route, and the associated reaction barrier may lead to an overpotential necessary to form the decomposition products. The intrinsic window of a solid electrolyte is determined from the change in calculated formation energies upon Li insertion and extraction. Thus, the solid electrolyte structure is considered electrochemical active through Li insertion/extraction. The associated average oxidation/reduction potential is calculated by referencing the formation energies to the Li-metal chemical potential similar to intercalation electrodes.¹⁵ These (de)lithiated solid electrolyte phases often have a higher formation energy compared to the most favourable decomposition products (decomposition window) and therefore represent metastable or unstable phases. It is proposed that at a specific lithium composition, these solid electrolyte phases become

Table 3.2: Calculated decomposition electrochemical stability window, assuming direct decomposition to the most stable decomposition products (values in agreement with the calculations in literature⁹), and the Calculated intrinsic electrochemical stability window based on the oxidation and reduction potentials for (de)inserting lithium for different solid electrolytes.

Material	Decomposition ox/red (V)	Intrinsic ox/red (V)
LPS	1.72 – 2.30	1.24 – 2.47
LPSB	1.72 – 2.01	1.09 – 2.23
LPSC	1.72 – 2.01	1.11 – 2.19
LGPS	1.63 – 2.14	1.19 – 2.38
LBH	0.54 – 2.10	0.00 – 3.43
LYB	0.67 – 3.06	0.00 – 3.43
LOC	0.00 – 2.68	0.00 – 3.17
LIPON	0.68 – 2.64	0.00 – 4.12
LLZO	0.05 – 2.68	0.00 – 3.61
LLTO	1.71 – 3.36	2.10 – 3.68
LATP	2.17 – 3.86	2.74 – 3.77
LAGP	2.71 – 3.98	2.31 – 4.30

sufficiently unstable to enable decomposition towards the most stable decomposition products, thus representing an indirect decomposition mechanism.⁹ The calculated decomposition electrochemical stability window, assuming direct decomposition towards the most stable decomposition products, and the intrinsic electrochemical stability window, assuming indirect decomposition to the most stable decomposition products via (de)lithiation, of the solid electrolytes in Table 3.2 are shown in Figure 3.1 and listed in Table 3.2.

For the sulfide electrolytes (yellow in Figure 3.1), the intrinsic window is significantly wider than the decomposition window. This is a consequence of the assumption that direct decomposition is kinetically hindered, resulting in the indirect decomposition via (de)lithiation of the solid electrolyte, effectively resulting in kinetic stabilization of the electrochemical stability window. This assumption is supported by the better agreement of the intrinsic stability window with the experimentally observed electrochemical stability. Considering Li_3PS_4 (LPS), its intrinsic oxidative stability of 2.47 V vs. Li/Li^+ is in reasonable agreement with the experimental value of 2.6 V.²⁰ Likewise, the wider intrinsic window of LGPS amounts to 1.19–2.38 V vs. Li/Li^+ , matching the experimental stability window of around 1.2–2.5 V vs. Li/Li^+ .^{8,11} It has already been shown that the intrinsic electrochemical stability of argyrodite LPSC agrees very well with experiments⁷, and similarly, there is a good agreement with the experimentally observed oxidation at 2.5 V vs. Li/Li^+ for LPSB. These experiments were performed without extra external pressure applied after assembling and therefore pressure differences of at most several MPa are expected.²¹ This is low compared to the much larger pressures that would theoretically influence the stability window of solid electrolytes.²² In the sulfide solid electrolytes, delithiation results in oxidation of S^{2-} towards S^0 around 2.2–2.5 V vs. Li/Li^+ , as expected, similar to the potential of sulfur electrodes. Upon lithiation, P is reduced from P^{5+} to P^0 around 1.1–1.2 V vs. Li/Li^+ and further reduces to P^{3-} (Li_3P) below 0.78 V.²³ We

want to clarify again that CV experiments using sulfide solid electrolytes report voltage ranges beyond > 0.5 V^{24,25}, however, these experiments are performed without conductive additive mixed with the solid electrolyte and are thus unable to capture the intrinsic electrochemical window.⁸

Similar to sulfide electrolytes, the intrinsic window of lithium boron hydride LBH and halide LYB is significantly larger as compared to the decomposition window. For both solid electrolytes, the indirect reductive potential predicts stability towards Li metal. Electrochemical stability of the boron hydride has been shown experimentally around $0 - 3$ V vs. Li/Li⁺¹⁸, matching the intrinsic stability window calculations. For halide LYB a relatively high oxidative voltage is predicted (3.43 V), for which in a battery with LiCoO₂ as active material a higher columbic efficiency is achieved compared to sulfur electrolyte LPS.¹⁷ However, at low potentials, LYB is reduced against Li metal, whereas the intrinsic window predicts it is stable towards Li-metal. Thus, in this case, the decomposition window has a better predictive value. We propose that this is the consequence of the simple composition build from few elements, thus having a small compositional space, where Li closely surrounds Y and Br in the structure. This can be expected to result in a small nucleation barrier for direct decomposition upon reduction into Y and LiBr, and thus the practical reduction potential approaches that of the predicted decomposition stability window. The large oxidative intrinsic stability window of LBH and LYB can be attributed to the strength of BH₄⁻ and YBr₆³⁻ backbones in these structures, similar to NaBH₄, for which it has been shown that desodiation leads to larger oxidative stability as compared to direct decomposition.²⁶

In Anti-Perovskite Li₃OCl (LOC), where Li is the only element that can be reduced, the reductive decomposition stability equals the Li-metal potential⁹, making it a suitable choice for Li-metal batteries.³ The intrinsic oxidative stability, 3.17 V vs. Li/Li⁺, is for this material larger than that predicted by direct decomposition. Accurate oxidation potentials are not reported for LOC. However, the low Coulombic efficiency and formation of decomposition products in combination with LiCoO₂ suggest the stability window to be below the LiCoO₂ potential.³ The predicted intrinsic stability window of LIPON, $0.00 - 4.12$ vs. Li/Li⁺, is significantly larger than the predicted decomposition window, $0.68 - 2.64$ vs. Li/Li⁺. Consistent with the intrinsic window, it has been shown that LIPON is oxidized around 4.3 V by Put et al.²⁷. The reductive stability of LIPON against Li metal is disputed, where apparent stability against Li metal is suggested from experiments, and LIPON is even used to coat Li metal anodes effectively^{3,27-29}. Nevertheless, different studies show the reduction of P and N in contact with Li metal.^{3,30} Here, intrinsic stability against Li metal is predicted by the convex hull of LIPON, with stable configurations on the convex at Li₁PO₂N and Li₆PO₂N (Figure A.14). The compositions just above the convex represent metastable phases that may occur at small overpotentials in practice. Garnet LLZO is predicted to have an oxidation and reduction potential of 0.05 and 2.68 V vs. Li/Li⁺, respectively, assuming direct decomposition. This window is increased to $0 - 3.61$ V vs. Li/Li⁺ assuming the intrinsic decomposition. This is in excellent agreement with the observed stability against Li metal and a demonstrated oxidation potential of 3.6 V vs. Li/Li⁺ for LLZO.^{7,8,31}

The predicted intrinsic stability window is wider than the predicted direct decomposition window for the solid electrolytes discussed so far. Interestingly, for Perovskite

LLTO, the direct reduction potential to form the decomposition products is predicted to be lower than the indirect reduction via lithiation of the LLTO structure. This implies that Li-ion insertion in the LLTO structure is energetically more favorable than the formation of decomposition products. Thus lithiation should occur before decomposition. Indeed intercalation of LLTO has been demonstrated, reflecting the reduction of Ti^{4+} towards Ti^{3+} , similar to, for instance, $\text{Li}_4\text{Ti}_5\text{O}_{12}$ electrodes³², demonstrating that the indirect stability window is not always wider than the window predicted based on direct decomposition. The oxidative potential of LLTO is predicted to be larger than that for direct decomposition, and as expected, similar compared to oxide electrolytes.

3

That the intrinsic window can be smaller than the direct electrochemical stability window is also demonstrated by NASICON type LAMP. As shown in Figure 3.1, LAMP has an intrinsic stability window more narrow than its decomposition window, resulting from the lower oxidation potential upon delithiation and higher reduction potential upon lithiation. This reveals that similar to LLTO, Li-ion insertion is predicted to occur before decomposition upon reduction, and Li-ion extraction is predicted to occur before decomposition upon oxidation. In Figure 3.2a, the many compositions on, or just above the convex hull, both upon lithiation (reduction) and delithiation (oxidation), indicate solid solution reactions in both cases, representing a gradual and homogeneous change in lithium composition in chemical potential, and thus in the oxidation and reduction potentials. Upon reduction, this is supported by experiments, demonstrating that intercalation of $\text{Li}_{1+x}\text{Al}_x\text{Ti}_{2-x}(\text{PO}_4)_3$ sets in at 2.5 V vs. Li/Li^+ , which gradually reduces during continuous reduction³³. Figure 3.2b displays the structure of LAMP ($\text{Li}_{1.5}\text{Al}_{0.5}\text{Ti}_{1.5}(\text{PO}_4)_3$) as well as the completely delithiated $\text{Al}_{0.5}\text{Ti}_{1.5}(\text{PO}_4)_3$ and lithiated structures $\text{Li}_3\text{Al}_{0.5}\text{Ti}_{1.5}(\text{PO}_4)_3$ (Ti is fully reduced from Ti^{4+} to Ti^{3+}) after DFT relaxation. In the lithiated LAMP structure, the rhombohedral lattice remains intact, and only minor reorientations of PO_4 groups can be observed. Similar distortions in symmetry are observed experimentally during the lithiation of LAMP, where the reduction of Ti leads to symmetry lowering of the lithiated samples from $R\bar{3}c$ to $R\bar{3}$. During oxidation, where lithium is extracted from the structure, the oxidation voltage towards the first point on the convex hull is 3.37 V. Also, upon delithiation to $\text{Al}_{0.5}\text{Ti}_{1.5}(\text{PO}_4)_3$, structural relaxation indicates that the rhombohedral structure is maintained. Without evaluating the chemical stability of $\text{Al}_{0.5}\text{Ti}_{1.5}(\text{PO}_4)_3$, we anticipate this to be stable based on the predicted chemical stability of rhombohedral $\text{Ti}_2(\text{PO}_4)_3$ (0.013 eV per atom above the hull).¹⁶ Here, it should be noticed that the supercell size determines the Li-composition step in the convex hull. The intrinsic window limits in Figure 3.1 and Table 3.2 are thus artificially defined by the smallest composition step of the supercell considered. These results imply that LAMP is electrochemically unstable at a smaller intrinsic window, however, whether the decomposition products form depends on the structural stability and reversibility upon (de)lithiation, similar to what insertion electrodes experience during cycling.

Indeed, structurally reversible lithiation and delithiation have been experimentally shown for LAMP, resulting in a gradual change in intercalation potential, consistent with a solid solution reaction.³⁴ This implies that the structural stability of the solid electrolyte extends beyond the electrochemical stability window. The intrinsic window defines when (de)lithiation occurs, which generally reduce the Li-ion and may increase

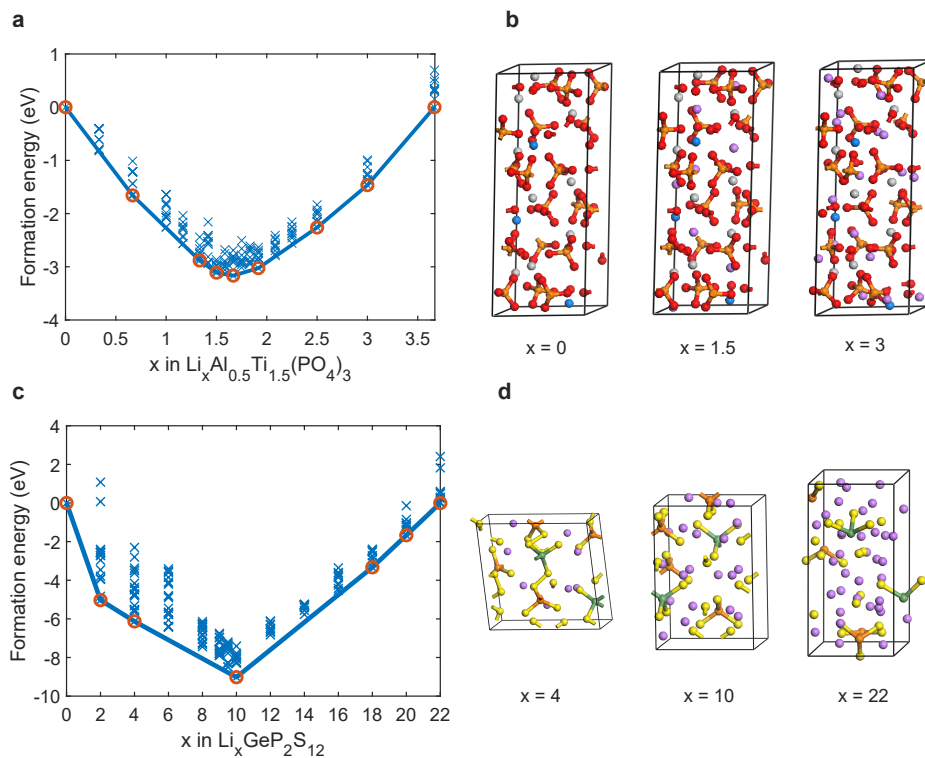


Figure 3.2: Formation energies of Li-vacancy configurations of $\text{Li}_x\text{Al}_{0.5}\text{Ti}_{1.5}(\text{PO}_4)_3$ and $\text{Li}_x\text{GeP}_2\text{S}_{12}$ with corresponding (de)lithiated structures after DFT relaxation. **a** Formation energies per formula unit of $\text{Li}_x\text{Al}_{0.5}\text{Ti}_{1.5}(\text{PO}_4)_3$ (LATP) with **b** corresponding structures after DFT relaxations for $x = 0, 1.5$ and 3 . On the convex hull the most stable Li concentrations are shown with an orange circle. Red spheres indicate oxygen, orange phosphorous, white titanium, blue aluminum, and pink lithium. **c** The Formation energies of $\text{Li}_x\text{GeP}_2\text{S}_{12}$ (LGPS) with **d** the corresponding structures of $x = 4, 10$, and 22 , the green sphere indicates germanium and the yellow sulfur. The convex hull of LATP has a convex shape, indicating solid solution behavior for both Li insertion and removal; the corresponding structures for lithiation and complete delithiation appear to be stable after DFT relaxation. For LGPS, the convex is V-shaped between $x = 4$ and $x = 18$, indicating phase separation. Further proof is also seen in the corresponding structure after relaxation, where the lattice parameters and angles change, and bonds form and cleave during (de)lithiation of the structure. The convex hulls of the additional solid electrolyte materials are shown in Figure A.9 – A.15.

the electron conductivity depending on the defect formation mechanism of the solid electrolyte, located near the electrode surface where it can be redox active. As a result, a further increase in the internal resistance or promotion of redox activity of the solid electrolyte is expected. LATP has been shown to form structurally stable interfaces beyond its electrochemical window (both decomposition and intrinsic) at high potentials versus an NMC electrode.³⁵ In contrast to LATP, NASICON LAGP is predicted to have an intrinsic stability window that is wider than the decomposition window, where both on oxidation (delithiation) and reduction (lithiation) a first-order phase transformation is predicted, suggesting the indirect formation of the most stable decomposition products.

3

The convex hull of sulfide electrolyte LGPS is shown in Figure 3.2c, between $x = 4$ and $x = 18$ a V-shape is found, indicating on phase separation during oxidation ($x > 10$) and reduction ($x < 10$). In Figure 3.2d, the structures of the most stable configurations $\text{Li}_4\text{GeP}_2\text{S}_{12}$ and $\text{Li}_{18}\text{GeP}_2\text{S}_{12}$ are shown. In contrast to LATP, large changes in lattice constants and atomic bonds are observed, originating from S^{2-} that is oxidized to S^0 in $\text{Li}_4\text{GeP}_2\text{S}_{12}$ and from Ge^{4+} and P^{5+} that are reduced in $\text{Li}_{18}\text{GeP}_2\text{S}_{12}$. This is confirmed by Figure 3.2d, where it is shown that structural changes occur, during delithiation S-S bond form in the PS_4 and GeS_4 groups indicating the oxidation of S^{2-} . Upon lithiation, the P-S and Ge-S bonds break, indicating on the reduction of Ge^{4+} and P^{3+} . These changes in bonds are also reflected in the radial distribution function after relaxation (Figure A.17). After reaching the kinetic metastable phases ($\text{Li}_4\text{GeP}_2\text{S}_{12}$ and $\text{Li}_{18}\text{GeP}_2\text{S}_{12}$), the material is expected to transform into the energetically more stable decomposition products, which can also be active during further oxidation and reduction⁷. That the solid electrolyte LGPS is redox active itself and that the oxidation can be attributed to the Li-S within the LGPS structure has experimentally been shown¹¹.

The properties of the decomposition products as well as accessible intermediate metastable phases can play an important role in the rate and extend of the decomposition, depending on their electronic³⁶, ionic conductivity as well as their volumetric changes³⁷. For the decomposition products of several solid electrolyte families this has been considered elsewhere. Note that the compositions on the convex hull through which the indirect decomposition takes place may be unstable, such that decomposition readily occurs.⁷ This implies that the properties of these compositions may not be decisive for the progress of decomposition, but rather the properties of the resulting decomposition products. In case the (de)lithiated phases are stabilized, it is important to evaluate the properties of these metastable (de)lithiated phases that can form upon changing the lithium composition in the solid electrolytes. The volumetric change, band gap and ionic conductivities of such metastable compositions for the presented solid electrolytes are calculated and listed in Table A.4-A.15. Most metastable phases show a significant volume increase during lithiation and decrease during delithiation. Decrease may lead to contact loss, raising the internal resistance, whereas an increase may hinder decomposition during cycling under volume constrains, effectively widening the electrochemical stability window.²² The band gaps of the metastable phases generally decrease upon lithiation, as more electrons are inserted in the structure. Although there is no direct relationship between the bandgap and the electronic conductivity, a decreasing bandgap is an indicator for improved electronic conductivity. The composition of most solid electrolytes is optimized towards ionic conductivity, hence it drops for the

(de)lithiated phases as observed in Table A.4-A.15. Nevertheless they remain ionic conductors which in combination with increased electronic conductivity will promote the electrochemical decomposition reactions.⁶

3.5. DISCUSSION

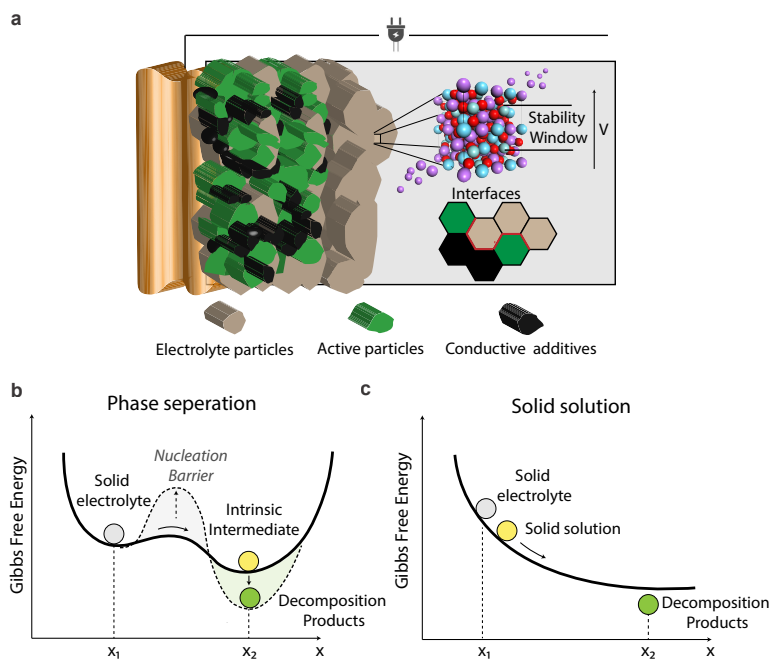


Figure 3.3: Schematic solid state battery and energy diagrams of possible reaction routes. **a** Schematic representation of a solid-state battery, the solid electrolyte is exposed to a potential at the interface with the conductive additive and active electrode particles. **b,c** Schematic energy diagrams versus Li composition in a solid electrolyte for a first-order phase and solid solution reaction. For phase separation, the solid electrolyte generally tends to react towards decomposition products in thermodynamic equilibrium. However, the stability window is determined by the nucleation barrier between the solid electrolyte and the reaction products. The intrinsic intermediate phase has a low energy barrier because the Li-ion mobility facilitates (de)lithiation, whereas the nucleation energy of the decomposition products can be large depending on the compositional and structural complexity of the material. For solid solution materials, the Li (de)insertion potential can be achieved at lower energy than the formation of decomposition products. Accordingly, the materials will react through the Li composition range until the decomposition potential is reached. A flow diagram showing the calculation routes is presented in Figure A.16.

A schematic solid-state battery is shown in Figure 3.3a. To establish good ionic transport between the electrolyte and active particles good solid-solid contact is required. In the vicinity of this contact, the electrolyte is exposed to the applied potential and will decompose according to its electrochemical stability window. Vicinity is difficult to determine, but it scales with the electronic resistance of the solid electrolyte and time that the electrolyte is exposed to the electrode potential. The decomposition centers related to

the (de)lithiation of the electrolyte are enabled by the limited electronic conductivity of the solid electrolyte in manner that closely resembles the (de)lithiation of electrodes.³⁶

For many solid electrolytes the indirect transformation via (de)lithiation (intrinsic window) predicts a stability window that is wider than that predicted based on the direct transformation into the decomposition products (decomposition window). To illustrate these transformation routes, Figure 3.3bc shows two schematic energy diagram scenarios for (de)lithiation of solid electrolytes. When this initiates a phase transition, the solid electrolyte reaction route goes through the (de)lithiated phase towards the favorable decomposition products. Solid electrolytes have high ionic conductivities and thus, small activation energies are required towards the lithiated and delithiated phases. Thereby the intrinsic metastable phase provides a low barrier accessible indirect pathway towards the decomposition products. In the case of a solid solution transition, Li-ion insertion in the structure will in general be associated with a low activation barrier as compared to the formation of the decomposition products. In this case, the end of the solid solution reaction is most likely determined by the decomposition potential. The importance of metastable phases in solid electrolytes is already revealed by the intrinsic chemical instability of most solid electrolytes towards decomposition products in thermodynamic equilibrium. The complexity of solid electrolytes varies from simple solids built up by only a few elements (binary salts) up to complex materials built by many elements (e.g. LLZO and LPSB). A larger amount of elements in a specific compound, thus representing more complex solids, in general raises the nucleation barrier towards stable decomposition products, thus enabling the formation of intermediate metastable phases.²⁸ Additionally, the type of bonds, electronic structure and chemical disorder can contribute to the chemical complexity of a material, further increasing the nucleation barrier towards decomposition. The higher nucleation barrier for these complex materials towards their decomposition products implies that direct composition is kinetically hindered. Therefore, for complex solid electrolytes, it is expected that the direct decomposition stability window is a lower limit and that redox activity will take place at potentials dictated by intrinsic (de)lithiation. Vice versa, materials with a smaller compositional space, e.g., binary Li salts, the nucleation barrier towards direct decomposition can be expected to be smaller (due to the smaller diffusion distances required) and thus the practical stability will approach the electrochemical decomposition window. Solid electrolytes are designed to have low diffusional barriers for Li-ions, facilitating the reaction pathway via intermediate metastable phases, whereas the host structure elements are intended to have a low diffusivity. For example, in the argyrodite $\text{Li}_6\text{PS}_5\text{Br}$ (LPSB) solid electrolyte, low stoichiometric amounts of Br and P make it relatively difficult to form and isolate the LiBr and P decomposition products, rationalizing why the formation energy towards the kinetic stabilization of lithiated metastable phases is more effective. For less complex Li_3YB_6 (LYB), where there are fewer elements in the unit cell, arranging and formation of decomposition products is expected to be easier, explaining why the actual electrochemical stability window can be smaller than the intrinsic stabilization potential suggest, consistent with the observed decomposition in contact with Li metal.¹⁷

That solid electrolytes do not directly form the decomposition products, and instead react through intermediate phases has been experimentally observed for various mate-

rials. Metastable intermediate phases where sulfur is connected into $P_2S_8^{4-}$ groups and disproportionation to $P_2S_7^{4-}$ and S has been observed for sulfur-based electrolytes^{7,38,39}. Similarly, for oxides, it has been shown that metastable phases exist⁴⁰. Materials with phosphate groups are known to form various P-O groups and (amorphous) metastable phases in the Li_2O - P_2O_5 range. Additionally, for oxide LLZO it has been shown that different Zr suboxides exist and are formed during charging⁸. This again rationalizes why the formation energy towards decomposition products is not representative for the actual stability window. The obvious consequence of redox activity due to (de)lithiation of solid electrolytes is generation of additional capacity (Table 3.2). Irreversible reactions towards decomposition products, directly or indirectly formed, impact the Coulombic efficiency, whereas reversible reactions of metastable intermediates and of decomposition products, provides reversible capacities.

The relatively good cycling performance for electrolytes that are unstable towards high voltage cathode materials ($> 4V$)^{25,41}, is attributed to the absence or very limited amount of conductive additive in the cathodic mixture in combination with the use of electronically isolating coatings present on the active materials. This rational strategy prevents direct contact between the solid electrolyte and the potential experienced by the electrode, slowing down or even preventing decomposition reactions.

By obtaining a more precise understanding of the realistic electrochemical stability window and corresponding structural responses, new insights can be found in designing more stable interfaces for solid-state batteries. For phase separation materials, improving bond strengths and material complexity play a crucial role in extending the decomposition window as this determines the height of the nucleation barrier towards decomposition and thus the practical electrochemical window. For solid solution materials, the wider structural stability window compared to the electrochemical window opens possibilities for solid electrolytes to have a reversible contribution to a composite electrode's capacity (generally at the expense of a lower local ion conductivity). Although none of the solid electrolytes calculated here covers the entire window of 0 – 4.5 V vs. Li/Li^+ needed to fulfil stability for a typical Li-metal high voltage cathode battery. The different classes of electrolytes inhibit electrochemical stabilities at various potentials where already proposed strategies as multilayer solid electrolyte batteries and guided formation, or artificial SEI could be applied more accurately^{3,9}. In this case however, more interfaces have to be introduced, which could lower the battery performance.

3.6. CONCLUSION

A first-principles computational framework is used to calculate the electrochemical stability of materials taking the intrinsic electrochemical window into account. This framework is applied to the most commonly used solid electrolytes in different classes of materials, showing good agreement with experimental data. For most solid electrolytes, a widening of the electrochemical decomposition stability is predicted. However, for electrolytes as LATP and LLTO, insertion reactions are predicted where the intrinsic electrochemical stability is smaller than the formation energy towards the most favourable decomposition products. Moreover, these materials can be structurally stable outside the electrochemical stability window. A better understanding of the realistic electrochemical stability window of solid electrolytes helps experimentalists analyse and design new

types of solid-state batteries. Stable interfaces and fundamental knowledge about the reactions involved remains of key importance in improving the rate capability and capacity retention in solid-state batteries.

REFERENCES

- [1] J. Janek and W. G. Zeier, *A solid future for battery development*, [Nature Energy](#) **1**, 14 (2016).
- [2] F. Zheng, M. Kotobuki, S. Song, M. O. Lai, and L. Lu, *Review on solid electrolytes for all-solid-state lithium-ion batteries*, [Journal of Power Sources](#) **389**, 198 (2018).
- [3] Y. Xiao, Y. Wang, S.-H. Bo, J. C. Kim, L. J. Miara, and G. Ceder, *Understanding interface stability in solid-state batteries*, [Nature Reviews Materials](#) (2019).
- [4] Z. Zhang, Y. Shao, B. Lotsch, Y.-S. Hu, H. Li, J. Janek, L. F. Nazar, C.-W. Nan, J. Maier, M. Armand, *et al.*, *New horizons for inorganic solid state ion conductors*, [Energy & Environmental Science](#) **11**, 1945–1976 (2018).
- [5] C. Yu, S. Ganapathy, E. R. H. v. Eck, H. Wang, S. Basak, Z. Li, and M. Wagemaker, *Accessing the bottleneck in all-solid state batteries, lithium-ion transport over the solid-electrolyte-electrode interface*, [Nature Communications](#) **8** (2017).
- [6] T. Famprikis, P. Canepa, J. A. Dawson, M. S. Islam, and C. Masquelier, *Fundamentals of inorganic solid-state electrolytes for batteries*, [Nature Materials](#) **18**, 1278–1291 (2019).
- [7] T. K. Schwietert, V. A. Arszewlewska, C. Wang, C. Yu, A. Vasileiadis, N. J. J. de Klerk, J. Hageman, T. Hupfer, I. Kerkamm, Y. Xu, E. van der Maas, E. M. Kelder, S. Ganapathy, and M. Wagemaker, *Clarifying the relationship between redox activity and electrochemical stability in solid electrolytes*, [Nature Materials](#) **19**, 428 (2020).
- [8] F. Han, Y. Zhu, X. He, Y. Mo, and C. Wang, *Electrochemical stability of $\text{Li}_{10}\text{GeP}_2\text{S}_{12}$ and $\text{Li}_7\text{La}_3\text{Zr}_2\text{O}_{12}$ solid electrolytes*, [Advanced Energy Materials](#) **6**, 1501590 (2016).
- [9] Y. Zhu, X. He, and Y. Mo, *Origin of outstanding stability in the lithium solid electrolyte materials: Insights from thermodynamic analyses based on first-principles calculations*, [ACS Applied Materials & Interfaces](#) **7**, 23685 (2015).
- [10] W. D. Richards, L. J. Miara, Y. Wang, J. C. Kim, and G. Ceder, *Interface stability in solid-state batteries*, [Chemistry of Materials](#) **28**, 266 (2016).
- [11] F. Han, T. Gao, Y. Zhu, K. J. Gaskell, and C. Wang, *A battery made from a single material*, [Advanced Materials](#) **27**, 3473 (2015).
- [12] Y. Tian, T. Shi, W. D. Richards, J. Li, J. C. Kim, S.-H. Bo, and G. Ceder, *Compatibility issues between electrodes and electrolytes in solid-state batteries*, [Energy & Environmental Science](#) **10**, 1150 (2017).
- [13] J. P. Perdew, K. Burke, and Y. Wang, *Generalized gradient approximation for the exchange-correlation hole of a many-electron system*, [Physical Review B](#) **54**, 16533 (1996).
- [14] G. Kresse and J. Hafner, *Ab initio molecular dynamics for liquid metals*, [Physical Review B](#) **47**, 558 (1993).

- [15] M. Aydinol, A. Kohan, and G. Ceder, *Ab initio calculation of the intercalation voltage of lithium-transition-metal oxide electrodes for rechargeable batteries*, *Journal of Power Sources* **68**, 664 (1997).
- [16] A. Jain, S. P. Ong, G. Hautier, W. Chen, W. D. Richards, S. Dacek, S. Cholia, D. Gunter, D. Skinner, G. Ceder, and K. A. Persson, *Commentary: The materials project: A materials genome approach to accelerating materials innovation*, *APL Materials* **1**, 011002 (2013).
- [17] T. Asano, A. Sakai, S. Ouchi, M. Sakaida, A. Miyazaki, and S. Hasegawa, *Solid halide electrolytes with high lithium-ion conductivity for application in 4 V class bulk-type all-solid-state batteries*, *Advanced Materials* **30**, 1803075 (2018).
- [18] K. Takahashi, K. Hattori, T. Yamazaki, K. Takada, M. Matsuo, S. Orimo, H. Maekawa, and H. Takamura, *All-solid-state lithium battery with LiBH_4 solid electrolyte*, *Journal of Power Sources* **226**, 61 (2013).
- [19] T. Teranishi, Y. Ishii, H. Hayashi, and A. Kishimoto, *Lithium ion conductivity of oriented $\text{Li}_{0.33}\text{La}_{0.56}\text{TiO}_3$ solid electrolyte films prepared by a sol-gel process*, *Solid State Ionics* **284**, 1 (2016).
- [20] T. Hakari, M. Nagao, A. Hayashi, and M. Tatsumisago, *All-solid-state lithium batteries with Li_3PS_4 glass as active material*, *Journal of Power Sources* **293**, 721 (2015).
- [21] W. Zhang, D. Schröder, T. Arlt, I. Manke, R. Koerver, R. Pinedo, D. A. Weber, J. Sann, W. G. Zeier, and J. Janek, *(Electro)chemical expansion during cycling: monitoring the pressure changes in operating solid-state lithium batteries*, *Journal of Materials Chemistry A* **5**, 9929 (2017).
- [22] W. Fitzhugh, F. Wu, L. Ye, H. Su, and X. Li, *Strain-stabilized ceramic-sulfide electrolytes*, *Small* **15**, 1901470 (2019).
- [23] C.-M. Park and H.-J. Sohn, *Black phosphorus and its composite for lithium rechargeable batteries*, *Advanced Materials* **19**, 2465 (2007).
- [24] S. Boulineau, J.-M. Tarascon, J.-B. Leriche, and V. Viallet, *Electrochemical properties of all-solid-state lithium secondary batteries using Li-argyrodite $\text{Li}_6\text{PS}_5\text{Cl}$ as solid electrolyte*, *Solid State Ionics* **242**, 45 (2013).
- [25] N. Kamaya, K. Homma, Y. Yamakawa, M. Hirayama, R. Kanno, M. Yonemura, T. Kamiyama, Y. Kato, S. Hama, K. Kawamoto, and A. Mitsui, *A lithium superionic conductor*, *Nature Materials* **10**, 682 (2011).
- [26] V. Lacivita, Y. Wang, S.-H. Bo, and G. Ceder, *Ab initio investigation of the stability of electrolyte/electrode interfaces in all-solid-state Na batteries*, *Journal of Materials Chemistry A* **7**, 8144 (2019).
- [27] B. Put, P. Vereecken, and A. Stesmans, *On the chemistry and electrochemistry of LiPON breakdown*, *Journal of Materials Chemistry A* **6**, 4848 (2018).

- [28] X. Yu, J. B. Bates, G. E. Jellison, and F. X. Hart, *A stable thin-film lithium electrolyte: Lithium phosphorus oxynitride*, *Journal of The Electrochemical Society* **144**, 524.
- [29] S. Wang, Q. Bai, A. M. Nolan, Y. Liu, S. Gong, Q. Sun, and Y. Mo, *Lithium chlorides and bromides as promising solid-state chemistries for fast ion conductors with good electrochemical stability*, *Angewandte Chemie International Edition* **58**, 8039.
- [30] A. Schwöbel, R. Hausbrand, and W. Jaegermann, *Interface reactions between LiPON and lithium studied by in-situ x-ray photoemission*, *Solid State Ionics* **273**, 51.
- [31] R. Jalem, Y. Morishita, T. Okajima, H. Takeda, Y. Kondo, M. Nakayama, and T. Kasuga, *Experimental and first-principles DFT study on the electrochemical reactivity of garnet-type solid electrolytes with carbon*, *Journal of Materials Chemistry A* **4**, 14371 (2016).
- [32] O. Bohnke, C. Bohnke, and J. Fourquet, *Mechanism of ionic conduction and electrochemical intercalation of lithium into the perovskite lanthanum lithium titanate*, *Solid State Ionics* **91**, 21 (1996).
- [33] K. Arbi, A. Kuhn, J. Sanz, and F. García-Alvarado, *Characterization of lithium insertion into NASICON-type $Li_{1+x}Ti_{2-x}Al_x(PO_4)_3$ and its electrochemical behavior*, *Journal of The Electrochemical Society* **157**, A654 (2010).
- [34] K. Arbi, M. Hoelzel, A. Kuhn, F. García-Alvarado, and J. Sanz, *Local structure and lithium mobility in intercalated $Li_3Al_xTi_{2-1}(PO_4)_3$ NASICON type materials: a combined neutron diffraction and NMR study*, *Phys. Chem. Chem. Phys.* **16**, 18397 (2014).
- [35] J.-Y. Liang, X.-X. Zeng, X.-D. Zhang, P.-F. Wang, J.-Y. Ma, Y.-X. Yin, X.-W. Wu, Y.-G. Guo, and L.-J. Wan, *Mitigating interfacial potential drop of cathode–solid electrolyte via ionic conductor layer to enhance interface dynamics for solid batteries*, *Journal of the American Chemical Society* **140**, 6767 (2018).
- [36] F. Han, A. S. Westover, J. Yue, X. Fan, F. Wang, M. Chi, D. N. Leonard, N. J. Dudney, H. Wang, and C. Wang, *High electronic conductivity as the origin of lithium dendrite formation within solid electrolytes*, *Nature Energy* **4**, 187 (2019).
- [37] R. Koerver, W. Zhang, L. de Biasi, S. Schweidler, A. O. Kondrakov, S. Kolling, T. Brezesinski, P. Hartmann, W. G. Zeier, and J. Janek, *Chemo-mechanical expansion of lithium electrode materials – on the route to mechanically optimized all-solid-state batteries*, *Energy & Environmental Science* **11**, 2142 (2018).
- [38] R. Koerver, F. Walther, I. Aygün, J. Sann, C. Dietrich, W. G. Zeier, and J. Janek, *Redox-active cathode interphases in solid-state batteries*, *Journal of Materials Chemistry A* **5**, 22750 (2017).
- [39] T. Hakari, M. Deguchi, K. Mitsuhara, T. Ohta, K. Saito, Y. Orikasa, Y. Uchimoto, Y. Kowada, A. Hayashi, and M. Tatsumisago, *Structural and electronic-state changes of a sulfide solid electrolyte during the li deinsertion–insertion processes*, *Chemistry of Materials* **29**, 4768 (2017).

- [40] W. Sun, S. T. Dacek, S. P. Ong, G. Hautier, A. Jain, W. D. Richards, A. C. Gamst, K. A. Persson, and G. Ceder, *The thermodynamic scale of inorganic crystalline metastability*, [Science Advances](#) **2**, e1600225 (2016).
- [41] Y. Kato, S. Hori, T. Saito, K. Suzuki, M. Hirayama, A. Mitsui, M. Yonemura, H. Iba, and R. Kanno, *High-power all-solid-state batteries using sulfide superionic conductors*, [Nature Energy](#) **1**, 16030 (2016).

4

THE EFFECT OF ALIOVALENT CATION SUBSTITUTION ON THE LI-ION DIFFUSION MECHANISM IN LI-ARGYRODITES.

This chapter has been submitted as: **Schwietert, T. K.** Vasileiadis, A., Gautam, A., Drost, D. and Wagemaker, M., *The effect of aliovalent cation substitution on the Li-ion diffusion mechanism in Li-argyrodites.*

4.1. ABSTRACT

LITHIUM-ION conducting argyrodites have shown great promise as solid electrolytes for solid-state batteries due to their relatively high ionic conductivity. Recent studies suggest that aliovalent substitutions can be an effective approach to further improve transport properties in this class of materials. For $\text{Li}_6\text{PS}_5\text{Br}$, it has been experimentally shown that Si doping in the Li-argyrodite structure provides a threefold increase in the ionic conductivity. To investigate the origin of this increasing Li diffusion, a density functional theory study is performed, where Si^{4+} in the $\text{Li}_6\text{PS}_5\text{Br}$ structure substitutes different ratios of P^{5+} atoms. Arrhenius plots show the increasing trend in the ionic conductivity for the Si-doped argyrodites, where the higher conductivity can be correlated to partial occupancy of Li on the T4 sites. This occupancy is activated by the Si^{4+} dopant, which provides excess Li occupancy in the argyrodite phase due to its lower valance. The presence of Li on the T4 site redistributes Li-ions in the lattice due to coulombic interactions, resulting in a more uniform Li distribution around the T4 and the neighboring T5 sites, effectively increasing the mobility through this site. Since the T4 site is positioned in the intercage jump pathway, an increase in the intercage jump rate is found, which is directly related to the macroscopic diffusion and bulk conductivity. Additionally, Rietveld refinements of a neutron diffraction experiment on the Si-doped argyrodite confirm the partial Li occupancy on the T4 sites. Understanding the effect of partially occupied interstitials generated by aliovalent doping is essential to improve the ionic conductivity of solid electrolytes, ultimately enabling better performing solid-state batteries.

4

4.2. INTRODUCTION

The development of all-solid-state batteries promises to provide safer batteries, by replacing the volatile liquid electrolyte, as well as higher energy densities, by increasing the fraction of cathode active materials and the possibility of using Li metal as an anode.^{1,2} One of the main obstacles towards solid-state batteries is the restricted power density originating from the poor Li-ion diffusion in bulk and at the interface with the electrode. Several solid electrolytes have been developed so far, including oxides, halides, borohydrides, and sulfides. Among all of them, sulfide based solid electrolytes shows great promise due to exceptionally high ionic conductivities and low grain boundary resistances.¹⁻³ Recently, Li-argyrodites $\text{Li}_6\text{PS}_5\text{X}$ (X = Cl, Br, and I) have shown great interest due to their higher ionic conductivity (1 - 10 mS/cm at room temperature).^{4,5} Furthermore, Li-argyrodites are suitable solid electrolytes because they possess relatively low grain boundary resistance due to its mechanically soft nature. However, the electrochemical instability at low and high potentials, especially in the vicinity of the negative and positive electrodes remains a major challenge.^{3,6-8}

To further increase the ionic conductivity of Li-argyrodites several methods are successfully implemented. The ratio of halogen anions ($\text{Li}_{6-x}\text{PS}_{5-x}(\text{Cl,Br,I})_{1+x}$) can be altered to increase the number of vacancies^{9,10}, and exchange between S^{2-}/X^- (X = Cl, Br and I) anions on Wyckoff 4c site referred to a 'site-disorder', can be tailored to make Li pathways more interconnected.¹¹ Another practical approach to increase the ionic conductivity of Li-argyrodites is doping the structure with aliovalent cations such as Si^{4+} ($r_{\text{Si}^{4+}} = 26$ pm), Ge^{4+} ($r_{\text{Ge}^{4+}} = 39$ pm), Sn^{4+} ($r_{\text{Sn}^{4+}} = 55$ pm) or Al^{3+} ($r_{\text{Al}^{3+}} = 39$ pm).¹²⁻¹⁴ These dopants can

increase the Li-ion concentration as well as the polyhedral volume due to their higher ionic radius of aliovalent cations compared to P^{5+} ($r_{P^{5+}} = 17$ pm). Doping can also be effectively used to alter other relevant electrolyte properties such as electrochemical stability¹⁵, air stability¹⁶, elasticity¹⁷, hardness¹⁷, and fracture toughness¹⁷. Kraft et al. recently demonstrated the Ge doping in Li-argyrodites enables the highest conductivities of 18.4 mS/cm after sintering for $Li_{6.6}P_{0.4}Ge_{0.6}S_5I$.¹² Furthermore, Zhou et al. showed that Si and Ge doping in thioantimonate argyrodites $Li_{6+x}Sb_{1-x}MxS_5I$ ($M = Si$ and Ge) increased the ionic conductivities up to 24 mS/cm after sintering for $Li_{6.6}Si_{0.6}Sb_{0.4}S_5I$.¹⁸ Also, Si^{4+} as a dopant in sulfur electrolytes has shown to be highly effective, a Li-P-Si-S-Cl electrolyte in the LISICON structure has delivered one of the highest conductivities reported for solid electrolytes in general (25 mS/cm).¹⁹

Silicon doping in the Li-argyrodite Li_6PS_5Br structure also shows significant improvements in the ionic conductivity. Recently Minafra et al. have shown that Si^{4+} doping in these argyrodites increases the Li-ion conductivity by a factor of three.¹³ As this increase in conductivity is higher than expected by only considering the increase in charge carrier concentration (6 % for $Li_{6.5}P_{0.5}Si_{0.5}S_5Br$), a more detailed diffusion mechanism is required to understand this increment. In the argyrodite system, Li-ions migrate through the crystal lattice by hopping from occupied to vacant sites. It has been assumed that the Wyckoff $48h$ (T5) site is the single active Li site in the diffusion mechanism.⁹ Recently, multiple additional sites have been proposed to contribute to the diffusion mechanism; however, a complete mechanism is not yet presented. One of these new positions is the Wyckoff $16e$ (T4) site, wherein a similar structure to Li-argyrodite, $Li_{6.6}Al_{0.15}Si_{1.35}S_{5.4}O_{0.6}$, it has been theorized that the T4 interstitial can be occupied and stimulate the diffusion process by flattening the energy landscape.²⁰

Here, we aim to understand the effect of aliovalent Si^{4+} doping on the transport properties of argyrodite Li_6PS_5Br . An ab-initio molecular dynamics study performed on the $Li_{6+x}P_{1-x}Si_xS_5Br$ structure shows the stabilization of the T4 site, which is enabled by the excess Li inserted in the structure. Using the ab initio molecular dynamics simulations increased conductivity is found for higher doping concentrations, this can be correlated to the partial occupancy on the T4 site, that facilitates an energetically more facile route for intercalation diffusion. Additionally, the occupancy on the T4 site is confirmed by a neutron diffraction experiment, where partial occupancy on the $16e$ site is shown by Rietveld refinement. Overall, this study provides an enhanced fundamental understanding of structure-transport correlations in Li-argyrodites by cation substitution.

4.3. METHOD

To evaluate the Li-ion diffusion in argyrodites ab initio molecular dynamics (AIMD) simulations using Vienna Ab-Initio Simulation Package (VASP) are performed. The simulations use the generalized gradient approximation (GGA) and the PAW-PBE basis set, the cutoff energy is set at 350 eV. First, the structure is relaxed using a $4 \times 4 \times 4$ k-points mesh which is reduced to $1 \times 1 \times 1$ in the AIMD simulations.⁹ The AIMD simulations were performed with 400,000 time steps of 2 femtoseconds, resulting in a total simulation time of 800 picoseconds. The AIMD simulation is then separated into 10 parts for which the mean diffusion constant and standard errors are calculated.²¹

The argyrodite structure is taken from literature⁹, the Si^{4+} atoms are substituted on

the P^{5+} sites according to literature.¹³ Li-ions are added on the T5 sites furthest away from neighboring Li-ions to minimize coulombic interactions.⁹ To determine the Li-ion conductivity in Li-argyrodites, first the tracer diffusivity D is calculated by Equation 4.1,

$$D = \frac{1}{2dN} \sum_{i=1}^N \frac{|r(t) - r(t_0)|^2}{dt} \quad (4.1)$$

where N is the total number of diffusing atoms, $r(t)$ the displacements of single Li atoms, d the number of diffusion dimensions, and t the simulation time. From the diffusion constant, the conductivity can be calculated using the Nernst-Einstein relation:

$$\sigma = \frac{ne^2 z^2}{k_B T} D \quad (4.2)$$

where e is the electron charge, n the particle density, z is the charge of the diffusive element, and k_B the Boltzmann constant.

To evaluate jumps rates in the MD simulation, jumps between specific sites in the structure are monitored. To define a jump in the simulation, a radius around the site position is specified, if a Li atom jumps from within the site radius to another site radius, a jump is counted. In the evaluation of the intercage jump rates, 'back and forth' jumps where the Li moves to a neighboring position and jumps back are not counted.

4.4. RESULTS

Argyrodite crystallizes in the $F\bar{4}3m$ spacegroup, the structure is shown in Figure 4.1. In the argyrodite structure, Li-ions jump between unoccupied sites through the lattice. In previous reports it was assumed that Li only resided on the T5 site. For this site, three different jumps are distinguished: doublet, intracage, and intercage.⁹ Doublet jumps take place between paired T5 sites (distance 1.9 Å), intracage jumps take place between pairs of T5 sites (distance 2.25 Å). In a unit cell, the six pairs of T5 sites surround the 4c sites, which together will be defined as cages.⁹ The intercage jumps is important for ionic transport, as represent the shortest jumps distance between the cages.

As Li moves fast in the argyrodite structure, partial occupancies on intermediate and meta-stable sites are difficult to assign as the probability density of Li spreads out over multiple sites. In recent literature, high-resolution neutron and X-ray diffraction experiments have shown partial occupancies on two additional Li sites between the T5 positions: T2 site^{11,22,23} and the T5a site (Wyckoff 24g).^{11,13,24} In the simulations performed here, no clear indication of Li occupation on the T5a site is found (< 0.05 occupancy). Additionally, there are several vacant Li sites in the symmetry that can be occupied.²³ Where especially the T4 site (Wyckoff 16e), an interstitial site that is located between two cages is interesting as it has been theorized that if this site would be occupied diffusion through this site could improve the macroscopic diffusion as it lowers the energy barrier for intercage jumps.^{20,22,25}

Lithium migration between the Li cages, or intercage jumps, are predominantly the limiting factor for Li-ion diffusion in the argyrodite.⁹ Two intercage jump pathways are described in literature, one pathway via two neighboring T2 sites and a pathway between two T5 sites via the T4 site,²¹ the two paths are shown in Figures 4.1c and 1d. The jump

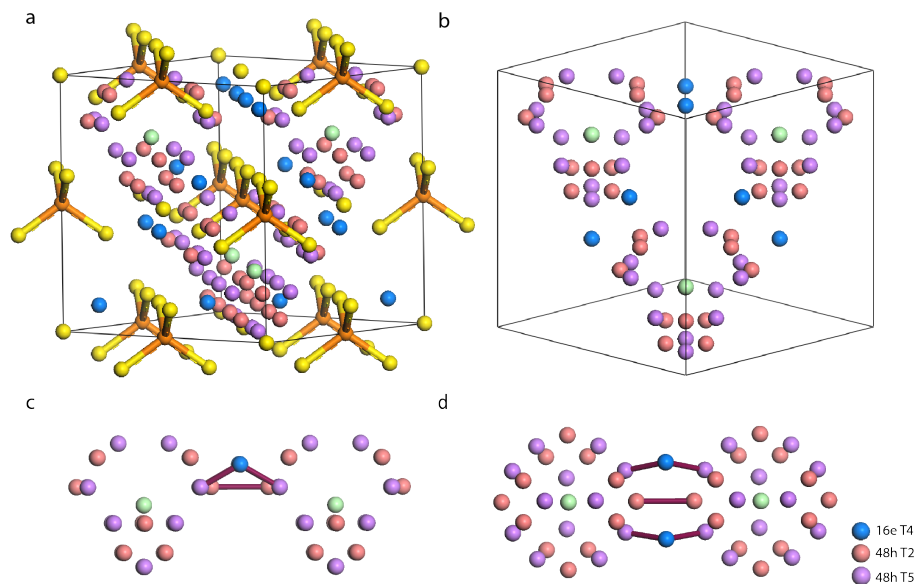


Figure 4.1: Structure, Li distribution and possible intercage hopping routes of $\text{Li}_6\text{PS}_5\text{Br}$. **a** The cubic structure of $\text{Li}_6\text{PS}_5\text{Br}$ with the T5 lithium sites (Wyckoff 48*h*) in purple, T2 lithium sites (Wyckoff 48*h*) in red, the T4 lithium sites (Wyckoff 16*e*) in blue, the $\text{Si}^{4+}/\text{P}^{5+}$ sites in orange, the Wyckoff 4a $\text{Br}^-/\text{S}^{2-}$ sites in yellow, Wyckoff 4c $\text{Br}^-/\text{S}^{2-}$ sites in green. **b** Lithium form cages like substructure around the Wyckoff 4c site, the T4 sites between the Li cages link the cages. **c** side view and **d** top view of two Li diffusion ‘cages’, of two intercage diffusion paths which determine the macroscopic diffusion, the Li jump pathway via T2 – T2 sites and the T5 – T4 – T5 pathway.

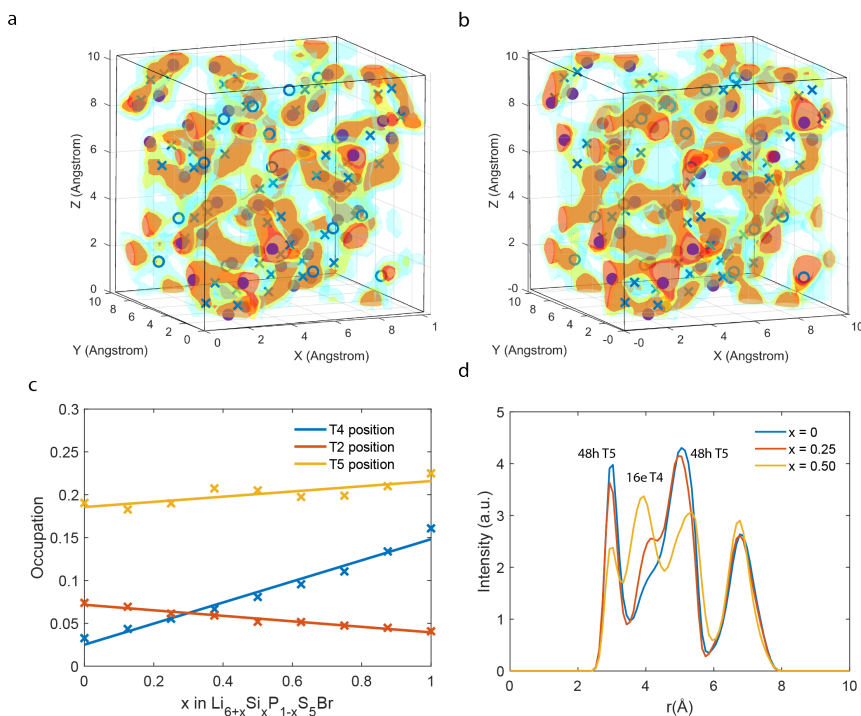


Figure 4.2: Li density, site occupancy and radial distribution function of Si-doped $\text{Li}_6\text{PS}_5\text{Br}$. **a** Density plot of Li for the undoped $\text{Li}_6\text{PS}_5\text{Br}$ and **b** the fully doped $\text{Li}_7\text{SiS}_5\text{Br}$ during a 100 ps 550 K AIMD simulation. The solid spheres are the T5 positions, crosses the T2 positions, and the circles T4 positions. Red indicates a high lithium density and more blue at a lower lithium density. With increased doping, the intensity on the T4 position increases. **c** Occupation of Li on the T4 position, T2, and T5 in a 550K AIMD simulation. **d** Radial distribution plot of Li and $\text{Si}^{4+}/\text{P}^{5+}$ during T5 - T5 jumps, the peaks at 3\AA and 5\AA correspond to the T5 position and with increased doping, a peak at 4\AA is found which corresponding to the T4 position.

pathway between the T2 sites is theorized because the T2 positions of two neighboring cages are in close proximity (2.1\AA).²³ The second jump pathway through the T4 site is considered as it connects two T5 sites of coinciding cages and forms two intercage pathways around the T2 site.^{9,11}

To evaluate the effect of the Si substitution in Li-argyrodite by DFT, the doping concentration x in $\text{Li}_{6+x}\text{P}_{1-x}\text{Si}_x\text{S}_5\text{Br}$ is increased from $x = 0$ to $x = 1$ in eight concentration steps. As experimental research predicts that Si^{4+} cation replaces P^{5+} cation on the Wyck-off $4b$ positions¹³, Si^{4+} is correspondingly homogeneously substituted on the P positions in the DFT simulations. The relaxed structures show a linear relationship between lattice parameters and doping concentration due to higher ionic radius of Si^{4+} ($r_{\text{Si}^{4+}} = 26 \text{ pm}$) compared to P^{5+} ($r_{\text{P}^{5+}} = 17 \text{ pm}$), and is in well agreement with literature (Figure A.19).¹³ To visualize Li migration, the undoped and fully doped argyrodite Li densities are shown in Figures 4.2a and 4.2b. Lithium density plots from the undoped $\text{Li}_6\text{PS}_5\text{Br}$ show high lithium densities on the T5 sites, where the cage-like structures in which lithium diffuses are clearly visible. In both the doped and undoped structures the relatively high lithium

concentrations between the T5 sites can be assigned to the T2 position. Additionally, for the doped structure, a sharp increase in Li density between the Li cages is found, analyzing these positions in the $F\bar{4}3m$ spacegroup indicates the occupation of the T4 position. The T4 position is enabled by the lower valence of Si^{4+} which provides a Li excess in the doped argyrodite structure, because of charge balance. These additional Li^+ -ions in the structure occupy the lowest energy vacant site can also be influenced by the difference in valence between Si^{4+} and P^{5+} , which have a reduced repelling coulombic force on Li^+ ions changing the local energy landscape around the Si atoms.

The occupancies of the T4, T2 and T5 positions are shown in Figure 4.2c. The site occupancies are determined from the time fraction that Li resides on a specific site in the AIMD simulation. Figure 4.2c clearly shows an increase in the T4 occupancy as the Si^{4+} content is increased and agrees with the higher Li densities found on this site in Figure 4.2a,b. The T5 site occupancy shows a slight increase (0.19 – 0.22) governed with a similar decrease in the T2 site occupancy (0.07-0.04). Hence, the total T5 and T2 site occupancy remains equal, and the excess Li introduced by Si doping occupies the T4 position.

To investigate the specific Li-ion motion during the intercage T5 - T5 jumps via the T4 position, the radial distribution function (RDF) of Li and the $4b$ site ($\text{P}^{5+} / \text{Si}^{4+}$ position) during T5 – T5 jumps is shown in Figure 4.2d. The RDF shows the integrated Li density over time as a function of the distance to the nearest $4b$ site. For the undoped argyrodite, two peaks are visible around 3 Å and 5 Å corresponding to two T5 positions. Si doping results in a peak around 4.0 Å, coinciding with the distance from the Si^{4+} or P^{5+} positions to the T4 positions. Hence, the RDF shows that the diffusing ions jump through the T4 positions, when Si^{4+} is increasingly substituted into the unit cell. In the RDF a flattening of the Li density for the diffusion pathway is shown as the Li density is more spread out and the peaks corresponding to the T5 sites are lower. The flattening of the Li density shows that Li is less constrained to the specific site positions, which indicates on the flattening of the energy landscape hence a more facile jump pathway.²⁵ The flattening is caused by the partial Li occupation on the T4 positions that, due to coulombic interactions in the lattice, distributes Li more uniformly around the T4 and two adjoining T5 sites. This is confirmed by the RDF where the Li density on the T5 sites declines and is spread out more evenly around the T4 site for higher dopant concentrations.

To analyse the site occupancies in the Si-doped argyrodite structures experimentally, neutron diffraction is performed on $\text{Li}_{6.125}\text{P}_{0.875}\text{Si}_{0.125}\text{S}_5\text{Br}$. The site occupancies are obtained by Rietveld refinement and are shown in Figure 4.3a, the fitted parameters of the Rietveld refinement are shown in Table A.16. Indeed a fractional occupancy of 7 % is found on the T4 position. This is consistent with the occupancies as predicted by the MD simulations for this doping concentration in Figure 4.1c, and shows that the T4 position is partially occupied in the doped structures. Similar to the MD simulations, the combined T2 and T5 occupancy remain equal, indicating that the T4 position accounts for the excess Li. The relative ratios of the T2 and T5 sites are different compared to the MD simulations where a relatively low occupation of T2 occupancy (2.5 %) is found. This discrepancy can be explained by the proximity of the T2 site to the T5 site that are difficult to entangle in the MD simulations as the radii that determine this sites are relatively close. Li moving from the T2 site to the T5 site overestimates the occupancy on the

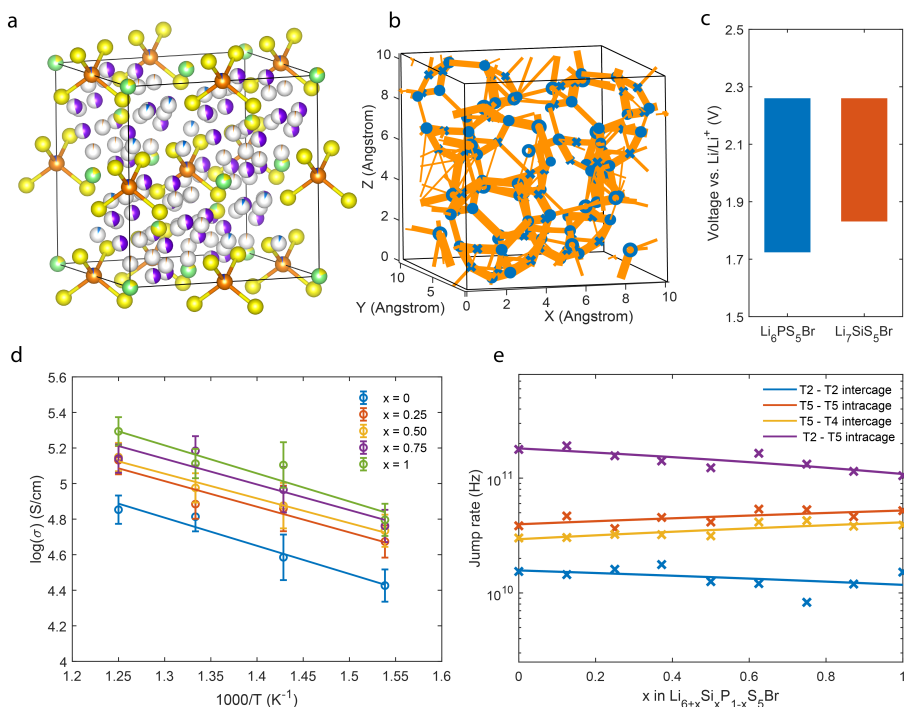


Figure 4.3: Refined site occupancy, electrochemical stability, Li-ion conductivity and hopping frequencies in Si-doped $\text{Li}_6\text{PS}_5\text{Br}$. **a** Structure of $\text{Li}_{6.125}\text{P}_{0.875}\text{Si}_{0.125}\text{S}_5\text{Br}$ with fractional occupancies based on neutron diffraction experiment. Yellow color represent the sulfur, green as bromide, and orange as phosphorous. The T5 is depicted in purple, the T2 in red and T4 in blue **b** Jump statistics plot of $\text{Li}_{6.5}\text{P}_{0.5}\text{Si}_{0.5}\text{S}_5\text{Br}$, thicker lines correspond to a higher jump rate between positions. **c** Electrochemical stability window of $\text{Li}_6\text{PS}_5\text{Br}$ and $\text{Li}_7\text{SiS}_5\text{Br}$. **d** Conductivity versus temperature plot of $\text{Li}_{6+x}\text{P}_{1-x}\text{Si}_x\text{S}_5\text{Br}$ for different x . **e** Jump rate of different site jumps for $\text{Li}_{6+x}\text{P}_{1-x}\text{Si}_x\text{S}_5\text{Br}$.

T2 site, however, in agreement with the MD simulations, the total occupancy on these positions remains unchanged.

Figure 4.3c shows the electrochemical stability towards the most favorable decomposition products of the fully doped $\text{Li}_7\text{Si}_5\text{Br}$ and undoped $\text{Li}_6\text{PS}_5\text{Br}$. The oxidation potential is equal for both phases as it is determined by the sulfur ($\text{S}^{2-} / \text{S}^0$) redox. The reduction potential that is affected by the phosphor ($\text{P}^{5+} / \text{P}^0$) and Si redox ($\text{Si}^{4+} / \text{Si}^0$), shows a higher reduction potential for increasing dopant concentrations. The lower reduction potential of Si compared to P can rationalize this, making the decomposition reaction towards reduced Si phases energetically more favourable over reduced P based decomposition products, resulting in a narrowing of the electrochemical stability for Si doped argyrodites.

To determine the conductivity of Li-ions in the Si-doped argyrodites, Arrhenius plots of the conductivity and temperature are shown in Figure 4.3d. An increasing trend in the conductivity with higher doping concentrations is shown, comparable to the direct experimental impedance spectroscopy results.¹³ The tracer conductivity at room temperature is 14 mS/cm for the undoped argyrodite $\text{Li}_6\text{PS}_5\text{Br}$ and 21 mS/cm for $\text{Li}_{6.5}\text{P}_{0.5}\text{Si}_{0.5}\text{S}_5\text{Br}$. This is a similar increasing trend as found in experiments in literature where the tracer conductivity is increased from 0.7 mS/cm to 2.4 mS/cm from the undoped argyrodite to $\text{Li}_{6.5}\text{P}_{0.5}\text{Si}_{0.5}\text{S}_5\text{Br}$.¹³ The tracer conductivities determined from AIMD simulations are around a factor 2 larger as found in literature, most probable originating from AIMD simulations that generally overestimate the ionic conductivity because a perfect crystal is assumed in the simulations without, for example, grain boundary resistance and contact losses.⁹ The activation energies found in impedance spectroscopy experiments (~ 0.2 eV¹³) are in good agreement with the activation energy found in the AIMD simulations shown in Figure A.20.

To investigate the influence of the jump type on the increase in Li conductivity, the jump rates between different Li sites in the $\text{Li}_{6+x}\text{P}_{1-x}\text{Si}_x\text{S}_5\text{Br}$ structure are calculated and shown in Figure 4.3e. The T2 – T5 jump path, corresponding to the jumps inside the cages, shows the highest jump rates which coincide with the large delocalization of the Li density in Figure 4.2a between the T2 and T5 sites, indicating fast Li movement between the two positions.

To evaluate the jump statistics between the Li cages, or ‘intercage’ jumps, the T5 – T4 – T5 jumps and T2 – T2 jumps are considered as shown in Figure 4.1d. The jump frequency of the T5 – T4 – T5 path is significantly higher than the T2 – T2 jump path and thus has a larger contribution to the macroscopic diffusion. This shows that the intercage diffusion predominantly moves through the T4 position as compared to the T2 – T2 jump pathway. Additionally, an increase in the T4 – T5 jump rate as a function of doping concentration is shown in Figure 4.3e. This is consistent with Figure 4.2d where it is shown that the Li density for the jump pathway is flattened at higher doping concentrations, indicating faster diffusion. Because the intercage jump rate is the bottleneck for macroscopic diffusion, the faster jump rate through the T4 site directly influences the total macroscopic diffusivity and ionic conductivity of the solid electrolyte as shown in Figure 4.3d.

Finally, a correlated increase in jump rate per doping concentration between the T5 – T4 and T5 – T5 jump rates is shown in Figure 4.3e, these jumps correspond to the inter-

cage and intra-cage jumps, respectively. The correlation suggests that a jump from the T4 to a T5 site promotes a jump between two neighboring T5 sites. The above indicates on a correlated interstitially driven mechanism, where Li on the T4 interstitial site pushes a Li on the T5 position to a neighboring T5 position. This is beneficial for macroscopic diffusion as it improves both the inter- and intracage diffusion. A decrease in the T5 – T2 jump rate compromises this correlated increase however does not affect the macroscopic diffusion as this jump rate is not a limiting factor for the macroscopic diffusion.

4.5. CONCLUSION

Using DFT-based molecular dynamics the origin of higher conductivities in Si-doped $\text{Li}_6\text{PS}_5\text{Br}$ is investigated. The simulations show that the excess Li in the Si^{4+} doped structures, originating from charge balance, resides on the T4 (Wyckoff 16e) sites. Radial distribution function analysis shows that this partial Li occupancy on the T4 position distributes Li more uniformly between the T5 and T4 position, effectively flattening the energy landscape and increasing the Li mobility through the T4 site. This increase in Li-ion mobility is confirmed by increasing jump rate statistics for this jump path. Because the T4 sites resides between two bordering Li cages, the intercage diffusion increases as a function of the doping concentration. As the intecage diffusivity is directly related to the macroscopic diffusion and ionic conductivity, a corresponding increase in Li-ion conductivity is shown in Arrhenius plots for higher doping concentrations. However, the increase in ionic conductivity is compromised by a higher reduction potential for higher doping concentrations, reducing the electrochemical stability for increased Si doping.

REFERENCES

- [1] T. Famprikis, P. Canepa, J. A. Dawson, M. S. Islam, and C. Masquelier, *Fundamentals of inorganic solid-state electrolytes for batteries*, *Nature Materials* **18**, 1278–1291 (2019).
- [2] F. Zheng, M. Kotobuki, S. Song, M. O. Lai, and L. Lu, *Review on solid electrolytes for all-solid-state lithium-ion batteries*, *Journal of Power Sources* **389**, 198 (2018).
- [3] Y. Xiao, Y. Wang, S.-H. Bo, J. C. Kim, L. J. Miara, and G. Ceder, *Understanding interface stability in solid-state batteries*, *Nature Reviews Materials* (2019).
- [4] S. Boulineau, M. Courty, J.-M. Tarascon, and V. Viallet, *Mechanochemical synthesis of Li-argyrodite $\text{Li}_6\text{PS}_5\text{X}$ ($\text{X} = \text{Cl}, \text{Br}, \text{I}$) as sulfur-based solid electrolytes for all solid state batteries application*, *Solid State Ionics* **221**, 1 (2012).
- [5] R. P. Rao and S. Adams, *Studies of lithium argyrodite solid electrolytes for all-solid-state batteries: Studies of lithium argyrodite solid electrolytes*, *physica status solidi (a)* **208**, 1804 (2011).
- [6] T. K. Schwietert, V. A. Arszewska, C. Wang, C. Yu, A. Vasileiadis, N. J. J. de Klerk, J. Hageman, T. Hupfer, I. Kerkamm, Y. Xu, E. van der Maas, E. M. Kelder, S. Ganapathy, and M. Wagemaker, *Clarifying the relationship between redox activity and electrochemical stability in solid electrolytes*, *Nature Materials* **19**, 428 (2020).
- [7] Y. Zhu, X. He, and Y. Mo, *Origin of outstanding stability in the lithium solid electrolyte materials: Insights from thermodynamic analyses based on first-principles calculations*, *ACS Applied Materials & Interfaces* **7**, 23685 (2015).
- [8] T. K. Schwietert, A. Vasileiadis, and M. Wagemaker, *First-principles prediction of the electrochemical stability and reaction mechanisms of solid-state electrolytes*, *JACS Au*, jacsau.1c00228 (2021).
- [9] N. J. J. de Klerk, I. Rosłoń, and M. Wagemaker, *Diffusion mechanism of Li argyrodite solid electrolytes for Li-ion batteries and prediction of optimized halogen doping: The effect of Li vacancies, halogens, and halogen disorder*, *Chemistry of Materials* **28**, 7955 (2016).
- [10] P. Adeli, J. D. Bazak, K. H. Park, I. Kochetkov, A. Huq, G. R. Goward, and L. F. Nazar, *Boosting solid-state diffusivity and conductivity in lithium superionic argyrodites by halide substitution*, *Angewandte Chemie International Edition* **58**, 8681 (2019).
- [11] A. Gautam, M. Sadowski, M. Ghidui, N. Minafra, A. Senyshyn, K. Albe, and W. G. Zeier, *Engineering the site-disorder and lithium distribution in the lithium superionic argyrodite $\text{Li}_6\text{PS}_5\text{Br}$* , *Advanced Energy Materials* **11**, 2003369 (2021).
- [12] M. A. Kraft, S. Ohno, T. Zinkevich, R. Koerver, S. P. Culver, T. Fuchs, A. Senyshyn, S. Indris, B. J. Morgan, and W. G. Zeier, *Inducing high ionic conductivity in the lithium superionic argyrodites $\text{Li}_{6+x}\text{P}_{1-x}\text{Ge}_x\text{S}_5\text{I}$ for all-solid-state batteries*, *Journal of the American Chemical Society* **140**, 16330 (2018).

- [13] N. Minafra, S. P. Culver, T. Krauskopf, A. Senyshyn, and W. G. Zeier, *Effect of Si substitution on the structural and transport properties of superionic Li-argyrodites*, *Journal of Materials Chemistry A* **6**, 645 651 (2018).
- [14] Z. Zhang, Y. Sun, X. Duan, L. Peng, H. Jia, Y. Zhang, B. Shan, and J. Xie, *Design and synthesis of room temperature stable Li-argyrodite superionic conductors via cation doping*, *Journal of Materials Chemistry A* **7**, 2717 (2019).
- [15] Z. Sun, Y. Lai, N. Lv, Y. Hu, B. Li, L. Jiang, J. Wang, S. Yin, K. Li, and F. Liu, *Insights on the properties of the O-doped argyrodite sulfide solid electrolytes ($\text{Li}_6\text{PS}_{5-x}\text{ClO}_x$, ($x = 0-1$))*, *ACS Applied Materials & Interfaces* **13**, 54924 54935 (2021).
- [16] B. W. Taklu, W.-N. Su, Y. Nikodimos, K. Lakshmanan, N. T. Temesgen, P.-X. Lin, S.-K. Jiang, C.-J. Huang, D.-Y. Wang, H.-S. Sheu, S.-H. Wu, and B. J. Hwang, *Dual CuCl doped argyrodite superconductor to boost the interfacial compatibility and air stability for all solid-state lithium metal batteries*, *Nano Energy* **90**, 106542 (2021).
- [17] Z. Fu, L. Zhang, J. E. Gritton, G. Godbey, T. Hamann, Y. Gong, D. McOwen, and E. Wachsman, *Probing the mechanical properties of a doped $\text{Li}_7\text{La}_3\text{Zr}_2\text{O}_{12}$ garnet thin electrolyte for solid-state batteries*, *ACS Applied Materials & Interfaces* **12**, 24693 (2020).
- [18] L. Zhou, A. Assoud, Q. Zhang, X. Wu, and L. F. Nazar, *New family of argyrodite thioantimonate lithium superionic conductors*, *Journal of the American Chemical Society* **141**, 19002 (2019).
- [19] Y. Kato, S. Hori, T. Saito, K. Suzuki, M. Hirayama, A. Mitsui, M. Yonemura, H. Iba, and R. Kanno, *High-power all-solid-state batteries using sulfide superionic conductors*, *Nature Energy* **1**, 16030 (2016).
- [20] W. Huang, C. LinDong, S. Hori, K. Suzuki, M. Yonemura, M. Hirayama, and R. Kanno, *Ionic conduction mechanism of a lithium superionic argyrodite in the Li-Al-Si-S-O system*, *Materials Advances*, 10.1039.D0MA00115E (2020).
- [21] A. Baktash, J. C. Reid, T. Roman, and D. J. Searles, *Diffusion of lithium ions in lithium-argyrodite solid-state electrolytes*, *npj Computational Materials* **6**, 162 (2020).
- [22] N. Minafra, M. A. Kraft, T. Bernges, C. Li, R. Schlem, B. J. Morgan, and W. G. Zeier, *Local charge inhomogeneity and lithium distribution in the superionic argyrodites $\text{Li}_6\text{PSLi}_5\text{X}$ ($X = \text{Cl}, \text{Br}, \text{I}$)*, *Inorganic Chemistry* **59**, 11009 (2020).
- [23] B. J. Morgan, *Mechanistic origin of superionic lithium diffusion in anion-disordered $\text{Li}_6\text{PS}_5\text{X}$ argyrodites*, *Chemistry of Materials*, acs.chemmater.0c03738 (2021).
- [24] H.-J. Deiseroth, S.-T. Kong, H. Eckert, J. Vannahme, C. Reiner, T. Zaiß, and M. Schlosser, *$\text{Li}_6\text{PS}_5\text{X}$: A class of crystalline Li-rich solids with an unusually high Li^+ mobility*, *Angewandte Chemie International Edition* **47**, 755 (2008).

- [25] K. Hogrefe, N. Minafra, I. Hanghofer, A. Banik, W. G. Zeier, and H. M. R. Wilkening, *Opening diffusion pathways through site disorder: The interplay of local structure and ion dynamics in the solid electrolyte $\text{Li}_6\text{P}_{1-x}\text{Ge}_x\text{S}_5\text{I}$ as probed by neutron diffraction and NMR*, *Journal of the American Chemical Society*, [jacs.1c11571](#).

5

AN ADVANCED MODEL FOR SOLID-STATE BATTERIES AND ITS MAIN CHALLENGES

This chapter is to be submitted: **Schwietert, T. K.**, Ombrini, P, Vasileiadis, A and Wagemaker, M., *An advanced model for solid-state batteries and its main challenges*

5.1. ABSTRACT

All-Solid-state batteries gain increasing interest due to the higher promised energy densities without the use of flammable liquid electrolytes. Two main issues for solid-state batteries are contact loss and interphase formation which both play a role at the solid electrolyte and active particle interfaces. Here, we present an advanced modular computational framework that is generally applicable for solid-state batteries with different electrodes and corresponding microstructures. The model is based on Multiphase Porous Electrode Theory, where for Li-ion transport in the solid electrolytes a regular solution free energy functional is considered, additionally, a model for contact loss and a diffusive interlayer to model SEI formation, coatings and liquid interphases are implemented. The theoretical results of the solid electrolyte model are compared with conventional liquid electrolyte models using a phase separating electrode to find the optimal conditions and bottlenecks of solid electrolytes in solid-state batteries. Mesoscopic modeling of solid-state batteries and the effect of solid ion transport, contact loss and interphase formation is crucial to understand, optimize and analyze the performances of all-solid-state batteries.

5

5.2. INTRODUCTION

Solid-state batteries have the potential to outperform conventional liquid electrolyte batteries in terms of energy density and safety. The research in novel solid electrolyte materials has led to the discovery of Li-ion conducting solids that perform at similar rates as its liquid counterpart, with the advantage of being safer, having more freedom in design, and potentially allowing more energy-dense electrode materials. There are, however, still challenges to overcome, the three main challenges for solid-state batteries are: maintaining physical contact between the electrode and electrolyte, formation of interfacial layers hindering Li-ions and electrons from participating in the desired electrochemical reactions and inhomogeneous deposition of metal anodes.¹⁻³ To understand the effect of these bottlenecks on the performance of solid-state batteries, physics-based models are required that simulate solid-state ion transport and can capture these remaining issues in solid-state batteries.

Modeling has been very efficient in validating Li-ion batteries, especially Porous Electrode Theory (PET) developed by Newman and coworkers is still extensively used to model intercalation electrodes. More recently, Multiphase Electrode Theory (MPET) based on non-equilibrium thermodynamics described by Bazant et al. has been developed, MPET can effectively capture the free energy functional of battery systems, successfully modeling phase transitions, spinodal gaps and kinetic limitations in LiFePO_4 ⁴⁻⁸, graphite, anatase TiO_2 ⁹ and spinel $\text{Li}_4\text{Ti}_5\text{O}_{12}$ ¹⁰. Phase field approaches are also used to study the microstructure in solid-state batteries, where it can be used to model the pore-electrolyte structure¹¹ and grain-boundaries¹².

Multiple models for solid-state batteries have been described in the literature. Most of these models are based on thin-film solid electrolytes, with the advantage of having a simple geometry with two flat electrodes,¹³ however, most solid electrolyte batteries described in experimental research use composite electrodes where the solid electrolyte and active materials are mixed, effectively obtaining a composite electrode with a porous

structure which can be modeled by PET based models.^{14,15} For transport in amorphous and polymer solid electrolytes, it can be assumed that a part of the Li-ions are bound in the structure, and only a fraction of Li-ions is mobile.^{16,17} However, for most inorganic solid electrolytes, all Li-ions participate in the diffusion process.^{1,18} Recent models also capture the free energy functional to simulate the transport of species through a solid electrolyte. Landstorfer et al. derived a model for the ion transport in solid electrolytes similar to that derived for solid transport in electrode-based models.¹³ This computational framework was applied to simulate the space-charge regions in a thin-film solid-state battery.

One of the main challenges in solid-state batteries is contact loss near the electrolyte-electrode interface.^{1,2,17,19,20} The insufficient mechanical contact facilitates cathode particles to become completely isolated from the solid electrolyte, where a gap of only sub-nanometers is enough to effectively lose the contact. Moreover, after cycling cracks can isolate crystallite grains in polycrystalline particles and become isolated because of the definite volume of solid electrolytes.²¹ While the poor contact between electrode and electrolyte can be improved by mechanical pressing, there often remains contact loss after solid-state battery assembly²². During cycling contact loss can increase by the shrinkage and expansion of electrode particles.²⁰ Also the void space connected to the contact loss is of importance as this gives an extra term in the porosity for the electrolyte^{23–25}, that can influence the rate capability of the solid-state battery.

Next to contact loss, interphase formation is a main challenge in solid-state batteries.^{1,2,26,27} These interphases are formed around the active material and can hinder the Li-ions moving from the electrolyte towards the electrode material.^{20,26,28} Li-ion transport through these layers is often sluggish, and these layers have different material properties as the bulk electrolyte. In contrast to most models for interphase formation in literature, where an extra resistance in the overpotential is applied^{29,30}, we define an interphase layer with a specific length that can be modified with specific transport properties. Additionally, different transport equations can be implemented in the interface region enabling the simulation of hybrid solid – liquid electrode systems such as porous SEI, coatings, liquid interphases and space-charge regions.

Here we use Modified Porous Electrode Theory to develop a methodology to study solid-state batteries that is generally applicable and can be used for different solid electrolytes, electrodes and interphase models, the code is freely available. A solid-state transport model is established based on the regular solution model and the effect of solid electrolyte transport on the battery performance is investigated for different battery geometries and is compared to similar size liquid electrolyte systems. Furthermore, the effect of contact loss between the electrode and electrolyte is studied considering a contact loss distribution throughout the electrode. Additionally, a model for interphase transport between the electrode – electrolyte interface is implemented where a specific material with corresponding transport properties is simulated. This advanced model framework for solid-state batteries will help experimentalists to understand, analyze, design and optimize new and better solid-state batteries.

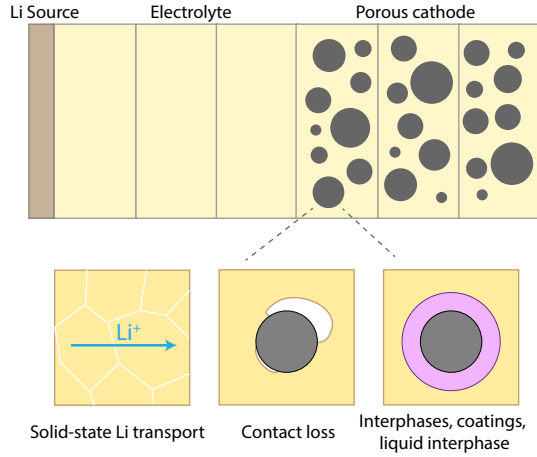


Figure 5.1: Schematic representation of the model used for solid-state batteries. The porous electrode is separated in volumes where the electrode particles interact with the electrolyte. In the modular model, solid-state transport, contact loss and interphase diffusion is simulated in a full battery system.

5

5.3. METHODS

The model is based on non-equilibrium electrochemical thermodynamics as implemented in the open-source software package MPET introduced by Smith and Bazant.³¹ In the computational framework, the corresponding transport equations for solid electrolytes are implemented in the code and an optional interphase layer between the electrolyte and particles is added. The battery is divided into an anode, electrolyte and cathode consisting of separate volumes. All the electrolyte volumes are connected in series and are coupled in parallel with the active particles where Li-ions are exchanged. In the porous electrode volumes, the particles reside in the electrolyte where a porous geometry is modeled. For composite solid electrolytes this model can resemble the microstructures of the battery.^{19,21,24,32} Similar to liquid electrolytes, solid electrolytes also have inactive parts such as voids and a carbon matrix, that is modeled by the porosity ϵ of the electrolyte. The tortuosity τ is a function of the porosity ϵ given by the Bruggeman relationship $\tau = \epsilon^a$.

TRANSPORT EQUATIONS

For the formulation of the transport equation, a binary electrolyte with positive and negative charged species i , that carry z number of elementary charge e is considered. In the bulk electrolyte we apply the charge neutrality condition $\sum_i z_i c_i = 0$, hence, for this binary material we can define a fixed concentration $c = c_+ = c_-$. The mass and charge balances in the electrolyte are in the following form,³¹

$$\epsilon \frac{\partial c_i}{\partial t} = -\nabla \cdot \mathbf{F}_i + R_i \quad (5.1)$$

$$\mathbf{0} = \nabla \cdot \mathbf{i} - \sum_i z_i e R_i \quad (5.2)$$

Where \mathbf{F} is the charged particle flux, R is the consumption rate from the electrolyte, \mathbf{i} the current density and e is the electron charge. As the charge is conserved in the electrolyte we can couple the reaction rate to the current density into the particles, $R_+ = a_p j_{\text{in}}$, where a_p is the surface area of the particle and j the flux of cations into the particles, at the particle interface we find $\nabla \cdot \mathbf{i} = -e a_p j_{\text{in}}$.

In the electrolyte, transport is given by the Nernst-Planck equation for concentrated solution theory,¹⁵

$$\mathbf{F}_i = -\epsilon D_{\text{chem},i} \nabla c_i - z_i D_i \epsilon c_i \nabla \phi \quad (5.3)$$

where D_{chem} is the chemical diffusivity $D_{\text{chem}} = D_0 (1 + \frac{\partial \ln \gamma}{\partial \ln c})$, that is dependent on the concentration and the activity coefficient γ . Using that the current density \mathbf{i} is the sum of the positive and negative particle fluxes we obtain,

$$\mathbf{i} = -e \epsilon (D_{\text{chem},+} - D_{\text{chem},-}) \nabla c - e (z_+ D_+ + z_- D_-) \epsilon c \nabla \phi. \quad (5.4)$$

By substituting equation 5.3 into equation 5.1 and using the current density the final mass balance becomes

$$c \frac{\partial c_i}{\partial t} = \nabla \cdot (\epsilon D_{\text{amb}} \nabla c) - \nabla \cdot \left(\frac{t^i \mathbf{i}}{e} \right) - a_p j_{\text{in}} \quad (5.5)$$

with $D_{\text{amb}} = \frac{z_+ D_+ D_{\text{chem},-} + z_- D_- D_{\text{chem},+}}{z_+ D_+ + z_- D_-}$, this is the formulation used in most PET models.¹⁵

DILUTE ELECTROLYTE

In the dilute electrolyte case, no friction between the cation and anion is present and the activity coefficient in the chemical diffusion is unity, $D_{\text{chem}} = D_0$. The charged particle flux (equation 5.3) and current density simplify to:

$$\begin{aligned} \mathbf{F}_i &= -\epsilon D_i \nabla c_i - z_i D_i \epsilon c_i \nabla \phi \\ \mathbf{i} &= -e \epsilon (D_+ - D_-) \nabla c - e (z_+ D_+ + z_- D_-) \epsilon c \nabla \phi. \end{aligned} \quad (5.6)$$

Together with the charge and mass balances equations 5.1 and 5.2 this defines the dilute electrolyte model.^{15,31}

STEFAN-MAXWELL MODEL

In the concentrated electrolyte model, the diffusion equation for multi-component species is considered,¹⁵

$$c_i \nabla \mu_i = \sum_j K_{ij} (\mathbf{v}_j - \mathbf{v}_i) = k_B T \sum_j \frac{c_i c_j}{c_T \mathcal{D}_{ij}} (\mathbf{v}_j - \mathbf{v}_i) \quad (5.7)$$

where \mathbf{v} is the velocity of species i , K_{ij} are the friction coefficient between different species and c_T the total concentration. This model implements the interaction between charged species and the neutral solvent. The charged particle flux can be written as¹⁵:

$$\mathbf{F}_i = -\frac{v_+ \epsilon}{\tau} D_l \nabla c_l - \frac{t_i^0 \mathbf{i}_l}{z_i e} \quad (5.8)$$

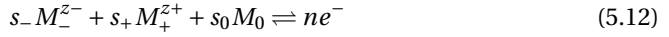
where,

$$D_l = \mathcal{D} \frac{c_T}{c_0} \left(1 + \frac{\partial \ln y_{\pm}}{\partial \ln \tilde{c}} \right) \quad (5.9)$$

$$\mathcal{D} = \frac{D_{0,+} D_{0,-} (z_+ - z_-)}{z_+ D_{0,+} + z_- D_{0,-}} \quad (5.10)$$

$$\frac{1}{\sigma} = \left(\frac{-k_B T}{c_T z_+ z_- e^2} \right) \left(\frac{1}{\mathcal{D}_{\pm}} + \frac{c_0 t_{-}^0}{c_+ D_{0,-}} \right). \quad (5.11)$$

The diffusivities and transference numbers with subscript 0 are with respect to the solvent, y_{\pm} is the mean molar activity coefficient. If the total reaction



is considered where M is the chemical formula species i , the current density is given by^{15,31},

$$\mathbf{i} = \frac{\sigma \epsilon}{\bar{T} \tau} \left(\nabla \phi + \frac{v k_B T}{e} \left(\frac{s_+}{n v_+} + \frac{t_+^0}{z_+ v_+} - \frac{s_0 c}{n c_0} \right) \times \left(1 + \frac{\partial \ln y_{\pm}}{\partial \ln \tilde{c}} \right) \nabla \ln \tilde{c} \right). \quad (5.13)$$

When the Stefan-Maxwell model is considered for the electrolyte the set of equations 5.1,5.2,5.9,5.13 determine the Stefan-Maxwell electrolyte.¹⁵ In the remaining of the Chapter the fitted parameter set of Bernardi and Go for a LiPF₆ in EC/CMC electrolyte is adopted for the Stefan-Maxwell model.³³

TRANSPORT EQUATIONS IN SOLID ELECTROLYTES

To derive the transport equations in the solid electrolyte the regular solution model is considered, similar as derived for diffusion in phase separating solid electrodes, where entropic and enthalpic interactions are considered^{12,13,34}. By taking the functional derivative of the Gibbs free energy, the chemical potential μ for the regular solution model is given by¹³,

$$\mu = k_B T \ln \left(\frac{\tilde{c}}{1 - \tilde{c}} \right) + \alpha_s (1 - 2\tilde{c}) + z e \phi \quad (5.14)$$

where k_B is the Boltzmann constant T the temperature, \tilde{c} the non-dimensionalized concentration (c/c_{\max}), α_s the energy of mixing between Li-ions and vacancies in the structure. Assuming lattice gas diffusion, where a free site needs to be available for diffusion, the charged particle flux is determined by,

$$\mathbf{F}_i = -\frac{D_0}{T} c_i (1 - \tilde{c}) \nabla \mu \quad (5.15)$$

Substituting equation 5.14 in equation 5.15 the chemical diffusion is then given by³⁵,

$$D_{\text{chem}} = D_0(1 - 2\tilde{\alpha}_s\tilde{c} + 2\tilde{\alpha}_s\tilde{c}^2) \quad (5.16)$$

where $\tilde{\alpha}_s$ is $\alpha_s/k_B T$.³⁵ For which, in the dilute case ($c \rightarrow 0$) the intrinsic diffusivity is obtained, $D_{\text{chem}} = D_0$. For solid-state electrolytes the nondimensionalized concentration is obtained by normalizing against the maximum cation concentration ($c_{\text{ref}} = c_{\text{max}}$). This chemical diffusion can be used to obtain a description of the solid electrolyte. The charge flux and mass balance are given by,

$$\mathbf{i} = -e\epsilon(D_{\text{chem},+} - D_{\text{chem},-})\nabla c - e(z_+D_+ + z_-D_-)\epsilon c\nabla\phi \quad (5.17)$$

$$e\frac{\partial c_i}{\partial t} = \nabla \cdot (\epsilon D_{\text{amb}}\nabla c) - \nabla \cdot \left(\frac{t^i \mathbf{i}}{e} \right) - a_p j_{in} \quad (5.18)$$

since the anionic framework is fixed in the crystal and the electronic conductivity is low, Li is the only moving charge carrier inside the bulk of the inorganic solid electrolytes, this results in a transference number t^+ in most inorganic solid electrolytes close to unity ($t^+ = (z_+D_+)/ (z_+D_+ + z_-D_-)$).^{36,37} In combination with the (semi)charge neutrality in the bulk electrolyte $z_+c_+ = z_-c_-$ this suppresses gradients in the Li-ion concentration throughout the bulk electrolyte regions ($\nabla c \approx 0$), which simplifies the transport equations as all diffusion terms drop out and only a migration term is left in the current density, effectively obtaining Ohms law,

$$\mathbf{i} = -e(z_+D_+ + z_-D_-)\epsilon c\nabla\phi. \quad (5.19)$$

Around the particle interface, the chemical potential difference between the electrolyte and electrode can decompose or form space-charge layers. In the case a space-charge layer forms the assumption of quasi-neutrality is no longer valid and the Poisson equation should be considered. However, because the Li concentration in solid electrolytes is relatively large, the thickness of the space-charge layer relatively small, the Debye length that determines the width of the space-charge layer is in the order of ~ 1 Å, for which limited effects are expected from the space-charge layer on battery operation.³⁸

ELECTRODE TRANSPORT

In this research the LiFePO₄ (LFP) electrode transport model mostly developed by Bazant and co-worker is used³⁵, where the chemical potential is used as derived from the Cahn-Hilliard free energy functional with a gradient energy coefficient κ and including the coherent stress penalty B .^{4,6,35}

$$\mu = k_B T \ln \left(\frac{\tilde{c}}{1 - \tilde{c}} \right) + \alpha_s(1 - 2\tilde{c}) + \frac{B}{c_{\text{max}}}(\tilde{c} - \bar{c}) - \frac{\kappa_{\text{LFP}}}{c_{\text{max,LFP}}}\nabla^2 \tilde{c}. \quad (5.20)$$

At the anode side a Li reservoir is used with a constant reaction rate and chemical potential, plating dynamics and dendritic effects are not captured in the simulations. In the simulations the electronic conductivity is considered not limiting and is therefore neglected.

KINETICS

The reaction kinetics is applied by the generalized Butler-Volmer equation,

$$i = i_0 \left(e^{-\frac{\alpha e \eta_{\text{eff}}}{k_B T}} - e^{\frac{(1-\alpha) e \eta_{\text{eff}}}{k_B T}} \right) \quad (5.21)$$

Where α is a symmetry coefficient, i_0 the exchange current density and η_{eff} the effective overpotential. The exchange current density i_0 is determined as is implemented by Bazant⁷,

$$i_0 = \frac{nk_0(a_O a_e^n)^{1-\alpha} a_R^\alpha}{\gamma_{\ddagger}} \quad (5.22)$$

where a_O and a_R are the activities of the oxidized and reductive species, a_e the activity of the electrons and where the activity of the activated state for LFP determined by $\gamma_{\ddagger} = \frac{1}{1-\tilde{c}}$.^{5,39} Using equation 5.14 and the definition of the chemical potential, the activity of the solid electrolyte is given by $a_{\text{slyte}} = \frac{\tilde{c}}{1-\tilde{c}} e^{\tilde{a}_s(1-2\tilde{c})}$.

5

CONTACT LOSS

As shown in Figure 5.1 contact loss at the solid electrolyte and electrode interface is considered. To model the contact loss an effective area ratio γ is implemented which is determined by the ratio between the contact area with contact loss A and the perfect contact area A_0 .¹⁷

$$\gamma = \frac{A}{A_0} \quad (5.23)$$

In the porous structure a contact loss distribution for every particle can be applied in the porous electrode. The contact ratio γ can be used to tune the effective area of every single particle which directly affects the exchange current density implemented in the Butler-Volmer equation.

INTERLAYER REGION

To model interphase formation, additional electrolyte volumes are implemented between the electrolyte and electrode particles. In these additional volumes specific transport equations and materials properties can be modelled between the electrolyte and the particles. Here, we use the region as a diffusive interlayer and electrochemical reactions are not considered. To derive the electrical potential difference at the particle - interlayer, the electrochemical potential is considered constant $\mu_{\text{elyte}} = \mu_{\text{int}}$.

BOUNDARY CONDITIONS

Boundary conditions are used as implemented in MPET simulations.³¹ The reaction rates in each particle are equal to the systems total current, and there are no net particle fluxes or current densities into the current collector at the cathode. When Li metal is used as anode, the boundary condition at that side is replaced where the flux is equal to the reaction rate into the particles.

5.4. RESULTS

TRANSPORT IN SOLID ELECTROLYTE VERSUS BINARY DILUTE AND STEFAN-MAXWELL CONCENTRATED ELECTROLYTE MODEL

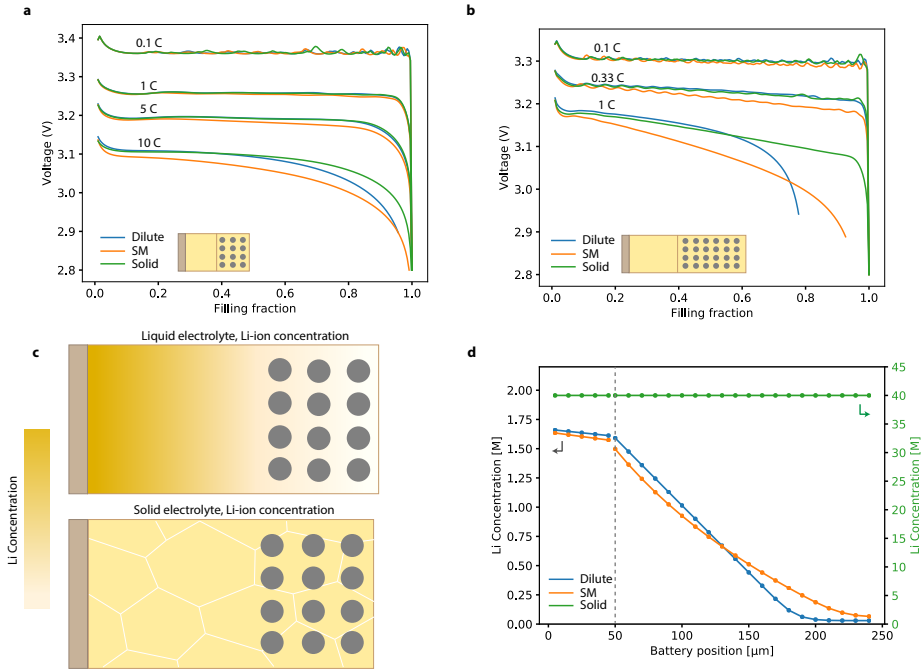


Figure 5.2: Simulated voltage curves for different C-rates and Li concentration in solid and liquid electrolytes, a Simulated voltage curves for different C-rates using dilute, Stefan-Maxwell and solid transport models in a 50 μm separator, 50 μm cathode Li/LFP battery. The filling fraction represents the fraction of the total particles that is filled with Li. **b** Simulated voltage curves for a 200 μm cathode Li/LFP battery. **c** Schematic representation of the concentration difference in liquid and solid-state batteries. **d** Concentration at the end of discharge for the different models for a 1C 200 μm cathode from Figure 5.2b.

First, the differences between liquid and solid-state electrolyte transport and the effect on the battery operation are investigated. As reference a solid electrolyte with a comparable Li-ion concentration as sulfide solid electrolyte $\text{Li}_6\text{PS}_5\text{Cl}$ is considered. The liquid electrolyte is based on a LiPF_6 electrolyte⁴⁰ which is integrated in a LFP half cell, the LFP parameters are taken from literature. To make an equal comparison between the models, the Li-ion conductivity is equalized in the dilute and solid model and adjusted to the fitted Stefan-Maxwell model. The relevant parameters are given in Table 5.1 in Section 5.6.

The voltage curves corresponding to the different models are shown in Figure 5.2. In Figure 5.2a a battery with a 50 μm separator and equal length LFP cathode is simulated, corresponding to the target dimensions of commercial solid-state batteries⁴¹. The voltage curves accurately demonstrate the phase separation behavior of LFP where a flat

voltage plateau at low C-rates, and solid solution behavior at higher current densities are obtained.^{39,42} The fluctuations in the voltage curves at low rates originate from the fast lithiation of individual particles shown in similar LFP based phase field models.³¹

For low C-rates, relatively small differences in voltage curves are shown as the system is mainly limited by the reaction kinetics in the LFP particles. At 5 and 10C voltage differences become more distinct. The high positive transference number in solid electrolytes in combination with charge balance in the bulk electrolyte cause concentration gradients to become small and Li-ion transport migration dominated.⁴³ In the solid electrolyte, this results in a near-constant Li-ion concentration in the bulk electrolyte. In the dilute and Stefan-Maxwell liquid electrolyte models, concentration gradients are formed due to relatively fast anion mobility causing Li-ion transport in the electrolyte to become more diffusion dependent.

In Figure 5.2b a battery with a 200 μm cathode is simulated and the system becomes more limited by electrolyte transport at lower C-rates. For the simulation with the solid electrolyte, a more gradual decrease in the voltage curve is shown resulting in a higher overall capacity. As the concentration in the solid electrolyte remains constant, the Li-ion depletion is limited around the LFP particles throughout the electrode, hence, the Li transport is more efficient over longer distances. For the dilute liquid electrolyte, Li-ion depletion lowers the concentration dependent activity and hence the local potential around the cathode particles close to the current collector which increases the overpotential, resulting in a voltage drop at higher filling fractions for thicker battery systems. For high C-rates the relatively fast diffusion and high local concentrations at the separator side raise the potential in the beginning of the discharge, however at the current collector side depletion causes high overpotentials for higher filling fractions. The Stefan-Maxwell concentrated electrolyte model, which includes concentration dependence electrolyte transport, shows intermediate effects where the voltage curve has a steeper slope and reaches higher capacities compared to liquid electrolytes.

In Figure 5.2d, the concentration in the electrolyte at the end of discharge of the 1C simulation for the 200 μm cathode is shown. In the inorganic solid electrolyte the Li-ion concentration is around 40 times higher than in liquid electrolytes. Similar to the study of Valøen and Reimers⁴⁰ and Smith and Bazant³¹, the dilute model shows more polarization compared to the Stefan-Maxwell model where a concentration dependent diffusivity is implemented. In contrast, in the dilute model only anion and cation interactions are considered. Again, the voltage of the concentrated electrolyte shows a more linear slope in voltage and reaches a higher capacity compared to the dilute model.³¹

The geometry of the cell is crucial to understand the kinetics of solid electrolytes and essential to optimize the cell designs. To evaluate the impact of the separator length of the solid electrolyte on the battery performance the thickness is varied from 50 to 2000 μm . The results are compared to liquid electrolyte models as shown in Figure 5.3a. As Li transport in the solid electrolyte is mainly dominated by migration the electrolyte behaves more ohmic (equation 5.19) and an initial drop in the voltage occurs as the electric potential in the electrolyte is linearly dependent on the electrolyte distance. In the dilute electrolyte case, the concentration gradient through the separator promotes diffusive transport at the separator side showing low overpotentials at the beginning of the discharge. However depletion of the Li concentration in the electrolyte at the current col-

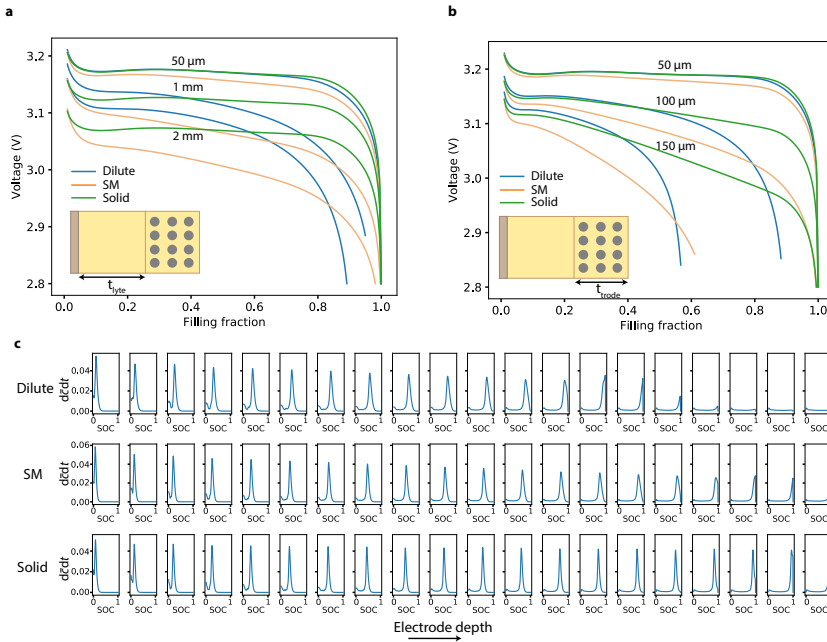


Figure 5.3: Simulated voltage curves for different separator and cathode lengths and lithiation rate in the cathode particles, a Simulated voltage curves for different separator lengths using the Dilute, Stefan-Maxwell and Solid transport models for a 50 μm cathode in a $\text{Li}|\text{Solid electrolyte}|\text{Li}_x\text{FePO}_4$ battery at 3C. **b** Simulated voltage curves for different separator lengths for a battery with a 50 μm separator at 3C. **c** The average concentration change of Li in the particles along the thickness of the electrode as a function of the state of charge. Here the maximum state of charge is related to the practical capacity obtained from the simulations. The separator is situated on the left and the current collector on the right.

lector increases the overpotential for higher C-rates. The Stefan-Maxwell concentrated electrolyte model has less polarization than the dilute model and reaches a higher capacity.

Next, we evaluate the effect of the electrode thickness by varying the cathode length from 50 to 150 μm as shown in Figure 5.3b. For solid transport a clear decrease in the slope of the voltage curve is shown. This again shows the more ohmic behavior of the solid electrolyte originating from Li migration, which predicts a linear voltage response for varying electrode depth. Therefore, a sloping curve is shown for the phase separating LFP for thicker electrodes. In the dilute electrolyte, the cathode length strongly increases the depletion near the current collector due to the high polarization in the electrolyte and increases the overpotential for a higher state of charge, showing a sharp voltage drop for higher electrode thickness. The Stefan-Maxwell concentrated electrolyte model shows both polarization and a sloping voltage curve reaching a higher filling fraction compared to the dilute model for thicker cathodes. The results show that all-solid-state batteries have better performances for thicker cathodes at higher rates than liquid electrolytes, enabling larger energy densities in a battery pack due to less packaging required.

It must be noted that in the simulations the Li-ion conductivity of solid electrolytes is equal to liquid electrolytes, whereas in practice, the Li-ion conductivity of solid electrolytes is generally lower³, and in these simulations contact loss and interphase formation are not yet taken into account.

In Figure 5.3c the average lithiation rate in the cathode particles over the cathode length is shown for a 100 μm cathode at 3C. In the simulations the electronic conductivity is assumed to be not limiting and is neglected in the simulations, such that the lithiation starts from the separator side. The simulations show that the lithiation starts rapidly for the dilute model, indicating that lithiation proceeds fast because of high local concentrations near the separator. Closer to the current collector the rate of lithiation becomes lower, indicating that the charge transfer is more sluggish compared to the solid and Stefan-Maxwell models. This effect originates from local Li depletion in the electrolyte near the particle which limits the particle from lithiating further. The Stefan-Maxwell model shows a more similar trend with lithiation starting fast close to the separator side and slowing down near the current collector. This effect is less distinct as in the dilute case as the solvent interactions slow down the polarization. The solid electrolyte shows a more constant lithiation rate as function of time for particles along the depth of the electrode. This is caused by the Li concentration in the solid electrolyte that shows minor fluctuations as function of the electrode depth (Figure 5.2d) and the lithiation rate in the depth of the electrode is shifted by the state of charge.

CONTACT LOSS

This section investigates the effect of contact loss in a solid-state battery. Contact loss is one of the main challenges in solid-state batteries strongly affecting the reactive area of particles, and hence limiting the reaction rate into the particles. Here, contact loss is captured by an effective area around the particles, effectively altering the reactive area for Li-ions and electrons. In Figure 5.4a a schematic representation of contact loss in solid-state batteries is presented, indicating the areas where contact loss occurs, closely matching SEM and tomography experiments.^{19,32,45}

Particle sizes and voids sizes have specific size distributions throughout the electrode, because contact loss is related to these variables, likewise, contact loss is expected to have a distribution over the electrode. Where in literature a constant contact loss is often considered for all particles^{17,45}, here multiple particles are simulated where a contact loss distribution is applied over the particles in the electrode, similar as simulated for the particle size distribution, a lognormal contact distribution is used to capture the contact loss distribution in the electrode. The voltage curves for a battery with a 100 μm separator and 100 μm electrode, with full contact, a constant contact loss of 60 % for all particles, and an electrode with an inverse lognormal distribution of contact loss through the electrode with a mean of 0.6 and a standard deviation of 0.4 are simulated and shown in Figure 5.4b.

The 1C voltage curve without contact loss shows a flat plateau around 3.22 V indicating phase separation of the LFP particles. When an effective constant contact fraction of 0.6 is applied to the particles (orange curve) and the system is in the spinodal region below the critical current where the exchange current density is not limiting, electrode particles phase separate resulting in a similar voltage plateau for batteries with contact

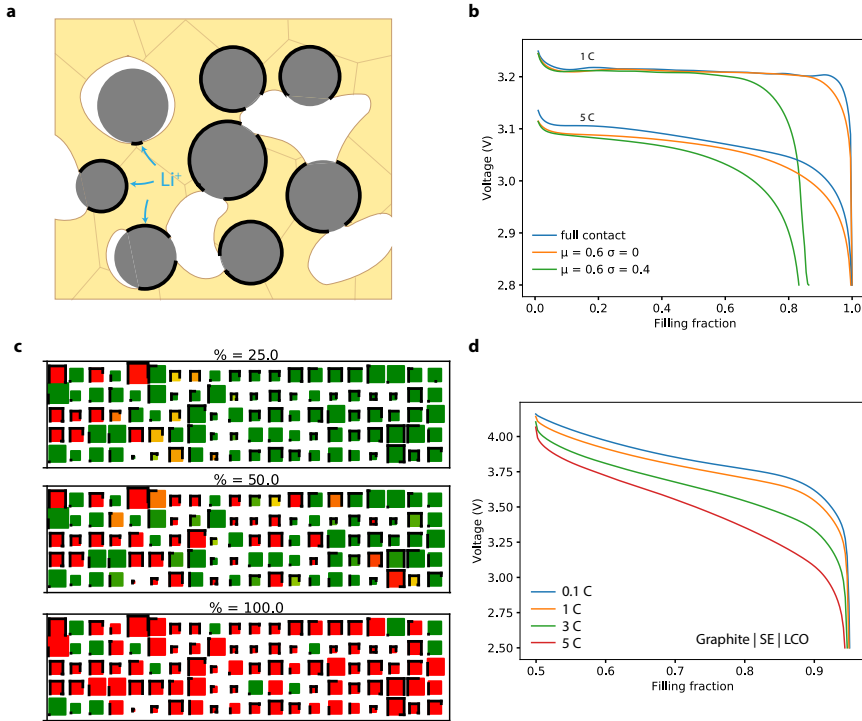


Figure 5.4: Schematic representation of contact loss in a solid-state battery, simulated voltage curves for different contact loss distributions and a simulated voltage curve of a graphite|SE|LCO battery, a Schematic of contact loss in solid-state batteries. b Simulated voltage curves for a Li/LFP battery with a 100 μm separator, 100 μm solid electrode without contact loss, a contact loss of 60 % for all particles and an electrode with an inverse lognormal distribution of contact loss fraction through the electrode with a mean of $\mu = 0.6$ and a standard deviation of $\sigma = 0.4$. c Simulated electrode with lithiating particles at 25 %, 50 % and 100 % state of charge, a red particle indicates a lithiated particle and green delithiated particle, with a black line contact of the particle is indicated. In the simulation the particles are considered as characteristic LFP platelet shaped particles and lithiation proceeds through the [010] facet. The state of charge is relative to the practical capacity from the simulations. d Simulated voltage curve of a graphite | SE | LCO battery in MPET with electrode parameters from the Lionsimba software.⁴⁴

loss and full contact. However, for the electrode with the lognormal contact distribution applied, a rapid drop in the voltage curve is shown around a cathode filling fraction of 0.6. At the beginning of the discharge the particles with higher contact, are not limited by surface potentials and lithiate at equal potentials as without contact loss. However at the end of discharge, the particles with limited contact start to dominate the kinetics, and cannot lithiate due to the low local exchange current density which quickly raises the overpotential. The same effect is shown in Figure 5.4c where the lithiation degree of the particle with contact distribution is shown. The contact is indicated with a black line around the particle. At 25% state of charge (relative to the practical capacity from the simulations), the particles with sufficient contact at the separator side start to lithiate at the same overall potential as the cathode without contact loss. At 50% state of charge the particles with most contact throughout the electrode are lithiated continuing the voltage plateau. Before the end of discharge, the particles with limited contact start to dominate the reaction showing higher overpotentials, at 100% state of charge the particles with limited contact cannot lithiate at the given 1C current density. This effect could explain the lower capacities found in solid-state batteries with limited contact loss and demonstrates the importance of relatively high pressures that are typically applied in solid-state batteries to keep sufficient contact.^{1,2}

5

In the 5C voltage curves an initial jump in the voltage curve of 10 mV is shown for both curves with contact loss. For higher current densities, the battery kinetics is increasingly determined by the local surface potential of the active particles which is controlled by the exchange current density. If the current density exceeds a critical value phase separation is suppressed and the LFP transitions into a solid solution regime.^{39,42} Because contact loss is directly affected by the exchange current density a voltage drop is shown for both contact fractions in this 5C solid solution region.

To show the modularity of the code, the solid electrolyte model is applied on a graphite - LiCoO₂ parameters set which has been developed by Torchio et al. in the Lionsimba software⁴⁴ which has been implemented in MPET. An 80 μm cathode, 88 μm anode and a 25 μm electrolyte are considered, the voltage curves are shown in Figure 5.4d. For the electrodes, a solid solution reaction is assumed, where similar to most PET models, the chemical potential and OCV are fitted. The simulated voltage curve in Figure 5.4d shows the solid solution behavior of LCO by a sloping voltage curve similar to the models where 1D diffusion is considered. In these simulations there are no contact losses applied. That fitted porous electrode models can predict voltage curves in solid solution materials has also been shown in recent literature.^{46,47}

TRANSPORT INTERLAYER

Interphase formation is one of the main challenges in solid-state batteries.^{1,2,26,48} The effect of an diffusive interlayer between the active particles and electrolyte is investigated. First, a solid electrolyte with a solid interlayer with varying cation conductivities is considered. In practice this can be a solid coating or solid SEI products, where the conductivity can be orders of magnitude lower as in the electrolyte.¹¹ At the interface the electrochemical potential is considered constant as stated in Equation 5.14 which is valid for systems in thermodynamic equilibrium. For the interphase depicted in Figure 5.5b the solid electrolyte parameters of Table 5.1 are used with different cation diffusion constants.

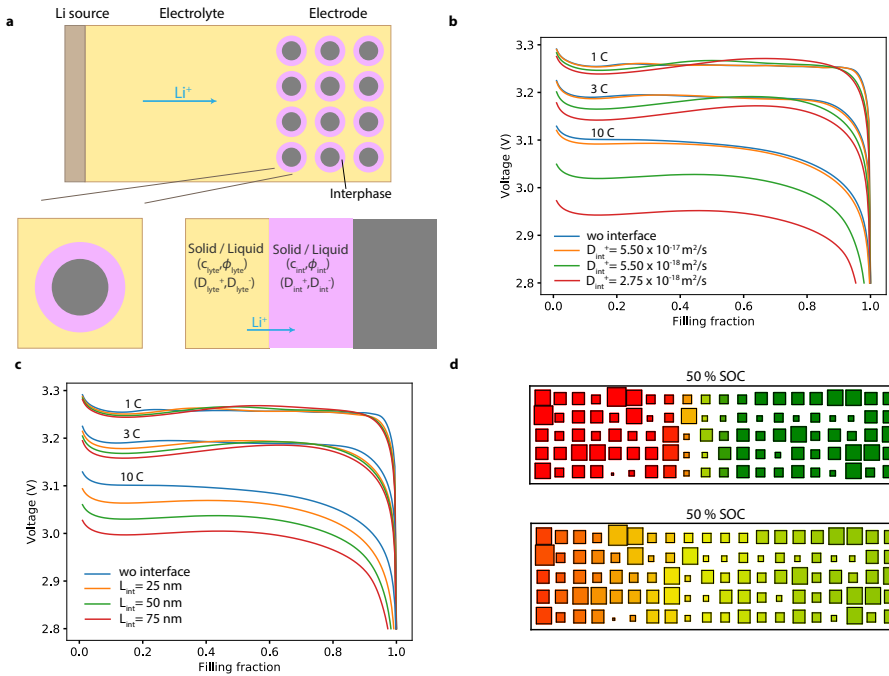


Figure 5.5: Schematic representation of the interphase model, simulated voltage curves for different interphases and a lithiation profile, a Schematic of the interfacial diffusion layer in a solid-state battery. **b** Simulated voltage curves for a 50 μm separator, 50 μm electrode, 50 nm interface with solid electrolyte transport for different conductivities **c** Simulated voltage curves for a 50 μm separator, 50 μm electrode and varying interphase thickness for an electrode without an interface with dilute (liquid) electrolyte diffusion with a diffusion constant for the cation and anion of $D_+ = 2.20 \times 10^{-16} \text{ m}^2/\text{s}$ and $D_- = 2.94 \times 10^{-16} \text{ m}^2/\text{s}$. **d** Simulated lithiation profile for a solid electrode with LFP electrode without diffusive interface and with a interfacial diffusion at 50 % state of charge.

Figure 5.5b shows the voltage curve of a simulation of a solid-state battery with a 50 nm interphase with varying Li-ion diffusivities at 1C, 3C, and 10C. When decreasing Li-ion diffusivity in the interface, the voltage curve shows the quasi-solid solution of LFP, where the voltage curve follows the homogeneous equilibrium chemical potential based on the regular solution model, where the limiting overpotential of the interphase surpasses the solid-solution voltage barrier and suppresses phase separation. When the diffusivity in the interphase is further decreased, (green and red curves in Figure 5.5b) an ohmic voltage drop appears as predicted by the Li migration in solid electrolytes. As the transport in the interphase becomes limiting more particles become active as for a population of particles it is energetically favorable to distribute the current density over multiple particles. As a consequence, the reaction front width and the active particle fraction increases. This effect is shown in Figure 5.5d where the lithiation rate of the particles in the electrode is shown for the 10C battery without an interphase and with a $2.75 \times 10^{-18} \text{ m}^2/\text{s}$ interphase. Without the interlayer, the reaction front is more narrow and with lower diffusivity in the interlayer as more particles get active and the reaction front is wider. This is a similar effect as described for high current densities in LFP where a solid solution transition occurs after reaching a critical current density, however in this case the unstable region in the voltage curve does not decrease by concentration-dependent activity as the solid interphase has a low concentration dependence of the applied current.

Solid-state batteries with small added amounts of liquid electrolyte or ionic liquid have become increasingly more used in literature.⁴⁹ Liquid is added to the electrode particle to make better contact with the active particles. In Figure 5.5c a solid-state battery with solid transport and a dilute model in the interphase is shown. When the interphase width is increased, a similar change in voltage curve is shown as for the solid interphase with changing diffusion constant, where a quasi solid solution voltage curve is shown. If the liquid interphase is not limiting, the hybrid solid-liquid systems benefit from both the solid transport and the wetting of voids around the particles by the liquid electrolyte. Where the small fraction of liquid does not deplete as fast as in the full liquid cell as the diffusion distances are smaller and Li transport through the solid-electrolyte benefits from long range solid-state migration.

5.5. CONCLUSION

An advanced mathematical model for simulating solid-state batteries with contact loss and interphase formation is presented. Solid-state Li-ion transport is described by the regular solution free energy functional is implemented in the computational framework. Due to the high cation transference number in solid electrolytes concentration gradients are small and Li transport is migration dominated. The small concentration gradients in solid-state batteries cause less electrolyte depletion in the electrodes, enabling thicker electrodes. A simulated contact loss distribution shows that contact at the electrolyte-electrode interface is crucial in solid-state battery operation, where especially particles with low contact determine the battery performance and if there is a sufficient loss of contact particles can become completely inactive reducing the overall battery capacity. Modeling of a diffusive interlayer between the solid electrolyte and LFP particles shows that, when the interphase transport is limiting, interphase formation around the parti-

cles increases the active particle population and reaction front width before increasing the internal resistance of the battery.

5.6. PARAMETERS

Table 5.1: Parameters used for the multiphase porous electrode theory simulations.

LFP parameters		
Enthalpy of mixing (Ω)	$1.8560 \cdot 10^{-20}$ J/Li	4
Gradient penalty (κ)	$5.0148 \cdot 10^{-10}$ J/m	4
Coherency strain (B)	$0.1916 \cdot 10^9$ Pa	4
LFP volume loading	0.69	31
LFP charge transfer coefficient (α)	0.5	4
Geometrical parameters		
Particle radius (r)	100 nm*	31
Electrolyte length (L)	50 μm^*	6
Porosity electrode (ϵ_{trode})	0.4	50
Number of particles	100	
Bruggeman coefficient	1.5	6,43
Solid electrolyte		
Maximum concentration (c_{max})	80 M (83.94 M)	51
Li-ion concentration (c_0)	40 M (39.45 M)	51
Enthalpy of mixing (α_s)	0 eV	13,38
Li-ion diffusivity D^+	$5.50 \cdot 10^{-12}$ cm ² /s	52
Anion diffusivity D^-	$5.50 \cdot 10^{-17}$	36
Dilute electrolyte		
Li-ion concentration (c_0)	1 M	31
Li-ion diffusivity D^+	$2.20 \cdot 10^{-10}$ cm ² /s	31
Anion diffusivity D^-	$2.94 \cdot 10^{-10}$ cm ² /s	31

*Varying for different simulations

REFERENCES

- [1] T. Famprikis, P. Canepa, J. A. Dawson, M. S. Islam, and C. Masquelier, *Fundamentals of inorganic solid-state electrolytes for batteries*, *Nature Materials* **18**, 1278–1291 (2019).
- [2] J. Janek and W. G. Zeier, *A solid future for battery development*, *Nature Energy* **1**, 1–4 (2016).
- [3] Z. Zhang, Y. Shao, B. Lotsch, Y.-S. Hu, H. Li, J. Janek, L. F. Nazar, C.-W. Nan, J. Maier, M. Armand, *et al.*, *New horizons for inorganic solid state ion conductors*, *Energy & Environmental Science* **11**, 1945–1976 (2018).
- [4] D. A. Cogswell and M. Z. Bazant, *Coherency strain and the kinetics of phase separation in LiFePO_4 nanoparticles*, *ACS Nano* **6**, 2215 (2012).
- [5] D. A. Cogswell and M. Z. Bazant, *Size-dependent phase morphologies in LiFePO_4 battery particles*, *Electrochemistry Communications* **95**, 33 (2018).
- [6] Y. Li, F. El Gabaly, T. R. Ferguson, R. B. Smith, N. C. Bartelt, J. D. Sugar, K. R. Fenton, D. A. Cogswell, A. L. D. Kilcoyne, T. Tyliszczak, M. Z. Bazant, and W. C. Chueh, *Current-induced transition from particle-by-particle to concurrent intercalation in phase-separating battery electrodes*, *Nature Materials* **13**, 1149 (2014), number: 12.
- [7] M. Z. Bazant, *Theory of chemical kinetics and charge transfer based on nonequilibrium thermodynamics*, *Accounts of Chemical Research* **46**, 1144 (2013).
- [8] H. Liu, F. C. Strobridge, O. J. Borkiewicz, K. M. Wiaderek, K. W. Chapman, P. J. Chupas, and C. P. Grey, *Capturing metastable structures during high-rate cycling of LiFePO_4 nanoparticle electrodes*, *Science* **344**, 1252817 (2014).
- [9] N. J. J. de Klerk, A. Vasileiadis, R. B. Smith, M. Z. Bazant, and M. Wagemaker, *Explaining key properties of lithiation in TiO_2 -anatase li-ion battery electrodes using phase-field modeling*, *Physical Review Materials* **1** (2017).
- [10] A. Vasileiadis, N. J. J. de Klerk, R. B. Smith, S. Ganapathy, P. P. R. M. L. Harks, M. Z. Bazant, and M. Wagemaker, *Toward optimal performance and in-depth understanding of spinel $\text{Li}_4\text{Ti}_5\text{O}_{12}$ electrodes through phase field modeling*, *Advanced Functional Materials* **28**, 1705992 (2018).
- [11] J.-M. Hu, B. Wang, Y. Ji, T. Yang, X. Cheng, Y. Wang, and L.-Q. Chen, *Phase-field based multiscale modeling of heterogeneous solid electrolytes: Applications to nanoporous Li_3PS_3* , *ACS Applied Materials & Interfaces* **9**, 33341 (2017).
- [12] K. Shen, Y. Wang, J. Zhang, Y. Zong, G. Li, C. Zhao, and H. Chen, *Revealing the effect of grain boundary segregation on Li ion transport in polycrystalline anti-perovskite Li_3ClO : a phase field study*, *Physical Chemistry Chemical Physics* **22**, 3030 (2020).
- [13] M. Landstorfer, S. Funken, and T. Jacob, *An advanced model framework for solid electrolyte intercalation batteries*, *Physical Chemistry Chemical Physics* **13**, 12817 (2011).

- [14] M. Doyle, T. F. Fuller, and J. Newman, *Modeling of galvanostatic charge and discharge of the lithium/polymer/insertion cell*, *Journal of The Electrochemical Society* **140**, 1526 (1993).
- [15] J. Newman and N. P. Balsara, *Electrochemical systems*, **4**, 611 (2021).
- [16] L. Raijmakers, D. Danilov, R.-A. Eichel, and P. Notten, *An advanced all-solid-state li-ion battery model*, *Electrochimica Acta* **330**, 135147 (2020).
- [17] H.-K. Tian and Y. Qi, *Simulation of the effect of contact area loss in all-solid-state Li-ion batteries*, *Journal of The Electrochemical Society* **164**, E3512 (2017).
- [18] N. J. J. de Klerk, I. Rosłoń, and M. Wagemaker, *Diffusion mechanism of Li argyrodite solid electrolytes for Li-ion batteries and prediction of optimized halogen doping: The effect of Li vacancies, halogens, and halogen disorder*, *Chemistry of Materials* **28**, 7955 (2016).
- [19] A. Bielefeld, D. A. Weber, R. Rueß, V. Glavas, and J. Janek, *Influence of lithium ion kinetics, particle morphology and voids on the electrochemical performance of composite cathodes for all-solid-state batteries*, *Journal of The Electrochemical Society* **169**, 020539 (2022).
- [20] R. Koerver, I. Aygün, T. Leichtweiß, C. Dietrich, W. Zhang, J. O. Binder, P. Hartmann, W. G. Zeier, and J. Janek, *Capacity fade in solid-state batteries: Interphase formation and chemomechanical processes in nickel-rich layered oxide cathodes and lithium thiophosphate solid electrolytes*, *Chem. Mater.*, **9** (2017).
- [21] G. Bucci, T. Swamy, Y.-M. Chiang, and W. C. Carter, *Modeling of internal mechanical failure of all-solid-state batteries during electrochemical cycling, and implications for battery design*, *Journal of Materials Chemistry A* **5**, 19422 (2017).
- [22] A. Sakuda, A. Hayashi, and M. Tatsumisago, *Sulfide solid electrolyte with favorable mechanical property for all-solid-state lithium battery*, *Scientific Reports* **3**, 2261 (2013).
- [23] A. N. Mistry, K. Smith, and P. P. Mukherjee, *Secondary-phase stochastics in lithium-ion battery electrodes*, *ACS Applied Materials & Interfaces* **10**, 6317 (2018).
- [24] H. Fathiannasab, A. Ghorbani Kashkooli, T. Li, L. Zhu, and Z. Chen, *Three-dimensional modeling of all-solid-state lithium-ion batteries using synchrotron transmission X-ray microscopy tomography*, *Journal of The Electrochemical Society* **167**, 100558 (2020).
- [25] M. Kroll, M. Duchardt, S. L. Karstens, S. Schlabach, F. Lange, J. Hochstrasser, B. Roling, and U. Tallarek, *Sheet-type all-solid-state batteries with sulfidic electrolytes: Analysis of kinetic limitations based on a cathode morphology study*, *Journal of Power Sources* **505**, 230064 (2021-09).

- [26] R. Koerver, W. Zhang, L. de Biasi, S. Schweidler, A. O. Kondrakov, S. Kolling, T. Brezesinski, P. Hartmann, W. G. Zeier, and J. Janek, *Chemo-mechanical expansion of lithium electrode materials – on the route to mechanically optimized all-solid-state batteries*, *Energy & Environmental Science* **11**, 2142 (2018).
- [27] T. K. Schwietert, A. Vasileiadis, and M. Wagemaker, *First-principles prediction of the electrochemical stability and reaction mechanisms of solid-state electrolytes*, *JACS Au*, jacsau.1c00228 (2021).
- [28] J. A. Lewis, F. J. Q. Cortes, Y. Liu, J. C. Miers, A. Verma, B. S. Vishnugopi, J. Tippens, D. Prakash, T. S. Marchese, S. Y. Han, C. Lee, P. P. Shetty, H.-W. Lee, P. Shevchenko, F. De Carlo, C. Saldana, P. P. Mukherjee, and M. T. McDowell, *Linking void and interphase evolution to electrochemistry in solid-state batteries using operando x-ray tomography*, *Nature Materials* **20**, 503 (2021).
- [29] M. Doyle, J. Newman, A. S. Gozdz, C. N. Schmutz, and J. Tarascon, *Comparison of modeling predictions with experimental data from plastic lithium ion cells*, *Journal of The Electrochemical Society* **143**, 1890 (1996).
- [30] M. Safari, M. Morcrette, A. Teyssot, and C. Delacourt, *Multimodal physics-based aging model for life prediction of Li-ion batteries*, *Journal of The Electrochemical Society* **156**, A145 (2009).
- [31] R. B. Smith and M. Z. Bazant, *Multiphase porous electrode theory*, *Journal of The Electrochemical Society* **164**, E3291 (2017).
- [32] S. Yubuchi, W. Nakamura, T. Bibienne, S. Rousselot, L. W. Taylor, M. Pasquali, M. Dollé, A. Sakuda, A. Hayashi, and M. Tatsumisago, *All-solid-state cells with $\text{Li}_4\text{Ti}_5\text{O}_{12}$ /carbon nanotube composite electrodes prepared by infiltration with argyrodite sulfide-based solid electrolytes via liquid-phase processing*, *Journal of Power Sources* **417**, 125 (2019).
- [33] D. M. Bernardi and J.-Y. Go, *Analysis of pulse and relaxation behavior in lithium-ion batteries*, *Journal of Power Sources* **196**, 412 (2011).
- [34] Y. Liu, Y.-B. Ma, W. Jaegermann, R. Hausbrand, and B.-X. Xu, *Interface equilibrium modeling of all-solid-state lithium-ion thin film batteries*, *Journal of Power Sources* **454**, 227892.
- [35] T. R. Ferguson and M. Z. Bazant, *Nonequilibrium thermodynamics of porous electrodes*, *Journal of The Electrochemical Society* **159**, A1967 A1985 (2012).
- [36] Z. Zhang, L. Zhang, Y. Liu, C. Yu, X. Yan, B. Xu, and L.-m. Wang, *Synthesis and characterization of argyrodite solid electrolytes for all-solid-state li-ion batteries*, *Journal of Alloys and Compounds* **747**, 227 (2018).
- [37] K. M. Diederichsen, E. J. McShane, and B. D. McCloskey, *Promising routes to a high Li^+ transference number electrolyte for lithium ion batteries*, *ACS Energy Letters* **2**, 2563 (2017).

- [38] N. J. J. de Klerk and M. Wagemaker, *Space-charge layers in all-solid-state batteries; important or negligible?* *ACS Applied Energy Materials*, [acsaem.8b01141](#) (2018).
- [39] P. Bai, D. A. Cogswell, and M. Z. Bazant, *Suppression of phase separation in LiFePO₄ nanoparticles during battery discharge*, *Nano Letters* **11**, 4890 (2011).
- [40] L. O. Valøen and J. N. Reimers, *Transport properties of LiPF₆-based Li-ion battery electrolytes*, *Journal of The Electrochemical Society*, **11** (2005).
- [41] A. M. Bates, Y. Preger, L. Torres-Castro, K. L. Harrison, S. J. Harris, and J. Hewson, *Are solid-state batteries safer than lithium-ion batteries?* *Joule* (2022).
- [42] M. Z. Bazant, *Thermodynamic stability of driven open systems and control of phase separation by electro-autocatalysis*, *Faraday Discussions* **199**, 423 (2017).
- [43] N. Wolff, F. Röder, and U. Krewer, *Model based assessment of performance of lithium-ion batteries using single ion conducting electrolytes*, *Electrochimica Acta* **284**, 639 (2018).
- [44] M. Torchio, L. Magni, R. B. Gopaluni, R. D. Braatz, and D. M. Raimondo, *LION-SIMBA: A matlab framework based on a finite volume model suitable for li-ion battery design, simulation, and control*, *Journal of The Electrochemical Society* **163**, A1192 (2016).
- [45] A. Neumann, S. Randau, K. Becker-Steinberger, T. Danner, S. Hein, Z. Ning, J. Marrow, F. H. Richter, J. Janek, and A. Latz, *Analysis of interfacial effects in all-solid-state batteries with thiophosphate solid electrolytes*, *ACS Applied Materials & Interfaces*, [acsami.9b21404](#) (2020).
- [46] S. Ansah, N. Shin, J.-S. Lee, and H.-H. Cho, *A comprehensive parametric study for solid-state lithium-ion battery through finite element simulation*, *Electronic Materials Letters* **17**, 532 (2021), number: 6.
- [47] M. Finsterbusch, T. Danner, C.-L. Tsai, S. Uhlenbruck, A. Latz, and O. Guillon, *High capacity garnet-based all-solid-state lithium batteries: Fabrication and 3D-microstructure resolved modeling*, *ACS Applied Materials & Interfaces* **10**, 22329 (2018).
- [48] T. K. Schwietert, V. A. Arszewska, C. Wang, C. Yu, A. Vasileiadis, N. J. J. de Klerk, J. Hageman, T. Hupfer, I. Kerkamm, Y. Xu, E. van der Maas, E. M. Kelder, S. Ganapathy, and M. Wagemaker, *Clarifying the relationship between redox activity and electrochemical stability in solid electrolytes*, *Nature Materials* **19**, 428 (2020).
- [49] L. Han, M. L. Lehmann, J. Zhu, T. Liu, Z. Zhou, X. Tang, C.-T. Heish, A. P. Sokolov, P. Cao, X. C. Chen, and T. Saito, *Recent developments and challenges in hybrid solid electrolytes for lithium-ion batteries*, *Frontiers in Energy Research* **8**, 202 (2020).
- [50] A. G. Kashkooli, S. Farhad, D. U. Lee, K. Feng, S. Litster, S. K. Babu, L. Zhu, and Z. Chen, *Multiscale modeling of lithium-ion battery electrodes based on nano-scale X-ray computed tomography*, *Journal of Power Sources* **307**, 496 (2016).

- [51] C. Yu, L. van Eijck, S. Ganapathy, and M. Wagemaker, *Synthesis, structure and electrochemical performance of the argyrodite $\text{Li}_6\text{PS}_5\text{Cl}$ solid electrolyte for li-ion solid state batteries*, *Electrochimica Acta* **215**, 93 (2016).
- [52] H.-J. Deiseroth, J. Maier, K. Weichert, V. Nickel, S.-T. Kong, and C. Reiner, *Li_7PS_6 and $\text{Li}_6\text{PS}_5\text{X}$ ($X: \text{Cl}, \text{Br}, \text{I}$): Possible three-dimensional diffusion pathways for lithium ions and temperature dependence of the ionic conductivity by impedance measurements*, *Zeitschrift für anorganische und allgemeine Chemie* **637**, 1287 (2011).

A

APPENDIX

A.1. APPENDIX CHAPTER 2

Table A.1: Reduction voltages of elemental phosphorus towards Li_3P calculated from the stable configurations on the P convex hull. All energies are taken from the Materials Project database.

Phase	Voltage (V)
P	-
LiP_7	1.27
Li_3P_7	1.17
LiP	0.94
Li_3P	0.87

Table A.2: Rietveld refinement of pristine $\text{Li}_6\text{PS}_5\text{Cl}$ as at room temperature. Lattice parameter, fractional atomic coordinates, isotropic atomic displacement and site occupancies are refined.

$\text{Li}_6\text{PS}_5\text{Cl}$	Atom	X	Y	Z	Wyckoff	Occ.	Uiso (\AA^2)
F43m	Li	0.1630	0.1630	-0.0082	48h	0.47	0.055
a = 9.853	P	0.5	0.5	0.5	4b	1.00	0.027
	S1	0.6223	0.6223	0.6223	16e	1.00	0.044
	S2	0.0	0.0	0.0	4c	0.53	0.040
	S3	0.25	0.25	0.25	4a	0.32	0.038
	Cl1	0.0	0.0	0.0	4c	0.47	0.028
	Cl2	0.25	0.25	0.25	4a	0.68	0.026

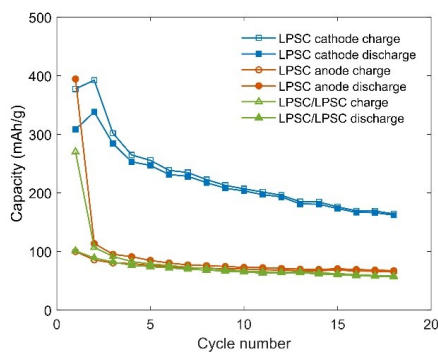


Figure A.1: Cycling performance of In | LPSC | LPSC-C, Li-In | LPSC | LPSC-C and one material battery LPSC-C | LPSC | LPSC-C ASSBs.

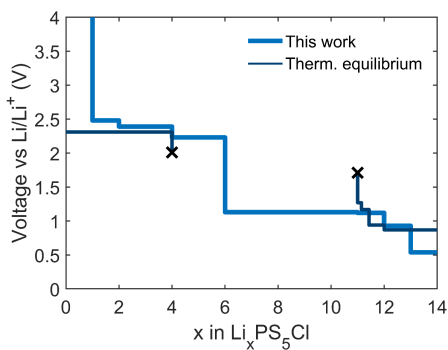


Figure A.2: Calculated theoretical voltage profile, vs. Li/Li^+ , of $\text{Li}_x\text{PS}_5\text{Cl}$ in the compositional range of $0 < x < 14$ and the theoretical voltage profile calculated at thermal equilibrium. The voltage window calculated in this work determines the initial voltage window achieving metastable decomposition (de)lithiated phases of $\text{Li}_x\text{PS}_5\text{Cl}$. The decomposition products i.e. P can follow the thermodynamic equilibrium voltages to lithiate further towards Li^3P .

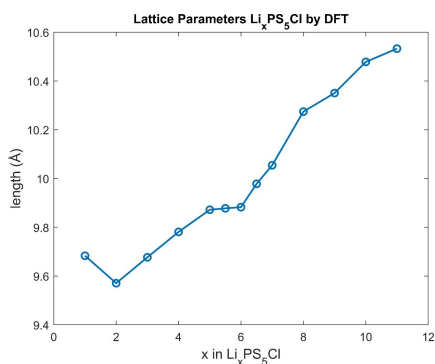


Figure A.3: Lattice parameters of structures $\text{Li}_x\text{PS}_5\text{Cl}$ ($1 < x < 12$) calculated by DFT.

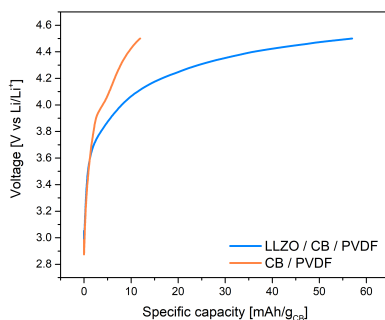


Figure A.4: Voltage profiles during oxidation up to 4.5 V vs Li/Li^+ with current of $7.0 \mu\text{A}$ of the LLZO-C electrode and the blank carbon electrode. Electrochemical activity is observed above 3.6 V vs. Li/Li^+ , indicating the oxidation of LLZO, consistent with previously redox activity observed¹. The specific capacity is calculated based on weight of carbon black, which results in similar carbon black loading for LLZO-C and blank electrode. Blank test shows the capacity contribution of the side reactions and the additional capacity indicates the activity of LLZO.

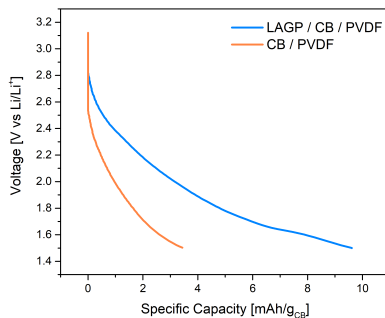


Figure A.5: Voltage profiles during reduction up to 1.5 V vs Li/Li^+ with current of $7.0 \mu\text{A}$ of the LAGP-C electrode and the blank carbon electrode. Electrochemical activity is observed below 2.4 V vs. Li/Li^+ , indicating the reduction of LAGP. The specific capacity is calculated based on weight of carbon black, which results in similar carbon black loading for LAGP-C and blank electrode. The blank test shows the capacity contribution of the side reactions and the additional capacity indicates the activity of LAGP.

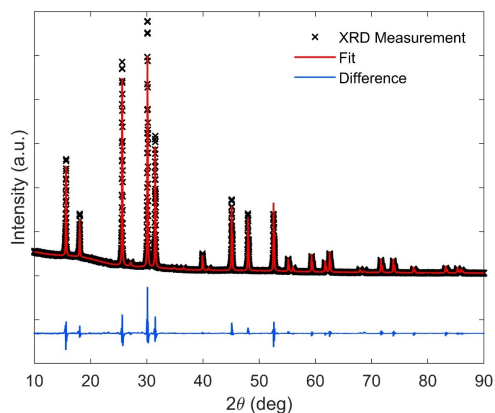


Figure A.6: Rietveld refinement of the X-ray powder diffraction data of pristine $\text{Li}_6\text{PS}_5\text{Cl}$ at room temperature.

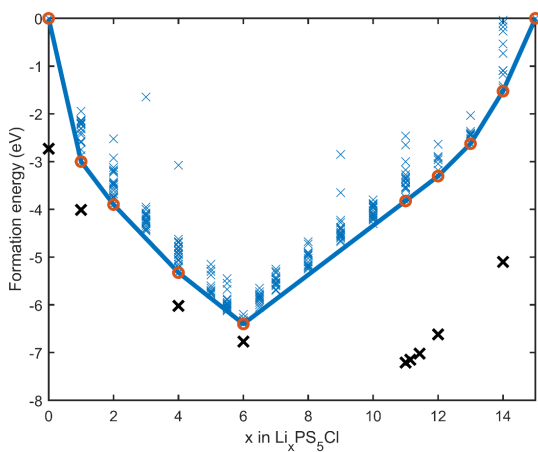


Figure A.7: Formation energies of Li-vacancy configurations of $\text{Li}_x\text{PS}_5\text{Cl}$ (extended to $x = 15$) and comparison of experimental and calculated voltage profiles. Formation energies per formula unit for all symmetrically non-equivalent Li configurations within one unit cell, versus the composition x in $\text{Li}_x\text{PS}_5\text{Cl}$. The formation energy of the combination of thermodynamically favourable decomposition are shown, in line with the decomposition products previously reported. The theoretical voltages are shown in Appendix Figure A.2.

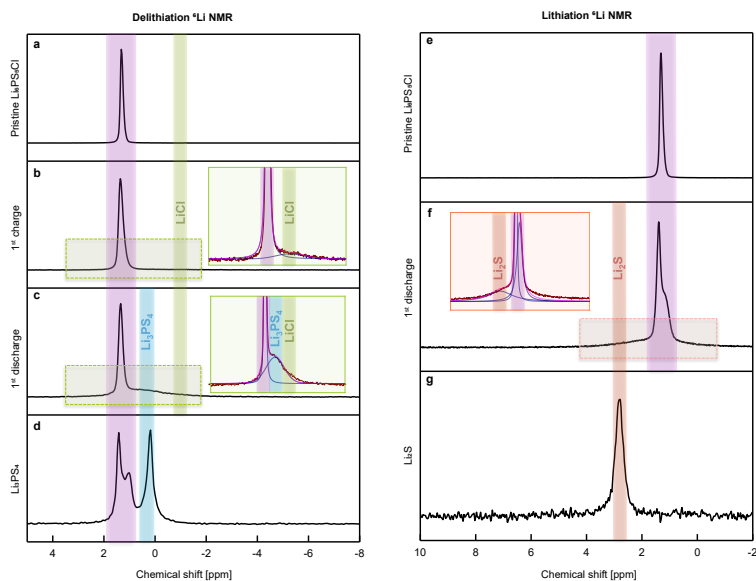


Figure A.8: ${}^6\text{Li}$ MAS NMR spectra of the cathodic mixtures and anodic mixtures. ${}^6\text{Li}$ MAS NMR spectra of the cathodic mixtures (a–d) and anodic mixtures (e–g) of $\text{Li}_6\text{PS}_5\text{Cl}$ in the $\text{In}|\text{LPSC}|\text{LPSC-C}$ and $\text{Li-In}|\text{LPSC}|\text{LPSC-C}$ solid-state batteries respectively. After first charge of the $\text{In}|\text{LPSC}|\text{LPSC-C}$ solid-state cell, formation of LiCl is observed (b). First discharge shows formation at a new resonance frequency corresponding to Li_3PS_4 (c,d). The solid state cell, which starts from lithiation process (f), results in formation of Li_2S , confirmed with the spectrum of the reference Li_2S (g).

A.2. APPENDIX CHAPTER 3

Table A.3: Materials, structures and parameters used in the density functional theory (DFT) simulations.

Material	Acronym	Structure	K-points	Space group	Inserted Li pos.	Supercell
Li ₃ PS ₄	LPS	mp-985583, ¹	5 3 3	Pnma	4c, 4a, 8d	1x1x1
Li ₆ PS ₅ Br	LPSB	²	4 4 4	F $\bar{4}$ 3m	48h	1x1x1
Li ₆ PS ₅ Cl	LPSC	³	-	-	48h	-
Li ₁₀ GeP ₂ S ₁₂	LGPS	⁴	3 3 3	P42mc	1d, 2d, 4d, 8e, 16h	1x1x1
LiBH ₄	LBH	mp-30209, ¹	5 5 5	Pnma	4c	1x2x1
Li ₃ YBr ₆	LYB	⁵	5 5 5	C12/m1	4h, 4g, 2d, 8j	1x1x1
Li ₃ OCl	LOC	mp-985585, ¹	3 3 3	Pm $\bar{3}$ m	3c	2x2x2
Li ₂ PO ₂ N	LIPON	mp-1020019, ¹	1 1 1	Cmc21	4a, 8b	1x2x2
Li ₇ La ₃ Zr ₂ O ₁₂	LLZO	³	-	-	8a, 16f, 32g	-
Li _{0.33} La _{0.56} TiO ₃	LLTO	⁶	3 3 1	P4/mmm	1d, 1c	2x2x2
Li _{1.5} Al _{0.5} Ti _{1.5} (PO ₄) ₃	LATP	⁷	3 3 1	R $\bar{3}$ c	6a, 6b, 18e	1x1x1
Li _{1.5} Al _{0.5} Ge _{1.5} (PO ₄) ₃	LAGP	⁸	-	R $\bar{3}$ c	6b, 36f	-

Table A.4: Metastable phases and corresponding volume, band gap and ionic conductivity calculated by density functional theory (DFT) simulations of Li₃PS₄.

Li ₃ PS ₄	Phase	Volume (Å ³)	Band gap (eV)	Ionic conductivity (S/m, 600K)
	Li ₃ PS ₄	660.68	2.675	203.61
Delithiated	Li ₁ PS ₄	588.60	2.611	67.43
Lithiated	Li ₈ PS ₄	762.92	1.422	302.82

Table A.5: Metastable phases and corresponding volume, band gap and ionic conductivity calculated by density functional theory (DFT) simulations of Li₆PS₅Br.

Li ₆ PS ₅ Br	Phase	Volume (Å ³)	Band gap (eV)	Ionic conductivity (S/m, 600K)
	Li ₆ PS ₅ Br	1001.00	2.093	65.80
Delithiated	Li ₄ PS ₅ Br	988.54	2.173	18.36
Lithiated	Li ₁₀ PS ₅ Br	1174.62	1.391	33.57

Table A.6: Metastable phases and corresponding volume, band gap and ionic conductivity calculated by density functional theory (DFT) simulations of $\text{Li}_6\text{PS}_5\text{Cl}$.

$\text{Li}_6\text{PS}_5\text{Cl}$	Phase	Volume (\AA^3)	Band gap (eV)	Ionic conductivity (S/m, 600K)
	$\text{Li}_6\text{PS}_5\text{Cl}$	965.21	1.984	95.78
Delithiated	$\text{Li}_4\text{PS}_5\text{Cl}$	935.80	2.391	43.83
Lithiated	$\text{Li}_{11}\text{PS}_5\text{Cl}$	1168.50	1.219	59.53

Table A.7: Metastable phases and corresponding volume, band gap and ionic conductivity calculated by density functional theory (DFT) simulations of $\text{Li}_{10}\text{GeP}_2\text{S}_{12}$.

$\text{Li}_{10}\text{GeP}_2\text{S}_{12}$	Phase	Volume (\AA^3)	Band gap (eV)	Ionic conductivity (S/m, 600K)
	$\text{Li}_{10}\text{GeP}_2\text{S}_{12}$	982.70	2.242	68.85
Delithiated	$\text{Li}_4\text{GeP}_2\text{S}_{12}$	975.99	2.124	14.27
Lithiated	$\text{Li}_{18}\text{GeP}_2\text{S}_{12}$	1150.85	1.702	39.33

Table A.8: Metastable phases and corresponding volume, band gap and ionic conductivity calculated by density functional theory (DFT) simulations of LiBH_4 .

LiBH_4	Phase	Volume (\AA^3)	Band gap (eV)	Ionic conductivity (S/m, 1000K)
	LiBH_4	400.29	6.930	233.39
Delithiated	$\text{Li}_{0.88}\text{BH}_4$	316.35	6.763	243.08
Lithiated	Li_3BH_4	602.58	0	260.49

Table A.9: Metastable phases and corresponding volume, band gap and ionic conductivity calculated by density functional theory (DFT) simulations of Li_3YBr_6 .

Li_3YBr_6	Phase	Volume (\AA^3)	Band gap (eV)	Ionic conductivity (S/m, 1000K)
	Li_3YBr_6	553.48	3.723	142.26
Delithiated	LiYBr_6	578.99	1.745	22.71
Lithiated	Li_7YBr_6	711.29	0	248.49

Table A.10: Metastable phases and corresponding volume, band gap and ionic conductivity calculated by density functional theory (DFT) simulations of Li_3OCl .

Li_3OCl	Phase	Volume (\AA^3)	Band gap (eV)	Ionic conductivity (S/m, 1000K)
	Li_3OCl	469.20	4.764	55.25
Delithiated	LiOCl	406.88	0	58.55

Table A.11: Metastable phases and corresponding volume, band gap and ionic conductivity calculated by density functional theory (DFT) simulations of Li_3PS_4 .

$\text{Li}_2\text{PO}_2\text{N}$	Phase	Volume (\AA^3)	Band gap (eV)	Ionic conductivity (S/m, 1000K)
	$\text{Li}_2\text{PO}_2\text{N}$	942.68	5.536	5.75
Delithiated	LiPO_2N	1025.14	3.037	18.21
Lithiated	$\text{Li}_4\text{PO}_2\text{N}$	1330.15	0.8731	128.84

Table A.12: Metastable phases and corresponding volume, band gap and ionic conductivity calculated by density functional theory (DFT) simulations of $\text{Li}_7\text{La}_3\text{Zr}_2\text{O}_{12}$.

$\text{Li}_7\text{La}_3\text{Zr}_2\text{O}_{12}$	Phase	Volume (\AA^3)	Band gap (eV)	Ionic conductivity (S/m, 1000K)
	$\text{Li}_7\text{La}_3\text{Zr}_2\text{O}_{12}$	2217.17	4.113	52.85
Delithiated	$\text{LiLa}_3\text{Zr}_2\text{O}_{12}$	2211.57	3.920	0.81

Table A.13: Metastable phases and corresponding volume, band gap and ionic conductivity calculated by density functional theory (DFT) simulations of $\text{Li}_{0.33}\text{La}_{0.56}\text{TiO}_3$.

$\text{Li}_{0.33}\text{La}_{0.56}\text{TiO}_3$	Phase	Volume (\AA^3)	Band gap (eV)	Ionic conductivity (S/m, 1000K)
	$\text{Li}_{0.33}\text{La}_{0.56}\text{TiO}_3$	948.47	1.793	4.04
Delithiated	$\text{Li}_{0.18}\text{La}_{0.56}\text{TiO}_3$	953.69	1.921	0.20
Lithiated	$\text{Li}_{0.37}\text{La}_{0.56}\text{TiO}_3$	933.45	0	0.86

Table A.14: Metastable phases and corresponding volume, band gap and ionic conductivity calculated by density functional theory (DFT) simulations of $\text{Li}_{1.5}\text{Al}_{0.5}\text{Ti}_{1.5}(\text{PO}_4)_3$.

$\text{Li}_{1.5}\text{Al}_{0.5}\text{Ti}_{1.5}(\text{PO}_4)_3$	Phase	Volume (\AA^3)	Band gap (eV)	Ionic conductivity (S/m, 1000K)
	$\text{Li}_{1.5}\text{Al}_{0.5}\text{Ti}_{1.5}(\text{PO}_4)_3$	1404.34	2.4735	104.46
Delithiated	$\text{Al}_{0.5}\text{Ti}_{1.5}(\text{PO}_4)_3$	1403.86	2.1290	*
Lithiated	$\text{Li}_3\text{Al}_{0.5}\text{Ti}_{1.5}(\text{PO}_4)_3$	1351.52	2.0490	30.06

Table A.15: Metastable phases and corresponding volume, band gap and ionic conductivity calculated by density functional theory (DFT) simulations of $\text{Li}_{1.5}\text{Al}_{0.5}\text{Ge}_{1.5}(\text{PO}_4)_3$.

$\text{Li}_{1.5}\text{Al}_{0.5}\text{Ge}_{1.5}(\text{PO}_4)_3$	Phase	Volume (\AA^3)	Band gap (eV)	Ionic conductivity (S/m, 1000K)
	$\text{Li}_{1.5}\text{Al}_{0.5}\text{Ge}_{1.5}(\text{PO}_4)_3$	1278.20	2.547	70.96
Delithiated	$\text{Li}_{1.33}\text{Al}_{0.5}\text{Ge}_{1.5}(\text{PO}_4)_3$	1272.84	3.318	53.98
Lithiated	$\text{Li}_{3.5}\text{Al}_{0.5}\text{Ge}_{1.5}(\text{PO}_4)_3$	1392.24	2.625	8.49

In Table A.3-A.15, the volume is determined from the relaxed structure after the DFT relaxation. The band gap is determined from the density of states calculated by a DFT calculation with an increased k-point mesh. For the ionic conductivity the mean squared displacement of Li is calculated using an ab-initio molecular dynamics simulation at the specified temperature.⁹ From the mean squared displacement the ionic conductivity at the corresponding temperature is calculated. * No Li in structure.

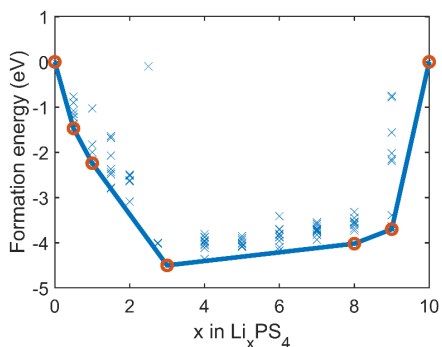


Figure A.9: Formation energies per formula unit for x in Li_3PS_4 . The most stable configurations are shown with an orange circle and form the convex hull.

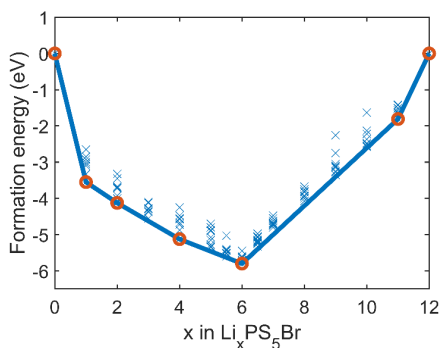


Figure A.10: Formation energies per formula unit for x in $\text{Li}_6\text{PS}_5\text{Br}$.

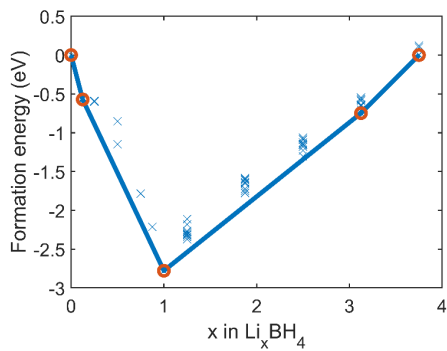


Figure A.11: Formation energies per formula unit for x in LiBH_4 .

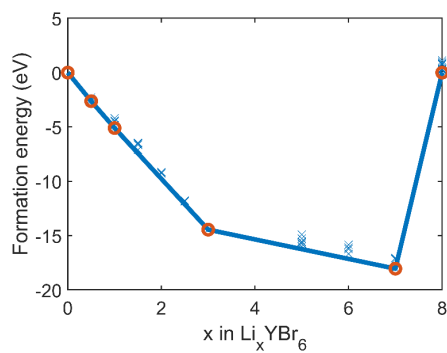


Figure A.12: Formation energies per formula unit for x in Li_3YBr_6 .

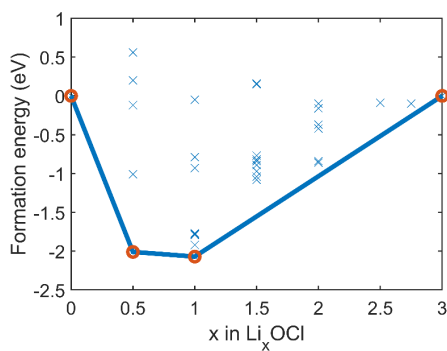


Figure A.13: Formation energies per formula unit for x in Li_3OCl .

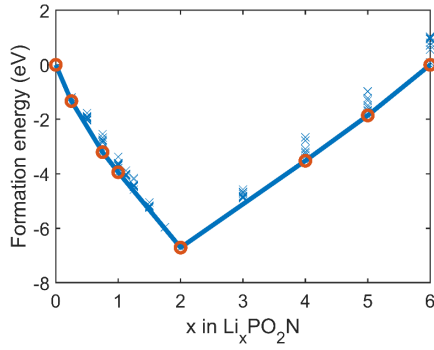


Figure A.14: Formation energies per formula unit for x in $\text{Li}_x\text{PO}_2\text{N}$.

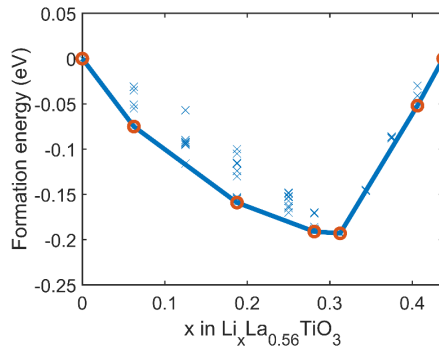


Figure A.15: Formation energies per formula unit for x in $\text{Li}_{0.33}\text{La}_{0.56}\text{TiO}_3$.

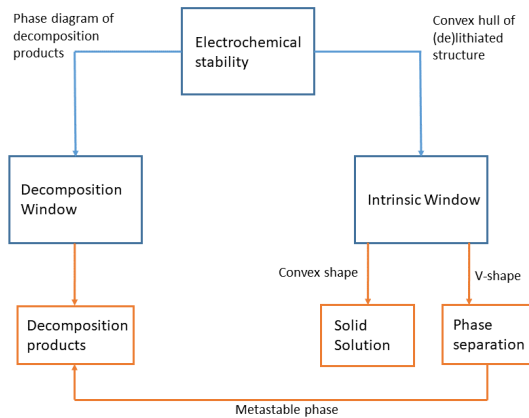


Figure A.16: Flow diagram for calculating the voltages to corresponding decomposition route of a solid material.

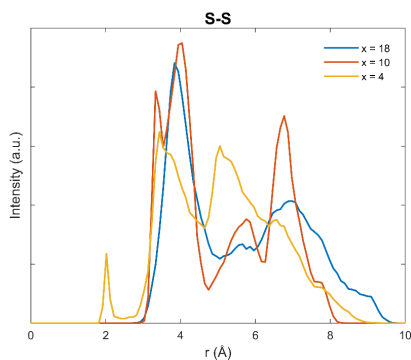


Figure A.17: Radial distribution function (RDF) of S-S bonds in $\text{Li}_4\text{GeP}_2\text{S}_{12}$, $\text{Li}_{10}\text{GeP}_2\text{S}_{12}$ and $\text{Li}_{18}\text{GeP}_2\text{S}_{12}$ calculated from ab-initio molecular dynamics simulations. During delithiation an increase in intensity around 2 Å is shown, representing formation of S-S bonds formed during oxidation of S in the $\text{Li}_{10}\text{GeP}_2\text{S}_{12}$ structure.

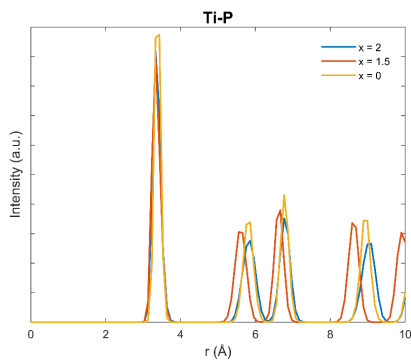


Figure A.18: Radial distribution function (RDF) of Ti-P bonds in $\text{Al}_{0.5}\text{Ti}_{1.5}(\text{PO}_4)_3$, $\text{Li}_{1.5}\text{Al}_{0.5}\text{Ti}_{1.5}(\text{PO}_4)_3$ and $\text{Li}_3\text{Al}_{0.5}\text{Ti}_{1.5}(\text{PO}_4)_3$ calculated from ab-initio molecular dynamics simulations. Minor structural changes are shown representing the relative stable structure of LATP during lithiation and delithiation.

A.3. APPENDIX CHAPTER 4

EXPERIMENTAL DETAILS NEUTRON DIFFRACTION AND RIETVELD REFINEMENT

High-resolution neutron powder diffraction data of Si substitution in $\text{Li}_6\text{P}_1\text{S}_5\text{Br}$ materials were collected at the Heinz Maier-Leibnitz Zentrum (research reactor FRM II, Garching b. München, Germany) using the high-resolution diffractometer SPODI^{10,11} and monochromatic neutrons (wavelength = 1.54817(2) Å). The strategy of data collection and experimental parameters were shown in $\text{Li}_{6+x}\text{P}_{1-x}\text{Si}_x\text{S}_5\text{Br}$.^{10,11} We re-examine the analysis to identify the possible interstitial sites of lithium occupancies, using neutron diffraction data of Si substitution from Minafra et al.¹⁰ and pristine $\text{Li}_6\text{P}_x\text{S}_5\text{Br}$ neutron diffraction data from Gautam et al.¹¹ The measurement of both samples were performed at room temperature.

The TOPAS software tool was used to perform Rietveld refinements of neutron diffraction data. The quality of the fits was determined using the goodness-of-fit (GOF) fit indicator and Rwp. The following parameters were refined: (1) 10 coefficients for a Chebyshev function were used to fit the background and peak shape modeled by the modified Thomson-Cox-Hastings pseudo-Voigt function; (2) scale factor, lattice parameter, and zero error; (3) isotropic atomic displacement parameter; and (4) atomic occupancies of the free S^{2-} (Wyckoff 4d) and Br^- (Wyckoff 4a) anions (refined since these two anions can be exchanged), resulting in site-disorder ($\text{Br}^-/\text{S}^{2-}$). The constraint on the Wyckoff 4a site (occupancies of $\text{Br}^-(4a) + \text{S}^{2-}(4a) = 1$) and the Wyckoff 4d site is equal to 1 (occupancies of $\text{S}^{2-}(4d) + \text{Br}^-(4d) = 1$) due to charge balance in the structure. Additionally Si occupancies also refined. The stability of the refinements was ensured by allowing the refinement of multiple correlated parameters simultaneously. Finally, lithium occupancies on the possible interstitial sites were investigated. Upon refining over several cycles. Finally, the reported structural models were obtained, allowing for the refinement of all these structural parameters simultaneously.

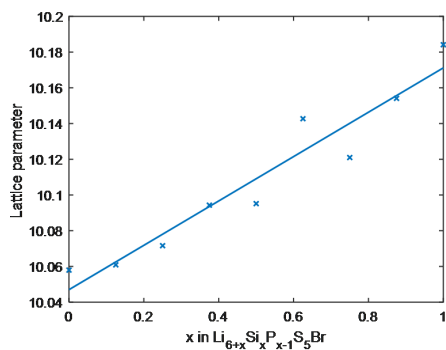


Figure A.19: Lattice parameters determined after a DFT relaxation for different values of x in the $\text{Li}_{6+x}\text{P}_{1-x}\text{Si}_x\text{S}_5\text{Br}$ structure.

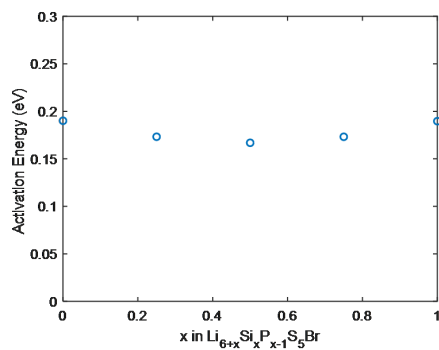


Figure A.20: Activation energies of conductivities calculated for $\text{Li}_{6+x}\text{P}_{1-x}\text{Si}_x\text{S}_5\text{Br}$.

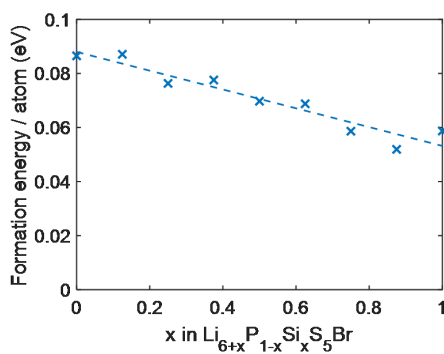


Figure A.21: Formation energy for $\text{Li}_{6+x}\text{P}_{1-x}\text{Si}_x\text{S}_5\text{Br}$ calculated by DFT.

Table A.16: Rietveld refinement of pristine $\text{Li}_{5.875}\text{P}_{0.875}\text{Si}_{0.125}\text{S}_5\text{Br}$ at room temperature. Lattice parameter, fractional atomic coordinates, isotropic atomic displacement and site occupancies are refined.

$\text{Li}_{5.875}\text{P}_{0.875}\text{Si}_{0.125}\text{S}_5\text{Br}$	Atom	Wyckoff	X	Y	Z	Occ.	B_{iso}
$F\bar{4}3m$ $a = 9.853 \text{ \AA}$	Li	48h T5	0.3044	0.0231	0.6956	0.454	3.82
	Li	48h T2	0.277	0.413	0.913	0.025	3.82
	Li	16e	0.154	0.154	0.154	0.077	0.72
	P	4b	0	0	0.5	0.500	3.26
	Si	4b	0	0	0.5	0.060	3.26
	S	16e	0.1164	-0.1164	0.6164	1.000	3.72
	S	4c	0.0	0.0	0.0	0.186	1.39
	S	4a	0.25	0.25	0.75	0.814	2.78
	Br	4c	0.0	0.0	0.0	0.814	1.39
	Br	4a	0.25	0.25	0.75	0.186	2.78

REFERENCES

- [1] A. Jain, S. P. Ong, G. Hautier, W. Chen, W. D. Richards, S. Dacek, S. Cholia, D. Gunter, D. Skinner, G. Ceder, and K. A. Persson, *Commentary: The materials project: A materials genome approach to accelerating materials innovation*, *APL Materials* **1**, 011002 (2013).
- [2] N. J. J. de Klerk, I. Rosłoń, and M. Wagemaker, *Diffusion mechanism of Li argyrodite solid electrolytes for Li-ion batteries and prediction of optimized halogen doping: The effect of Li vacancies, halogens, and halogen disorder*, *Chemistry of Materials* **28**, 7955 (2016).
- [3] T. K. Schwietert, V. A. Arszewska, C. Wang, C. Yu, A. Vasileiadis, N. J. J. de Klerk, J. Hageman, T. Hupfer, I. Kerkamm, Y. Xu, E. van der Maas, E. M. Kelder, S. Ganapathy, and M. Wagemaker, *Clarifying the relationship between redox activity and electrochemical stability in solid electrolytes*, *Nature Materials* **19**, 428 (2020).
- [4] A. Kuhn, J. Köhler, and B. V. Lotsch, *Single-crystal X-ray structure analysis of the superionic conductor $\text{Li}_{10}\text{GeP}_2\text{S}_{12}$* , *Physical Chemistry Chemical Physics* **15**, 11620 (2013).
- [5] A. Bohnsack, G. Balzer, H.-U. Güdel, M. S. Wickleder, and G. Meyer, *Ternäre halogenide vom typ A_3MX_6 . die bromide Li_3MBr_6 ($\text{M}=\text{Sm}, \text{Lu}, \text{Y}$): Synthese, kristallstruktur, ionenbeweglichkeit*, *Zeitschrift für anorganische und allgemeine Chemie* **623**, 1352 (1997).
- [6] T. Teranishi, Y. Ishii, H. Hayashi, and A. Kishimoto, *Lithium ion conductivity of oriented $\text{Li}_{0.33}\text{La}_{0.56}\text{TiO}_3$ solid electrolyte films prepared by a sol-gel process*, *Solid State Ionics* **284**, 1 (2016).
- [7] D. Rettenwander, A. Welzl, S. Pristat, F. Tietz, S. Taibl, G. J. Redhammer, and J. Fleig, *A microcontact impedance study on NASICON-type $\text{Li}_{1+x}\text{Al}_x\text{Ti}_{2-x}(\text{PO}_4)_3$ ($0 \leq x \leq 0.5$) single crystals*, *Journal of Materials Chemistry A* **4**, 1506 (2016).
- [8] J. Kang, H. Chung, C. Doh, B. Kang, and B. Han, *Integrated study of first principles calculations and experimental measurements for Li-ionic conductivity in Al-doped solid-state $\text{LiGe}_2(\text{PO}_4)_3$ electrolyte*, *Journal of Power Sources* **293**, 11 (2015).
- [9] N. J. de Klerk, E. van der Maas, and M. Wagemaker, *Analysis of diffusion in solid-state electrolytes through MD simulations, improvement of the li-ion conductivity in $\beta\text{-Li}_3\text{PS}_4$ as an example*, *ACS Applied Energy Materials* **1**, 3230.
- [10] N. Minafra, S. P. Culver, T. Krauskopf, A. Senyshyn, and W. G. Zeier, *Effect of Si substitution on the structural and transport properties of superionic Li-argyrodites*, *Journal of Materials Chemistry A* **6**, 645 651 (2018).
- [11] A. Gautam, M. Sadowski, M. Ghidui, N. Minafra, A. Senyshyn, K. Albe, and W. G. Zeier, *Engineering the site-disorder and lithium distribution in the lithium superionic argyrodite $\text{Li}_6\text{PS}_5\text{Br}$* , *Advanced Energy Materials* **11**, 2003369 (2021).

SUMMARY

Solid-state batteries have the promise to outperform conventional Li-ion batteries. Solid electrolytes are safer, as the solids used are generally not combustible, and especially if Li-metal anodes are enabled, higher energy densities can be obtained. However, solid-state batteries still have challenges to overcome. In this thesis the origins of the main challenges in solid-state batteries are investigated and this understanding is captured in nano- and microscopic models that can be generally applied to solid-state batteries.

The relatively narrow electrochemical stability window of solid electrolytes is one of the main challenges for solid-state batteries. In Chapter 2 the redox activity and electrochemical stability of an argyrodite, NASICON and a garnet solid electrolyte are investigated. It is demonstrated that the decomposition pathway of the solid electrolytes is rather indirect via (de)lithiated metastable phases, instead of direct via the energetically most stable decomposition products. Because the reaction proceeds via the intermediate phases, these phases determine the electrochemical stability window, generally resulting in a larger stability window. The larger window and reaction pathway that are predicted match with electrochemical experiments and observed (de)lithiated phases in XRD and NMR experiments.

In Chapter 3 the methodology to predict the electrochemical stability window and decomposition reaction pathway by the (de)lithiation potential is applied to a broader range of solid electrolytes from different chemical classes. It is shown that the intrinsic indirect electrochemical window often accurately predicts the practical stability window obtained from the literature. However, if the kinetic barrier for decomposition is relatively small, the electrochemical stability window can be more close to the decomposition window. Additionally, different decomposition mechanisms are found for solid electrolytes such as phase separation and solid solution reactions.

In Chapter 4 the origin of the Li-ion conductivity increase in Si-doped $\text{Li}_6\text{PS}_5\text{Br}$ is investigated. The increase in ionic conductivity is caused by the excess Li in the structure that is enabled by the lower valence of Si^{4+} compared to P^{5+} . This excess of Li resides on a previously unoccupied 16e position between two Li cages. Due to this presence, Li redistributes more homogeneously along neighboring sites, effectively causing a more facile diffusion path. Because this specific jump pathway is the bottleneck for macroscopic diffusion the overall ionic conductivity increases.

In Chapter 5 a model framework for simulating solid-state batteries is presented based on multiphase porous electrode theory. Using the regular solution model a lithium transport equation for solid-state electrolytes is provided. The theoretical results of batteries using solid electrolytes are compared to liquid electrolyte batteries. Because there are limited concentration gradients in the solid electrolytes, the lithiation of the electrodes proceeds more homogeneous for thick electrodes. Contact loss is modeled, where a distribution of contacts is applied to the electrode particles. The results show that especially particles with limited contact determine the overpotential and capacity loss. Addi-

tionally, a novel approach to simulate diffusive interlayers is implemented where specific physics such as SEI formation, coatings or space-charge regions can be modeled.

In short, the relationship between redox activity and the electrochemical stability window of solid electrolytes is established, providing critical insights into the decomposition mechanisms. The origin of aliovalent Si doping on the Li-ion diffusion mechanism in $\text{Li}_6\text{PS}_5\text{Br}$ is elucidated, providing better understanding in the diffusion mechanism and the effect of dopants. Finally, A model framework for solid-state batteries and their main bottlenecks is presented providing key insights in the operation of solid-state batteries.

SAMENVATTING

Vastestofbatterijen hebben de potentie om conventionele Li-ion batterijen te overtreffen. Vastestofelectrolieten zijn veiliger, omdat deze electrolieten niet ontvlambaar zijn, en als er een Li metaal anode gebruikt wordt kan er een hogere energiedichtheid gehaald worden. Er zijn nog wel uitdagingen voor vastestofelectrolieten. In dit proefschrift zoeken we naar de oorzaken van de meest voorkomende uitdagingen in vastestofbatterijen en proberen we deze te modelleren in nano- en microscopische modellen die algemeen toepasbaar zijn.

Een van de grootste uitdagingen voor vastestofelectrolieten is de relatief zwakke electrochemische stabiliteit. In Hoofdstuk 2 wordt de redox activiteit en de electrochemische stabiliteit voor een Argyrodiet, NASICON en Granaat electroliet onderzocht. Er wordt aangetoond dat het vastestofelectroliet niet direct reageert naar de decompositieproducten, maar indirect reageert, via een metastabiele ge(de)lithieerde fase. Omdat de decompositie via deze indirecte route verloopt wordt er een grotere electrochemische stabiliteit verwacht. De voorspelde redox potentialen komen overeen met experimentele electrochemische metingen en de ge(de)lithieerde producten zijn geobserveerd met röntgendiffractie en kernspinresonantie.

In Hoofdstuk 3 wordt de methodologie om de electrochemische stabiliteit te voorspellen gebruikt om meer vastestofelectrolieten in verschillende chemische groepen te bestuderen. Er wordt aangetoond dat de intrinsieke electrochemische stabiliteit vaak dicht bij praktische stabiliteit uit de literatuur zit. Maar als de kinetische barrière naar de decompositie producten relatief klein is, kan de electrochemische stabiliteit dichter bij de formeringsenergie van de decompositie producten zitten. De vastestofelectrolieten hebben verschillende reactie mechanismes, waarbij ze kunnen reageren door middel van fasescheiding of als vaste oplossing.

In Hoofdstuk 4 wordt de toename in Li-ion geleiding van Si-gedoopt $\text{Li}_6\text{PS}_5\text{Br}$ onderzocht. De hogere geleiding wordt veroorzaakt door overtollig Li in de structuur dat wordt geïntroduceerd door Si^{4+} wat een lagere valentie heeft dan P^{5+} . Dit geïntroduceerde Li zit in de kristalstructuur op een voorheen niet bezette 16e positie. Omdat deze 16e positie tussen twee Li posities zit die het knelpunt voor de macroscopische diffusie vormen, gaat de totale geleiding omhoog.

In Hoofdstuk 5 wordt een model van een vastestofbatterij gepresenteerd gebaseerd op 'Multiphase Porous Electrode Theory'. Lithium transport door het vastestofelectroliet wordt beschreven door een 'regular solution' model. De theoretische resultaten van een batterij met een vastestofelectroliet en een vloeibaar elektroliet worden met elkaar vergeleken. Omdat er minder concentratiegradiënten in vastestofelectrolieten zijn vergeleken met vloeibare elektrolieten is de lithiatie meer homogeen in dikkere elektrodes. Ook wordt contactverlies gemodelleerd met een distributie voor de deeltjes in de elektroden waarbij wordt aangetoond dat vooral deeltjes met weinig contact prestatiebepalend

zijn. Ook is een model gemaakt voor een laag tussen de actieve deeltjes en het elektrolyet waar 'SEI' formatie en coatings gesimuleerd kunnen worden.

Samenvattend, de relatie tussen de redoxpotential en electrochemische stabiliteit voor vastestofelectrolieten is bepaald deij kritieke inzichten in het decompositie mechanisme zijn aangetoond. De oorsprong van de toegenomen ionische geleiding van Si substitutie in $\text{Li}_6\text{PS}_5\text{Br}$ is opgehelderd. Ten slotte is een model voor vastestofelectrolieten gemaakt waarbij belangrijke inzichten in de werking van vastestofbatterijen worden getoond.

ACKNOWLEDGEMENTS

I would like to thank all the people who contributed to this PhD thesis.

First of all I would like to thank Marnix, who gave me the opportunity to start this academic journey after my master thesis. I appreciate that you were always very supportive and very welcoming to new ideas. You made have made a warm and open work environment and I am grateful for all the support you give. I also have very good memories of the time we were in the conference in Shenzhen and the several group outings.

Secondly I would like to thank all the thesis committee members for their careful evaluation of this thesis. Especially, my copromotor Erik for his nice constructive discussions about the thesis and several group meetings. I would also like to thank Martin Bazant for giving the opportunity to visit his group in MIT, I had a wonderful time in your group.

I would like to thank the technical support of the group, Michel and Frans for helping in the lab, Kees and Robbert for helping with XRD spectra, and the rest of the technical staff Baukje and Esther. Furthermore I would like to thank Ilse and Nicole for the small chats at the coffee machine and helping out when necessary. Also thanks too Leon, Victor, Nico, Laura for their fast programming skills and the nice discussions. My appreciation to Jouke for the friendly discussions and computational support.

Thanks to all the current and former group members Niek, Michi, Peter-Paul, Chao, Zhu, Xuehang, Lars, Theo, Chaofang, Martijn, Mark, Mark, Pranav, Anika, Zhaolong, Shiv, Shengnan, Qidi, Chenglong, Pedro, Biffo, Zhu, Ajay. Special thanks to Tomas, for bringing enthusiasm to the group and having some beers time to time after work. Also thanks to Swapna for binding the group and organising memorable group outings. Angie for nice coffee talks about coffee, Ming for showing us around in China, having good dinners. Pier for nice computational and fun discussions at work, and Victor for enjoyable discussions and coffee breaks, Eveline for always an interesting talk, Remco for dinners at his home and memorable battery BBQ's. Hanan for being the best office neighbor and the good cappuccinos and lunches, and Alexandros I always enjoyed a lot working together you were always very helpful and enthusiastic, and off course, for having the best Greek food and the wonderful time in Boston.

I would like to thank Viola for being my biggest supporter. We were very lucky to work together a long time, we had a great time and even did some great research together. Also thanks to your family for their support! Furthermore, I like to give my appreciation to all my friends, roommates and club Lans for their support and keeping up a good work life balance, the time in Delft was incredible.

Finally, I would like to thank my parents, brothers, Annika, Muriel, and especially my grandparents Henny and Harry, who always gave me full love and support.

CONFERENCES

- [EUROMAT 2021](#) – *Electrochemical stability and decomposition route of solid electrolytes*. – September 2021 – Oral Presentation
- [International Conference on Energy Storage Materials \(ICEnSM2109\)](#) – *The relationship of the redox activity with the electrochemical stability of solid electrolytes for solid-state batteries* – Shenzhen, China – November 2019 – Oral Presentation
- [Modval 16th](#) Symposium on Modeling and Experimental Validation of Electrochemical Energy Technologies – Braunschweig, Germany Modval – March 2019

LIST OF PUBLICATIONS

5. **Schwietert, T. K.**, *An advanced model for solid-state batteries and its main challenges*, [To be submitted](#).
4. **Schwietert, T. K.**, *The effect of aliovalent cation substitution on the Li-ion diffusion mechanism in Li-argyrodites.*, [Submitted](#).
3. **Schwietert, T. K.** Vasileiadis, A. and Wagemaker, M., *First-Principles Prediction of the Electrochemical Stability and Reaction Mechanisms of Solid-State Electrolytes*, [JACS Au 1, 9 \(2021\)](#)
2. **Schwietert, T. K.**[†], Arszelewska[†], V.A., Wang, C., Yu, C., Vasileiadis, A., de Klerk, N.J., Hageman, J., Hupfer, T., Kerkamm, I., Xu, Y. and van der Maas, E., Kelder, E.M., Ganapathy, S., Wagemaker, M., *Clarifying the relationship between redox activity and electrochemical stability in solid electrolytes*, [Nature Materials 19, 4 \(2020\)](#). († Co first author)
1. Yu, C., Ganapathy, S., Hageman, J., Van Eijck, L., Van Eck, E.R., Zhang, L., **Schwietert, T. K.**, Basak, S., Kelder, E.M. and Wagemaker, M., *Facile Synthesis toward the Optimal Structure-Conductivity Characteristics of the Argyrodite Li₆PS₅Cl Solid-State Electrolyte*, [ACS Appl. Mater. Interfaces 10, 39 \(2018\)](#).

CURRICULUM VITÆ

Tammo Klaas SCHWIETERT

Tammo Klaas Schwietert was born in Amsterdam on 20 September 1992. After finishing high school at the Maartenscollege in Groningen, the Netherlands, he started a Bachelor Applied Physics at the Delft University of Technology in 2011, which he completed in 2015 with a thesis entitled: 'Design of a superconducting on-chip Mach-Zehnder spectrometer for millimeter-submillimeter wave astronomy'. After obtaining his bachelor's degree he continued with a Master Applied physics at the Delft University of Technology specializing in Radiation Science and Technology. At the beginning of his master's study he had the urge to use his theoretical knowledge to solve more practical problems, and he joined Delft Hyperloop, a team competing in a student competition organized by SpaceX to develop a prototype vehicle for a new mode of transportation, the team won the overall prize in the competition in Los Angeles, USA. At the end of the master's degree he worked as an intern at Mapper Lithography where he developed a verification setup for the cooling element used in the beam switcher module of the Mapper lithography machine. For his thesis he joined the group of prof. dr. ir. M. Wagemaker to work on modeling and experiments on solid electrolyte $\text{Li}_6\text{PS}_5\text{Cl}$, his master thesis was entitled: 'Ab initio molecular dynamics simulations and experimental study on $\text{Li}_6\text{PS}_5\text{Cl}$ interfaces for future solid-state batteries'.

His growing interest in energy storage and appreciating the valuable work done in the Storage of Electrochemical Energy group (SEE) at TU Delft led him to pursue a PhD under the supervision of prof. dr. ir. M. Wagemaker. During his research he especially developed skills in battery modeling at various length scales such as Density Functional Theory, Phase Field modeling and Molecular Dynamics. He also performed experimental work such as assembling and electrochemical testing of (solid-state) batteries and used advanced experimental techniques such as XRD and XPS at the TU Delft and EXAFS at the European Synchrotron and Radiation Facility (ESRF) in Grenoble, France. At the end of his PhD he visited the group of E.G. Roos Professor of Chemical Engineering and Mathematics M.Z Bazant at the Massachusetts Institute of Technology (MIT) in Cambridge, USA, where he further developed his knowledge in computational modeling and the fundamental understanding of batteries. Furthermore, during his PhD he supervised several bachelor, minor and master students, and worked as a teaching assistant for the Energy Storage in Batteries course.